Universitat Politècnica de Catalunya
Departament de Física i Enginyeria Nuclear
Departament de Física Aplicada

Programa de Doctorat
Doctorat en Ciència i Tecnologia Aeroespacial

Collective dynamics of Bulk Metallic Glasses Studied by Molecular Dynamics Simulations

Memòria presentada per

Araceli Vallés Sales
per obtenir el títol de Doctora per la Universitat Politècnica de Catalunya.
Directors:

Daniel Crespo Artiaga
Eloi Pineda Soler

19th July 2014

Acknowledgements

I would like to express my special appreciation and thanks to my advisers Professor Daniel Crespo and Professor Eloi Pineda. I would like to thank you for promote my research and for your generous support and coaching, without them all this journey would never had been possible. Their kind assistance, patient and encouragement had been essential for the result of this PhD. Your advice on both, research as well as on my career, were priceless.

I wish to express my sincerest gratitude to Dr. Peter Derlet that after meeting me for a short time opened the doors of his office and house for me. For his kind help with the moldyPSI software, for shearing his knowledge about condense matter theory and for showing me the lovely country where I life right now, Switzerland. My appreciation is extended to all people at PSI, for make me feel like at home during my stay.

I would like to thank the financial support from MICINN, (MAT2010-14907), 2011-2013 and la Generalitat de Catalunya (2009SGR01251), 2009-2013 and the support from BSC (FI-2012-1-0007) that support us with the capacity for developing bigger simulations. Moreover, special thanks to the department of Physics and Nuclear Engineering for grant me with the scholarship that allowed me to develop this work for the last 4 years.

I am deeply grateful to the people that shared all this time in the office: Estel, Anna, Isa, Gabriela, Ruxandra Jazmin, Francesc, Milad, Roger, Luis Fer, Chaoren, Fuqiang, Shervin, Marc, Victor, Juan Carlos and research group: Pere, Pep, Jorge i Trinitat, for their unconditional help and advises and for all the unforgettable moments we lived together.

All my thanks to those who helped in a direct or indirect way with their knowledge and encourage, thanks to all the professors and administration people. Specially to Toni Castillo and Jordi Lino that their knowledge was a great tool and great support.

I can not forget my friends that celebrate with me the good moment but where crucial for overcome the rugged ones. The list of names would be quite long, but they have been there for a long time and they know it. I would like to give thanks to all the people in Switzerland that made me feel like home and supported me in the last part.

Special thanks to my friend, flatmate, teammate, colleague, ... Estel Blay. Without his personal influence this work would had been infinity harder. You inspired me everyday for fighting for my dreams.

Finally, I couldn't finish without expressing my deep gratitude to my family, specially my parents and my brother. I can imagine it is not easy to support something that pushes away who you loves. Thank you for your unconditional support, your endless patient, for shear the values that lead me to reach my

dreams and fight for them.

Without any of you all this work would never had been possible.

Contents

List of Figures

List of Tables

Nomenclature

GK	Green-Kubo
η_1	Quenching rate 24.57/500 $[\varepsilon/(k_B\tau)]$ at Lennard-Jones potential
η_2	Quenching rate 24.57/5000 $[\varepsilon/(k_B\tau)]$ at Lennard-Jones potential
η_3	Quenching rate 24.57/50000 $[\varepsilon/(k_B\tau)]$ at Lennard-Jones potential
$\Phi_{ij}(r_{ij})$	Pair potential term with electrostatic core-core repulsion at EAM
$\rho(r)$	Material density
$\rho(r)$	Pair density
k_B	Boltzman constant
$P_{\alpha\beta}$	Independent component of the stress in the $\alpha\beta = xy, yz, zx$ direction
$v_i(t)$	Velocity for a i particle at a time t
α	Dimension of reciprocal distance. Constant at Morse Potential.
α_{11}	Dimension of reciprocal distance between atoms of type 1. Constant at Morse Potential.
α_{12}	Dimension of reciprocal distance between atoms of type 1 and type 2. Constant at Morse Potential.
α_{22}	Dimension of reciprocal distance between atoms of type 2. Constant at Morse Potential.
Δt	Time increment
η	Shear viscosity
η_0	Constant at shear viscosity
$\Gamma_{L,T}(q)$	Broadening of the excitation
μ	Friction factor at Nose-Hoover thermostat
ω_{BP}	Boson Peak frequency
ω_{IR}^{L}	Ioffe-Regel frequency for the longitudinal wave
ω_{IR}^{T}	Ioffe-Regel frequency for the transverse wave

ω	frequency
ω_{BP}	Boson Peak frequency
ω_D	Debye frequency
ω_D	Debye frequency
$\Omega_{L,T}(q)$	Characteristic frequency
$\overrightarrow{\varepsilon}$	Polarization vector
$\overrightarrow{k}$	Wave vector
$\overrightarrow{Q}$	Momentum of the phonons
$\overrightarrow{U}(r_N)$	Potential energy function between N particles
$\phi(r_{ij})$	Pair potential energy of two atoms i and j separated by a distance r_{ij} in Morse potential
σ	Length measurement at Lennard-Jones potential
τ	Time at Lennard-Jones potential
θ	One-half of the scattering angle
$\triangle P$	Pressure reduction at simulations
$\triangle r/r$	Atomic radius mismatch between elements
$\triangle T$	Temperature reduction at simulations
$\triangle_V$	Excess of volume
ε	Energy measurement at Lennard-Jones potential
ξ	Mean correlation length of elastic fluctuations
ξ_{IR}^L	Longitudinal Ioffe-Regel mean correlation length of elastic fluctuations
ξ_{IR}^T	Transverse Ioffe-Regel mean correlation length of elastic fluctuations
A	Activation temperature
$a(t)$	Particle acceleration at time t
a_0	Equilibrium lattice constant of the crystal.
c_1	Concentration atoms type 1
c_2	Concentration atoms type 2
c_L	Longitudinal sound speed
c_T	Transverse sound speed

$C_{xy}(t)$ Correlation function

$c_{L-Cu_{20}Pd_{80}}$ Longitudinal sound speed for $Cu_{20}Pd_{80}$

$c_{L-Cu_{50}Pd_{50}}$ Longitudinal sound speed for $Cu_{50}Pd_{50}$

$c_{T-Cu_{20}Pd_{80}}$ Transverse sound speed for $Cu_{20}Pd_{80}$

$c_{T-Cu_{50}Pd_{50}}$ Transverse sound speed for $Cu_{50}Pd_{50}$

D_{11} Energy of reciprocal distance between atoms of type 1. Constant at Morse Potential.

D_{12} Energy of reciprocal distance between atoms of type 1 and type 2. Constant at Morse Potential.

D_{22} Energy of reciprocal distance between atoms of type 2. Constant at Morse Potential.

E_{TOTAL} Total energy

$F_i(n_i)$ energy the ion core gets when it is embedded in the local electronic density at EAM

$g(\omega)$ Density of States

$g(r)$ Pair correlation function

h_{ck} Planck's constant

I_{BP} Boson Peak maximum intensity

I_{BP} Boson Peak maximum intensity

$j_\alpha(q,t)$ Current self correlation function

$j_L(q,t)$ Longitudinal current self correlation function

$j_T(q,t)$ Transverse self correlation function

L_i Box length in the coordinate direction i

m_A Mass atoms type A

m_B Mass atoms type B

m_i Mass for the particle i

$n_b(\beta E)$ Boson ocupation factor

n_i Integer i

n_i Ion density

P_f Final pressure at simulations

P_i Initial pressure at simulations

q_{BP} Boson Peak wave vector

q_{IR}^{L} Longitudinal Ioffe-Regel wave vector

q_{IR}^{T} Transverse Ioffe-Regel wave vector

q_m Position of the maximum of the static structure factor S(q)

$r(t)$ Particle position at time t

$r(t + \Delta t)$ Particle position at time t+ Δt

$r(t - \Delta t)$ Particle position at time t- Δt

r_c Cut off distance

r_e Equilibrium distance between the atoms i and j within the first nearest neighbour.

r_N Set on 3N particles coordinates

$S(q, \omega)$ Dynamic Structure Factor

$S_L(q, \omega)$ Longitudinal dynamic structure factor

$S_T(q, \omega)$ Transverse dynamic structure factor

T_0 Initial temperature at shear viscosity

T_D Debye temperature

T_f Final temperature at simulations

T_g Glass transition

T_i Initial temperature at simulations

T_m Melting temperature

U_1 One-body term potential energy function

U_2 Two- body term potential energy function or pair-potential function

U_3 Three-body term potential energy function

$v(t)$ Particle velocity at time t

V_a Atomic volume

V_{LJ} Lennard-Jones pair potential

V_m Specific volume of the cage

V_{void} Void space available for the atomic movement

<c> Averaged sound velocity

λ Wavelength of the X-rays

μm Micrometer

A Constant

Al- Aluminium

AMU Atomic Mass Units

BMG Bulk Metallic Glasses

BP Boson Peak

BSC Barcelona Supercomputing Center

C Specific heat

Ca- Calcium

Cu- Copper

D Energy of reciprocal distance. Constant at Morse Potential.

d Distance between the atomic planes

DHO Damping Harmonic Oscillator

E Energy

EAM Embedded Atom Method

eV Electronvolt

Fe- Iron

fs Femtosecond

HRTEM High Resolution Transmission Electron Microscope

INS Inelastic Neutron Scattering

IR Ioffe-Regel

IXS Inelastic X-ray Scattering

K	Kelvin
K/s	Kelvin per second
km/s	Kilometer per second
ksi	Kilo pound per square inch
L	Box length
LJ	Lennard Jones
LRO	Long Range Order
M	Box mass
m	Fragility
MD	Molecular Dynamics
Mg-	Magnesium
MPa	Megapascal
MPI	Message Passing Interface
MRO	Medium Range Order
N	Number of particles
n	Integer
NPT	Constant number of particles N, pressure P and temperature T
PBC	Periodic Boundary Conditions
PCF	Pair Correlation Function
Pd	Palladium
PSI	Paul Scherrer Institute
Pt	Platinum
Q	Mass associated to the friction factor at Nose-Hoover thermostat
q	wave vector
r	distance or separation between two particles in a Lennard-Jones potential
r	particle position

S(q)	Static structure factor
SEM	Scanning Electron Microscope
SRO	Short Range Order
T	Temperature
t	time
U	Potential energy function
V	Local free volume
V	intermolecular potential between two atoms or molecules
v	sound velocity
VACF	Velocity Autocorrelation function
VDOS	Vibrational Density of State
VFT	Vogel-Fulcher-Tammann
Zr-	Zirconium

Chapter 1

Introduction

The structural materials used in airframe and propulsion systems influence the cost, performance and safety of aircrafts, spacecrafts, etc. The knowledge of available materials, as well as their properties and reliability, is essential for the aerospace community.

Metallic glasses are metastable solids without the long-range order present in crystals. Conventional metallic materials have a crystalline structure consisting of single crystal grains of varying sizes that fit together to form the metal's microstructure. Metal alloys are usually obtained by melting and subsequent solidification; the particular cooling path, as well us further thermal treatments, are eventually responsible of the crystallization process and final metallic microstructure which, in turn, define the mechanic response.

Unlike crystalline alloys, bulk metallic glasses (BMG) are obtained by fast cooling below the crystallization temperature. Fast cooling prevents regular crystallization, and thus the material keeps the structure of the precursor liquid; bulk metallic glasses are thus solid materials with liquid-like structure at the atomic level. This non-crystalline structure makes bulk metallic glasses more resistant to permanent deformation than their crystalline counterparts - by factors of 2 or 3 – and tougher than ceramics.

The first metallic glass, discovered over fifty years ago by Pol Duwez at Caltech, was produced by rapid cooling an Au–Si eutectic liquid [1]. However, the extremely high critical cooling rate (e.g., 10^6 K/s) limited sample dimensions to the micrometer range, restricting applications to a few areas such as micro mechanisms in transformers and sensors. It was in the 1990s when a variety of alloy systems with low critical cooling rates, around 0.1–100 K/s [2, 3] , was discovered. This allowed the production of metallic glasses with dimensions of millimeters to centimeters via conventional casting technologies well known by metallurgists.

The disordered atomic structure of metallic glasses provides many superior mechanical properties compared to crystalline exemplars. For example, elastic strains up to 2% have been measured (most engineering metals exhibit 0.2% or less), with failure strengths approaching theoretical values; the strength-to-density ratio for Al- , Ca- , and Mg- based bulk metallic glasses is at least twice that of the corresponding crystalline materials. Most exciting is the development of new Fe- based bulk metallic glasses, so-called amorphous steels [4, 5] , which have exhibited failure strengths exceeding twice those measured for conventional

high strength steels. The combination of the unique mechanical properties with easy processability and shaping provides the potential for a new generation of structural materials with cutting-edge applications in a variety of industries including aerospace and aeronautics, high-performance sports equipment, armor and anti-armor devices, biomedical, and conventional structural applications [6].

The continuous research effort on bulk metallic glasses is resulting in the continuous appearing of new amorphous compositions for use in several applications - sports equipment, medical tools, military hardware, spacecraft parts, etc. -. Better measurements of viscosity and a better understanding of the atomic structure will help researchers to improve a variety of materials with a wide application range.

The macroscopic mechanical properties of a material are intimately linked to its atomic structure. The fracture behavior of brittle materials, in particular, is initiated by the generation of vibrational modes. In crystals, where periodicity is found in their structure, the vibrational states can be described as quantized plane-waves phonons, but in amorphous systems the nature of vibrations remains unclear. Their vibration spectrum strongly deviates from that expected from Debye's elasticity theory [7].

The structural and elastic heterogeneities present on glasses at the nm scale determine the physical properties at the mesoscale, this is the transition between the atomic level, defined by the particular atomic bonding of the substance, and the macroscopic elastic continuum [8, 9]. The nature of low frequency modes and how they are influenced by local atomic structure is unclear.

Amorphous materials exhibit a number of peculiar low temperature properties that strongly differ from the ones observed in crystalline systems. The specific heat, C , presents an excess $\propto T^3$ over the Debye prediction which appears as a maximum in C/T^3 . This excess is visible as a maximum, which is called Boson-Peak.

The so-called Boson Peak reflects an enhancement of states in the low frequency regime of the Vibrational Density of States and is believed to be the key to the fundamental understanding of the vibrational properties in metallic glasses.

The disordered atomic structure of glasses makes extremely difficult the experimental analysis of its atomic structure. Thus one of the principal tools in the theoretical study of metallic glasses is the simulation by molecular dynamics (MD). MD simulations are used to investigate the topology and structural dynamics of materials. Detailed simulations, based on first principles, give a precise description of the material but are restricted to moderate number of atoms due to their large computational cost. The use of empirical potentials allows faster calculations following only specific atomic degrees of freedom and, as a result, larger and more complex systems can be treated by allowing some reduction in accuracy. This is particularly important in the case of glasses, as the properties of the glassy state are consequence of the long range interaction of large number of atoms. In particular, the study of the Boson Peak can be performed by MD

1.1 Metallic Glasses

Metallic glasses are metastable solids without the long-range order present in crystals. They are emerging as potentially useful materials at the frontier of materials science research. They combine some advantages and avoid some of the problems of normal metals and glasses.

Amorphous metallic alloys or metallic glasses are relatively newcomers to the world of glasses, and they have properties that are unusual for metallic solids. Metallic glasses, which exist in very wide variety of compositions, combine fundamental interest with practical applications. They also serve as precursors for exciting new nano crystalline materials.

Amorphous alloys have attracted considerable attention due to their unique properties, such as mechanical, magnetic, electronic, chemical and other properties. Specially, their magnetic (soft and hard) and mechanical properties are of particular interest [10]. These properties make them candidates for fundamental studies in solid state physics as well as for industrial applications [11, 12, 13].

In the last two decades, metallic glasses have regained more interest due to the discovery of new glass-forming compositions with critical cooling rates below 100K/s, thus remaining glassy in bulk shapes. The availability of bulk metallic glasses allows their consideration for engineering applications. They offer an opportunity to reshape the field of structural materials with unfamiliar combinations of strength, elastic limit, toughness, wear resistance and corrosion resistance.

1.1.1 What are Metallic glasses?

A glass is a solid material produced when a liquid is cooled without crystallizing. Bulk Metallic Glasses (BMGs) are metallic alloys having amorphous or glassy structure.

When a conventional metal or alloy cools from the liquid melt, equilibrium is reached when it solidifies into the lowest energy state in a crystalline lattice. Most metals crystallize at a temperature just below the melting point in microseconds during solidification. But rather than forming a perfect single crystal, most metals are polycrystalline, with grains of varying shape and size. Grain boundaries and crystal defects represent weak spots of less than optimal atomic packing, where fracture can form and corrosion often starts.

A glass solidifies without crystallizing; it retains a much more disordered structure reminiscent of the liquid state. The disordered structure of glasses gives them unique properties, the most distinctive of which is the glass transition, T_g. A crystal will melt at a specific temperature when heated. A glass will not melt; instead, it gradually softens, changing from solid to liquid over a range of temperature as shown in Figure 1.1. This can be very useful for processing glasses into complex shapes.

1.1.2 Processing

Virtually any liquid can be turned into a glass if it is cooled quickly enough to avoid crystallization. The question is: how fast does the cooling need to be?

Common oxide glasses (such as ordinary window glass) are quite resistant to crystallization, they can be formed even cooling the liquid really slowly, and

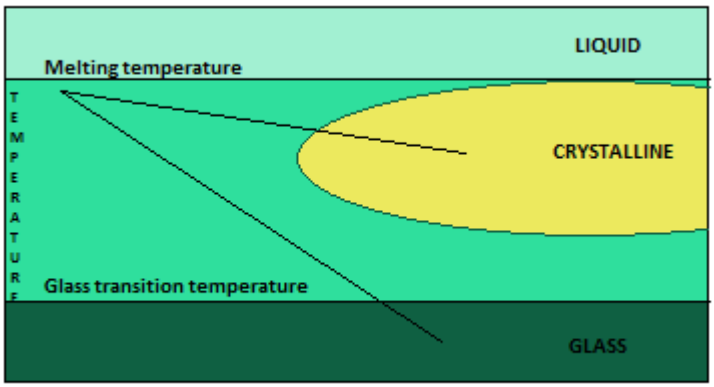

Figure 1.1: Glass transition.

many polymers cannot be crystallized at all. For both oxides and polymers, the key to glass formation is that the liquid structure cannot be rearranged to the more ordered crystalline structure in the time available. Metallic glasses, however, do not have these features. Because the structural units are individual atoms (as opposed to polymer chains or the network structure of an oxide), in most metallic alloys it is relatively easy for crystals to nucleate and grow. As a result, the earliest metallic glasses (which were discovered at Caltech in the late 1950s [1]) required very rapid cooling - around one million degrees Celsius per second - to avoid crystallization. Although this sounds impressive, it's actually not as hard to achieve. One way to do it is by single-roller melt spinning, as shown in Figure 1.2:

In this process, the alloy is melted (typically in a quartz crucible) by induction heating, and then forced out through a narrow nozzle onto the edge of a rapidly rotating chill wheel (typically made of copper). The melt spreads to form a thin ribbon, which cools rapidly because it is in contact with the copper wheel.

Melt spinning and other rapid solidification techniques have been used to make a wide variety of amorphous and nano crystalline metals from the 1960s to the present. However, materials produced in this way have a key limitation: At least one dimension must be very small, so that heat can be extracted quickly enough to achieve the necessary cooling rate. As a result, the early glass-forming alloys could only be produced as thin ribbons (typically around 50 μm thick), wires, foils, or powders. Although some applications (notably those that made use of the magnetic properties of iron- and nickel-based alloys) could use metallic glasses in these forms, structural applications were obviously impractical. The earliest demonstration of a bulk metallic glass came from Harvard University in the 1980s, where was shown that by using a flux to remove impurities, a palladium-based glass could be produced in thickness of more than a millimeter [2, 14]. More rapid progress was made in the early 1990s on developing alloys that could form glasses at much lower cooling rates, down to one degree Celsius per second or less. Today, a wide range of glass-forming alloys are known, based on common elements including iron, copper, titanium, magnesium, zirconium,

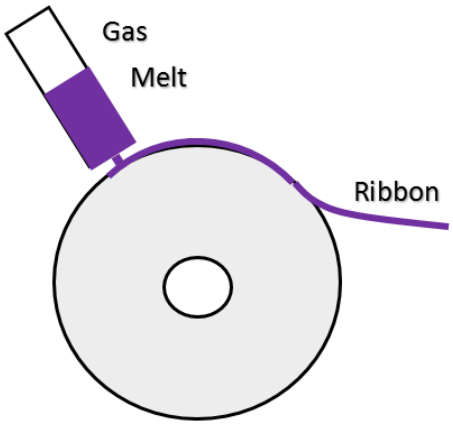

Figure 1.2: Single-roller melt spinning.

and platinum. These alloys can be produced using variations on standard metallurgical casting techniques, although in most cases processing must be done in vacuum or under an inert atmosphere to prevent contamination. Another technique suitable for producing metallic glasses is suction casting. An ingot in the upper chamber under an inert atmosphere is melted with an electric arc (much like in arc welding) and then sucked into a mold when the lower chamber is opened to vacuum, see Figure 1.3.

One of the potentially useful properties of metallic glasses is that they do not melt abruptly at a fixed temperature. Instead, like ordinary oxide glasses, they gradually soften and flow over a range of temperatures. By careful control of temperature, the viscosity of the softened glass can be precisely controlled. This ability can be used to form metallic glasses into complex shapes by techniques similar to those used for molding polymers.

1.1.3 Structure

In a crystal (Figure 1.4), there is a strong regularity or order in the atomic positions. In comparison, the atomic positions in a glass (Figure 1.5) lack the long range crystal periodicity.

There are several things to notice about these simple models. In the crystal, the local environment around each atom is the same. In the tho-dimensional hexagonal lattice of Figure 1.4 every atom has six neighbors, all at the same distance. In a close packed three dimensional lattice, each atom would have twelve neighbors. In the glass, different atoms will have a different number of neighbors, often below the expected average. Furthermore, the neighbors around a given atom are not all at the same distance, although an average near-neighbor distance can be defined. The same basic principles apply to real metallic glasses, but the situation is more complex because metallic glasses usually have more than one kind of atom.

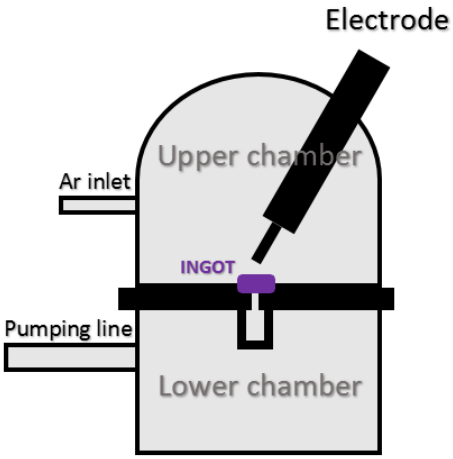

Figure 1.3: Suction casting.

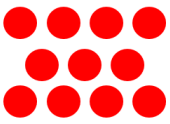

Figure 1.4: Crystal.

Figure 1.5: Amorphous.

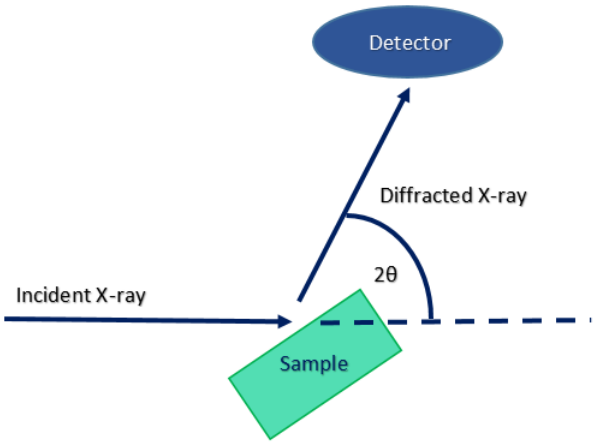

Figure 1.6: X-ray diffraction experiment.

We can study the atomic-scale structure of metallic glasses using some of the same techniques used to study crystalline materials. The most widely-used technique is X-ray diffraction. Because of their wave nature, X-rays will diffract from the regularly-spaced planes of atoms in a crystal, following Bragg's Law:

$$\sin\theta = \lambda/2d \tag{1.1}$$

where θ is one-half of the scattering angle, λ is the wavelength of the X-rays, and d is the distance between the atomic planes.

In an X-ray diffraction experiment, the intensity of the diffracted X-rays is measured as a function of θ, as shown schematically in Figure 1.6:

If Bragg's Law is satisfied, then X-rays will be strongly diffracted and a large intensity will be recorded. Because of the highly ordered nature of a crystal, this will happen only at a few angles. So the diffraction pattern from a crystal consists of a few, sharp diffraction peaks as shown in Figure 1.7 (top):

The disordered atomic-scale structure of a glass, however, leads to a diffraction pattern that has only a few, broad scattering, features as shown in Figure 1.7 (bottom).

The difference in structure can also be seen in the electron microscope. Figure 1.8 shows two (HRTEM) images. The left image shows the highly ordered contrast associated with the periodicity of a crystal; the right image corresponds to a glass, showing no periodic features.

1.1.4 Properties

1.1.4.1 Mechanical properties

Much of the recent interest in metallic glasses is due to their unusual and potentially useful mechanical properties [10, 15, 16]. The differences in behavior

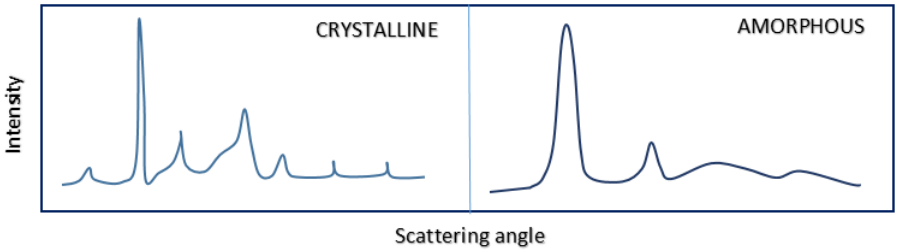

Figure 1.7: Diffraction pattern.

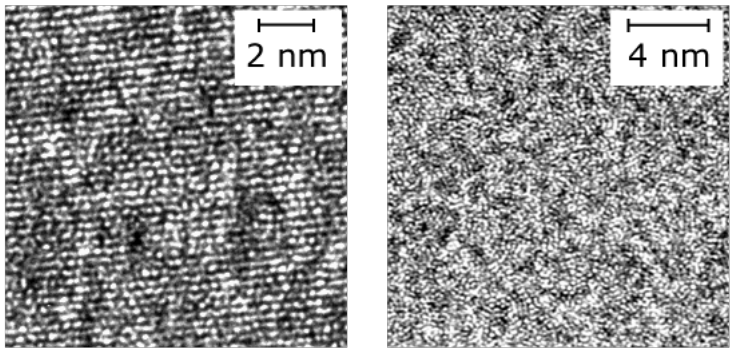

Figure 1.8: High resolution transmission electron microscope image (HRTEM).

ALLOY	Yield Strenght		Density		Strength to weigth ratio	Elongation (%)
	MPa	ksi	g cm^{-3}	Lb in^{-3}		
Metallicglasses						
$Zr_{41.25}Ti_{13.75}Cu_{12.5}Ni_{10}Be_{22.5}$	1900	275	6.1	0.22	310	2
$Mg_{65}Cu_{25}Tb_{10}$	700	100	4.0	0.14	175	1.5
$Fe_{59}Cr_6Mo_{14}C_{15}B_6$	3800	550	7.9	0.29	480	2
Conventionalalloys						
Aluminium (7075-T6)	505	73	2.8	0.1	180	11
Titanium (Ti-6Al-4V)	1100	160	4.4	0.16	250	10
Steel (4340)	1620	190	7.9	0.29	206	6
Magnesium (AZ80)	275	400	1.8	0.07	150	7

Table 1.1: Mechanical properties of Metallic glasses compared to some conventional alloys.

between metallic glasses and conventional, crystalline alloys result directly from the differences in their structures.

The strength and deformation behavior of a crystalline metal are ruled by the presence of defects in the crystalline structure, namely dislocations and grain boundaries. An amorphous material, such as a metallic glass, has neither grain boundaries or crystalline directions susceptible to generate dislocations and so its strength can approach the theoretical limit associated with the strength of its atomic bonds. Table 1.1 gives a comparison of the mechanical properties of some metallic glasses, along with a few conventional alloys for comparison:

It can be seen from the table that metallic glasses can in fact be quite strong. For instance, the iron-based glass in the table ($Fe_{59}Cr_6Mo_{14}C_{15}B_6$) is more than twice as strong as high-strength steel. As it might be expected, the high strength of metallic glasses has generated a high interest in them for structural applications.

Another consequence of the unusual structure of metallic glasses is that they are somewhat (20-30%) less stiff than similar crystalline alloys. ("Less stiff" means that in the elastic region they deform more, given the same amount of force.) Although this might seem undesirable, in some applications a less stiff alloy is actually advantageous. For instance, springs made of metallic glasses are springier. Another example would be orthopedic implants; in this case, if the implant material is much stiffer than the bone, the implant carries too much of the load and the bone becomes weaker (a response called "remodeling"). A metallic glass could be a better match than a crystalline alloy of similar composition, reducing the effects of remodeling.

Not all of the mechanical properties of metallic glasses are good. Notice the rightmost column of the table 1.1 above, "Plastic elongation", which is a measure of ductility, and it is a useful property of metals for two reasons. First, it means that metals can be formed into a wide variety of shapes by deformation processing (such as forging, rolling, and extrusion). Second, since the opposite of ductile behavior is brittle fracture, ductility is obviously desirable in any structural application. But from the table above we see that most of metallic glasses are not ductile, which is potentially a significant barrier to their

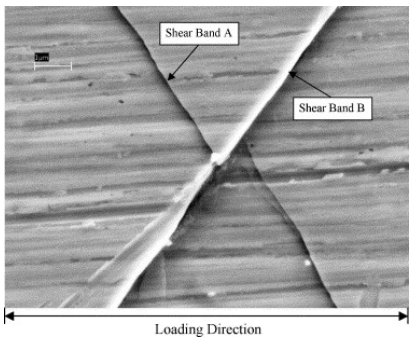

Figure 1.9: SEM picture of two shear bands crossing with each other on the $Zr_{52.5}Cu_{17.9}Ni_{14.6}Al_{10}Ti_{5.0}$.

widespread application.

Ironically, the same feature of metallic glasses that gives them their high strengths, the lack of dislocations, is also responsible for their lack of ductility. Dislocations cause strain hardening, which means that crystalline metals actually get stronger in response to deformation. Thus, if a small region of a crystalline metal deforms plastically, it gets stronger. Rather than continuing to deform in that same spot, deformation occurs someplace else which has not strain hardened and is therefore weaker. In this way, plastic deformation spreads through a relatively large volume of material. Metallic glasses have exactly the opposite response: their strain soften. So once plastic deformation sets in, it tends to continue in the same region, a process called shear localization. The result is the formation of shear bands, which are regions of highly localized plastic deformation [17], as seen in the SEM picture shown in Figure 1.9.

The image shows the surface of a metallic glass specimen subjected to bending, as seen in a scanning electron microscope. The deformation has caused shear bands to form on the surface of the specimen. There is extensive shear deformation on each shear band, but little deformation occurs in between the bands. The fracture could occur easily on the major shear band. The lack of tensile ductility in metallic glasses presents a potential problem for structural applications, where brittle behavior is undesirable. The problem is not quite as bad as it might seem, because despite their brittle behavior many metallic glasses still have reasonably good fracture toughness [18]. In addition, it is possible to achieve some ductility by making composite materials consisting of relatively soft, ductile crystalline metal particles or fibers embedded in a metallic glass matrix [19]. The particles both promote shear band formation and inhibit shear band propagation. Generating more shear bands might not seem like a good thing, but the idea is that many small shear bands are preferable to a single, large shear band that would cause fracture. One final consequence of the microstructure of metallic glasses is that they appear to be more susceptible to fatigue failure than conventional crystalline alloys. A simple explanation for this is that once a small crack forms, there are no micro structural features in a metallic glass to impede its growth under cyclic loading. It may be that fatigue performance of metallic glasses can also be improved by making a composite material, but to date there has been relatively little work in this area.

1.1.4.2 Magnetic properties

Despite the tremendous recent interest in the mechanical properties of metallic glasses, the most common real-world application of metallic glasses actually make use of the novel magnetic properties of some amorphous alloys based on iron, nickel, and cobalt. Although the saturation magnetization of these alloys is not as great as that of the pure elements, the lack of a crystalline structure can be an important advantage. In particular, amorphous alloys tend to have low coercivity because there are no boundaries between crystalline grains to impede the motion of magnetic domain walls and because there is no magneto crystalline anisotropy [20]. Furthermore, although metallic glasses are electrically conductive, their resistance to current flow is generally higher than that of crystalline alloys. This helps to minimize eddy-current losses that occur due to rapid magnetization and demagnetization of the material.

1.1.4.3 Other properties

Like crystalline metals, metallic glasses have free electrons to conduct electricity, which makes them both electrically and thermally conductive. However, compared to crystalline alloys they are not especially good conductors, due to their disordered atomic structure and high levels of alloying elements. Contrarily to common oxide glasses, metallic glasses are not transparent to visible light; their metallic character prevent so. Photons at visible wavelengths are strongly scattered and absorbed by the conduction electrons in metallic glasses. As a result, metallic glasses have the shiny luster typical of other metals and are not transparent.

Another common claim about metallic glasses is that they are resistant to corrosion, a property which is usually attributed to the lack of crystalline grain boundaries (which in ordinary crystalline metals can be particularly susceptible to chemical attack). The extension of solubility, respect to the crystalline phases, permits the homogeneous distribution of high concentrations of beneficial corrosion-resistant elements. One example of this strategy are the amorphous steels with high-contents of chromium [21]. It is true that some amorphous alloys are resistant to corrosion, but others are not, so any such claims should be treated with caution.

1.1.5 Glass forming criteria

In order to obtain amorphous structure from the liquid state the crystallization kinetics must be slowed down. According to Inoue [22], in order to obtain amorphous structures some criteria must be fulfilled:

- Multi-component alloys (three of more elements) increase the complexity and size of the crystal unit cell, resulting in a low energetic advantage of forming an ordered structure with long-range order.
- An atomic radius mismatch between elements, $\triangle r/r > 12\%$, leads to a higher packing density and smaller free volume and so smaller free energy difference between the stable crystalline phase and the supercooled melt.
- A negative heat of mixing between the main elements increases the energy barrier at the liquid-solid interface and decreases atomic diffusion. This retards local atomic rearrangements and the crystal nucleation rate.

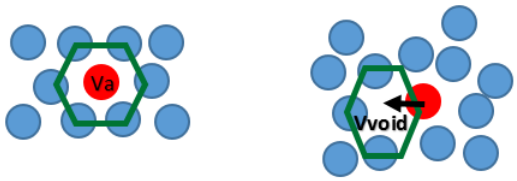

Figure 1.10: Free volume schematic representation.

• An alloy composition close to a deep eutectic forms a stable liquid phase at low temperature. Slower crystallization allows a decreased critical cooling rate and an increased size of the BMGs.

1.1.6 Free Volume

Free volume is defined as the excess of volume $\triangle_V$ which can be redistributed without energy change. In this section the free volume is defined for the case of a metallic glass.

Amorphous liquids display a complex relaxation path and transport properties near the glass transition T_g; the changes in free volume justify this behavior.

The free volume models based upon the theories of Cohen [23, 24, 25, 26] consider than an atom in a liquid state is trapped in a cage formed by its neighboring atom. This cage affects the atom movement conditioning it. Only when the space next to the atom is larger than the atomic volume, the atom can move into the liquid.

Figure 1.10 sketches the free volume around two atoms in a liquid. There, V_a corresponds to the atomic volume, V_m to the specific volume of the cage and V_{void} corresponds to the void space available for the atomic movement.

In order to allow atom's movement, void space should appear with a volume equal or bigger than the atomic volume ($V_{void} > V_a$).

A local free volume V for every atom is defined as $V = V_m - V_a$, and this local free volume can be redistributed between neighboring cages. When void spaces are greater than this V , atomic movement takes place by redistribution of the local free volume.

The free volume model can describe the thermodynamics for dense liquids and glasses in metastable equilibrium, but it does not give information about local atomic structure.

The local volume and specific geometry of the cage formed around individual atoms are not defined by free volume model.

1.1.7 Short Range Order

The structure of metallic glasses is characterized by their random long range structural order (LRO), although a considerable amount of short range order (SRO) [27, 28, 29, 30] is expected to be present in these alloys, due to their high atomic packing density and the varying chemical affinity between the constituent elements.

The first recognized structural model for metallic glasses is Bernal's [31, 32] dense random packing model. The atomic rearrangement is considered to be sphere packing using their atomic radius. This model is valid for mono-atomic metals and alloys where elements have similar atomic size. In spite of being one of the most accepted structural model, it does not provide any information about short range order (SRO) and medium range order (MRO) observed in glassy systems with more components and low critical cooling rate.

In general, atoms in glassy systems prefer to rearrange in SRO where the local nearest-neighbor environment of each atom is similar to other equivalent atoms, although this feature does not remain over considerable distance. This provides higher packing density and low free volume than their equivalent alloys. Finney[33] developed geometrical studies of two random packing models of high density by means of Voronoi polyhedral construction [34] obtaining a sensitive structural description.

The Voronoi tessellation method [34] split up the glass in Voronoi polyhedra around each atom, obtaining information about local volumes and nearest neighbor environment. The SRO of the amorphous samples is defined by the occurrence of certain types of Voronoi polyhedra.

In addition to Voronoi tessellation method applied by mean of Molecular dynamics, some experimental methods like X-ray and neutron diffraction [35, 36, 37, 38] are used to study the SRO in metallic glasses. Although it must be remarked that they give only averaged structural information in one dimension. MRO, can be defined as the next structural organization level beyond the SRO. It describes how Voronoi polyhedral are connected and arranged in a three-dimensional space.

1.2 Phonons

In the study of physical properties of solids, phonons play a major role.

A phonon is a collective excitation in a periodic elastic arrangement of atoms or molecules in condensed matter, such as solids and some liquids. The study of the propagation of phonons is an important tool to investigate the unexpected and baffling dynamic properties of amorphous solids.

In perfect crystals the vibrational motion of undamped atoms is easily decomposed into independent normal modes, therefore their vibrational excitations are generally well-understood. These normal modes are plane-wave excitations and are the already named phonons [39].

Phonons have associated a frequency (ω), wave-vector (q) and polarization vector. Anharmonic effects lead to a coupling between these modes resulting in a finite lifetime. In general crystal imperfections give rise to localized excitations which can also limit the phonon lifetime through elastic or inelastic scattering.

In amorphous solids, the situation is more complex and less understood. The

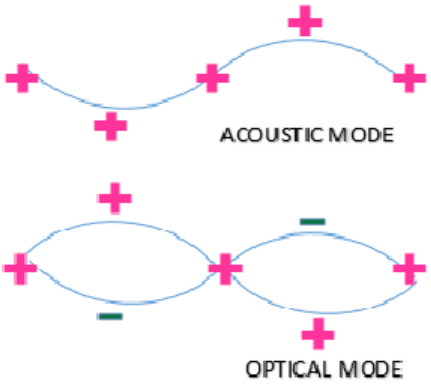

Figure 1.11: Phonons have energy (E), frequency (ω), wavelength (λ), wave vector (q) and propagate at a velocity v=ω/q.

lack of periodicity generates a complex situation. The normal modes can not be expressed as a normal waves, phonons are damped as in anharmonic crystals, and this effect is more important as the phonon wavelength approaches the interatomic spacing. Therefore, the dispersion curve in amorphous solids is smeared out increasing wave vector and phonons in the original sense pass away.

Anyhow, reaching the wavelength limit - at low frequencies -, glasses behave as elastic continua, like crystals. A well defined dispersion relation exists.

It must be taken into account that the fact that a system is in equilibrium does not mean absence of particle dynamics. Fluctuations appear continuously in the system. How fluctuations are able to disappear is an essential feature associated with the macroscopic behavior. This is an important reason for the study of the phonons of metallic glasses.

1.2.1 Debye model

In 1907 Einstein [40] made the first successful model to explain the behaviour of the specific heat C of solids at low temperatures. However, Einstein's model couldn't explain the behaviour when the temperature T approaches 0 K, where experimental data indicates that the specific heat is proportional to T^3 ($C \propto T^3$). In 1912 Peter Debye [41] developed a quantum mechanics theory for estimating the phonon contribution to specific heat in a solid.

Debye described the phonon oscillations of atoms as sound waves. Atomic movements are not isolated movements, there is a collective movement. So Debye quantized atomic movements as Planck quantized light waves.

Besides the difference on the velocity between speed of light and sound, there is one minor difference. Light is a transverse wave that contains two possible polarizations for each k, while, for sound there are three possible different modes (a longitudinal mode and two transverse modes).

In order to simplify this theory, it is assumed that the transverse and longitudinal modes have the same velocity, although longitudinal velocity is greater than transverse velocity.

We consider waves with Periodic Boundary Conditions, PBC. PBC, assume an infinite repetition of the solid in space. Let's consider, first, an one-dimensional solid in the x-coordinate direction; an one-dmensional wave, described for example by $\exp(ikx)$ must have the same amplitude in points equivalents by translation such as x and $x + L$, where L, is the box length. Then, this restricts the possible values of k to be

$$k = \frac{2\pi n}{L} \tag{1.2}$$

for n integer. In order to sum over all values of$k$, for$L$ large enough, this sum can be replaced by an integral

$$\sum \rightarrow \frac{L}{2\pi} \int dk \tag{1.3}$$

Expanding to three dimensions, a three-dimensional wave is described by $exp\left(i\overrightarrow{k}\cdot\overrightarrow{r}\right)$. By considering PBC the finite sample of size L^3 wraps onto itself in all three coordinate directions, generating a hypertorus. Moving a distance L in any direction, you get back to where you started. This implies

$$\overrightarrow{k} = \frac{2\pi}{L}(n_1, n_2, n_3) \tag{1.4}$$

for n_i integer

With this, the volume of every point is $(2\pi/L)^3$, and summing over every k we obtain

$$\sum \rightarrow \frac{L^3}{(2\pi)^3} \int dk \tag{1.5}$$

Let's suppose that oscillation modes are waves with frequency $\omega(\overrightarrow{k}) = v\left|\overrightarrow{k}\right|$ with v being the sound velocity. For each $\overrightarrow{k}$ there are three possible oscillation modes (one longitudinal and two transverse) . Taking this into account, an expression similar to Einstein's expression is obtained

$$< E >= 3\sum \hbar\omega\left(\left|\overrightarrow{k}\right|\right)\left(n_B\left[\beta\hbar\omega\left(\left|\overrightarrow{k}\right|\right)\right] + \frac{1}{2}\right) \tag{1.6}$$

$$< E >= 3\frac{L^3}{(2\pi)^3}\int dk\hbar\omega\left(\left|\overrightarrow{k}\right|\right)\left(n_B\left[\beta\hbar\omega\left(\left|\overrightarrow{k}\right|\right)\right] + \frac{1}{2}\right) \tag{1.7}$$

each excitation mode is a boson of frequency $\omega\left(\left|\overrightarrow{k}\right|\right)$ and it is occupied on average $n_B(\beta h\omega\left(\left|\overrightarrow{k}\right|\right))$ times, $n_B\left(\beta E\right)$ being the boson occupation factor, $\beta = {}^{1}/_{\mathrm{k_B T}}$ and k_B the Boltzmann constant.

Given the spherical symmetry, we can transform the three dimension integral to an one dimension integral

$$\int d\overrightarrow{k} \rightarrow 4\pi \int k^2 dk \tag{1.8}$$

where $k = \omega/v$. An open question on this expression are the integration limits. Though any wavenumber is possible, Debye assumed that the number of allowed excitations should coincide with the number of normal modes of vibration, which for a system of N atoms would be $3N$. This allows us to define a cutoff frequency, namely the Debye frequency, $\omega_d^3 = 6\pi^2 n v^3$, where n is the atomic density defined by $nL^3 = N$.

$$< E >= 3\frac{4\pi L^3}{(2\pi)^3}\int_o^{\omega_D}\frac{\omega^2 d\omega}{v^3}(\hbar\omega)(n_B(\beta\hbar\omega(k)) + \frac{1}{2}) \tag{1.9}$$

The Density of States is defined by

$$g(\omega) = N\left[\frac{12\pi\omega^2}{(2\pi)^3 n v^3}\right] = N\frac{9\omega^2}{\omega_d^3} \tag{1.10}$$

$$< E >= \int_o^{\omega_D} d\omega g(\omega)(\hbar\omega)(n_B(\beta\hbar\omega(k)) + \frac{1}{2}) \tag{1.11}$$

The density of Stated defines the number of oscillation modes with frequencies between ω and $\omega + d\omega$, therefore equation 1.11 represents the modes available for a frequency ω times the energy in each mode, integrated over all frequencies.

This result, reminders Planck's result for the quantum energy of light waves replacing $2/c^3 \rightarrow 3/v^3$. The factor 2 came from the number of modes in light and it is replaced by the number of modes available in sound waves.

The second difference between the two cases is the factor $+1/2$. This accounts for the zero point energy of each oscillator and gives us a contribution which is independent on temperature.

When the heat capacity is calculated $C = \frac{\partial < E >}{\partial T}$ the zero point energy does not affect, it can be ignored.

$$< E >= \frac{9N\hbar}{\omega_d^3}\int_o^{\omega_D} d\omega\frac{\omega^3}{\exp(\beta\hbar\omega) - 1} + E_0 \tag{1.12}$$

Defining $x = \beta\hbar\omega$, the Debye temperature from $\hbar\omega_d = k_B T_D$ and $x_D = T_D/T$ we get

$$< E >= \frac{9N\hbar}{\omega_d^3(\beta\hbar)^4}\int_o^{x_D} dx\frac{x^3}{\exp(x) - 1} + E_0 = \frac{9Nk_B T^4}{T_d^3}\int_o^{x_D} dx\frac{x^3}{\exp(x) - 1} + E_0 \tag{1.13}$$

The specific heat is then obtained by derivation against T:

$$C = \frac{\partial < E >}{\partial T} = \frac{9Nk_B T^4}{T_d^3}\int_o^{x_D} dx\frac{x^4}{(\exp(x) - 1)^2} \tag{1.14}$$

For high temperatures - $T > T_D$ - $\exp(x) - 1 \sim x$, and the specific heat approaches the classical value given by Dulong-Petit's law. For intermediate temperatures - $T \sim T_D$ the integral must be solved numerically. And, finally, for low temperatures - $T \ll T_D$ - $x_D = T_D/T \rightarrow \infty$; substituting x_D by ∞ the integral can be evaluated analytically, giving

$$C = Nk_B\frac{T^3 12\pi^4}{(T_D)^3 5} \tag{1.15}$$

which reproduces the experimental behaviour at low temperatures. The Debye model of specific heat reproduces qualitatively - and in some cases quantitatively the main features of the specific heat of solids. The observed differences affect mainly to metals, and are due to the contribution of electrons to the specific heat which are out of the scope of this work.

1.2.2 Boson Peak

Experimental measurements of the Vibrational Density of States (VDOS) in amorphous materials show a maximum above the standard Debye contribution at low frequency regimes. This maximum is commonly termed as Boson Peak (BP). In 3D systems it can be outlined by plotting the $VDOS/\omega^2$ versus ω, see Figure 1.12.

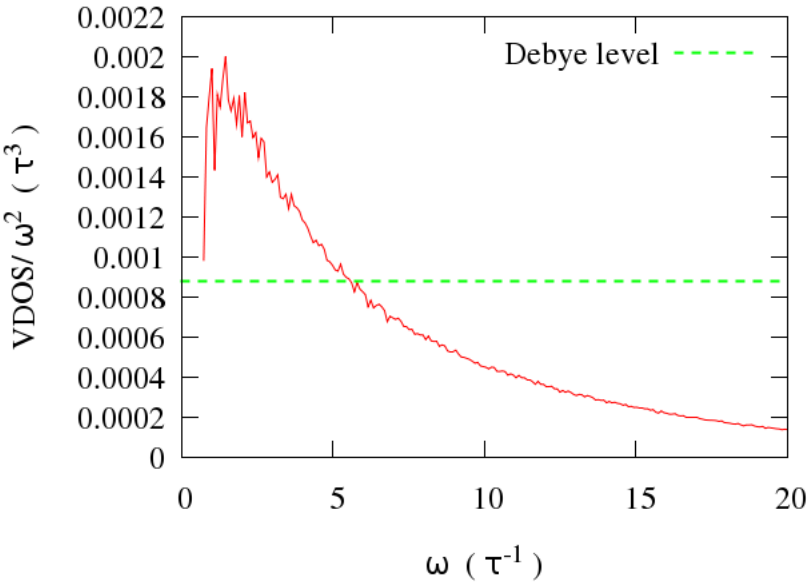

Figure 1.12: Boson Peak observed in a Lennard-Jones binary system of 1098500 atoms and quenching rate η_1.

It is generally accepted that the BP is associated to some sort of disorder in metallic glasses. The origin of the excess of vibrational modes is not clear. It appears to be connected to the so called quasi-localized eigen modes of the vibrational spectrum.

There have been proposed two main frameworks in order to understand the origin of the BP. On one hand, it is considered that the excess modes has a structural origin. The excess modes are localized and originated from defects or specific groups of atoms [42, 43].

On the other hand, the excess of modes may represent a counterpart of the van Hove singularity, which comes from transverse acoustic sound waves of the crystalline state. Constant random forces broaden and shift the singularity to lower frequencies.

Moreover, in the study of the origin of the BP some controversial issues have been found. The relation of the BP frequency to the Ioffe-Regel limit for transverse phonons limiting the frequency for the propagation nature of the transverse modes was studied by Shintani and Tanaka [44]. Ruffle, Ruocco et al. studied the existence of a strong damping for the acoustic modes with Ω^4frequency dependence near and above the BP [45, 46, 43]. Furthermore, the apparent sound velocity display a characteristic behaviour in the area where the BP occurs [47, 46, 7, 48, 49, 50]. Thus, the origin and features of the BP is still a very active field of research.

Chapter 2

Objectives

The purpose of this research work is to study the vibrational properties of metallic glasses by Molecular Dynamics (MD) simulation. Molecular Dynamics simulation consists in the integration of the equations of motion at the atomic scale. MD gives access to the atomic configuration and dynamics. This allows one to access the atomic topology and to correlate the microscopic state to the macroscopic features of the material. In the particular case of glasses, where the structure and dynamics of the material depend on the interaction at different scales, MD is one of the most powerful research tools available, though realistic simulations require a very large number of atoms.

The accuracy of MD depends on several factors. First, the interatomic interaction may be computed with different degrees of accuracy. Full quantum mechanics computations are possible but at a high computational cost. In order to save computing time, simplified or empirical potentials are often used. Second, a large number of atoms is needed to simulate collective phenomena. And, finally, the extremely high frequency of the atomic movement requires to simulate them on a very short time scale. Consequently, even using simplified empirical potentials MD simulation has a large computational cost.

Despite its computational cost, MD is a very powerful tool in the analysis of the dynamical properties of glasses. These properties depend on physical aspects, such as the quenching rate of the glass, and also on technical aspects, such as the size of the simulation box. In this work we will study the effect of these factors on the vibrational properties of metallic glasses by using different interatomic potentials. Lennard-Jones (LJ), Embedded Atom method (EAM) and Morse potentials will be used and compared. The Lennard-Jones potential has been largely used in the literature to describe the features of glasses, but the Embedded Atom method potentials are used in the simulation of the behaviour of crystalline materials, giving very precise results. Morse potentials are an intermediate option between them. Being still spherical simplified potentials, they give good results in the simulation of metallic systems.

Thus, the target of this work is to simulate glassy systems with different interatomic potentials, obtained at different quenching rates in boxes of different sizes, and to distinguish between the common features and those which are dependent on the parameters of the simulation. The dynamical properties, such as the dynamical structure factor and the Boson Peak will be computed and analyzed, and the results will be compared to the available experimental data.

Chapter 3

State of the art

The structure of metallic glasses (MG) has been a long standing challenge.

On one hand, MG are amorphous materials without long range order in their structure; on the other hand, short to medium range is expected to be pronounced due to their high atomic packing density.

The goal of the structural study of MGs is to extract statistical information about the glass structure to unveil the key features of the short and medium range order, and to identify the physical principles that constitute the structural basis of glass formation and glass properties. Different aspects have been already analyzed along the last years. In this work, we are interested in the collective dynamics in the MG. Elementary excitations such as phonons were extensively studied in crystalline materials by both experimental and theoretical techniques in the eighties, but the situation is very different for amorphous solids. In disordered systems, one cannot take advantage of the reciprocal-lattice vectors, and this is the main reason for the absence of experimental information on dynamic structure factors in glasses. As far as the Raman scattering is concerned, a large amount of experimental data is available on dielectric glasses mainly in the spectral region of the so-called 'boson peak', that is the energy region where the intermolecular modes are expected to dominate. Unfortunately, the interpretation of the Raman spectra of topologically disordered solids is controversial and this is basically due to the theoretical difficulty in disentangling the true dynamical effects from the frequency dependence of the photon excitation coupling.

Thus, in spite of the large efforts dedicated to the study of topologically disordered systems, the description of the microscopic dynamic of glasses is still poorly understood. It is, for example, quite difficult to obtain the dispersion relationship of phonons in a glass since only average quantities are known, such as the radial distribution function or the density. The dispersion relations of the crystal excitations can be measured, for example, by inelastic (coherent) neutron scattering. However, this technique, which is able to explore a large region of the energy- momentum plane, cannot access the low-q wavenumber region due to kinematic limitations. Of particular interest because wave vector is no longer a good quantum number, one would like to know how far out the dispersion curve can be followed and how the peaks in $S(q,\omega)$ broaden with increasing frequency.

Gary S. Grest, Sidney R. Nagel and A. Rahamn [51] calculated for the first

time the structure of the normal modes for a monoatomic closed packed glass.

Later, J.Hafner calculated the dynamical structure factor and the local vibrational density of state for a particular metallic glass $Ca_{70}Mg_{30}$ [52]. This study was performed via Molecular Dynamic Simulations in 2D models.

Other similar systems were studied later using more realistic potentials. R. N. Barnett, C. L. Cleveland and U. Landman [53] studied the glass transition, structure and dynamics of $Ca_{67}Mg_{33}$.

In the ninety's Wei Jin, Priya Vashishta and Rajiv K.Kalia [54] performed a study of the Dynamic structure factor and vibrational properties of the glass SiO_2. The structure was studied by experimental and theoretical methods. X-ray, neutron and NMR experiments were compared to the results obtained using molecular dynamics simulations in 2D systems.

In this period some other studies were performed. M. Sampoli, P. Benassi, R. Dell'anna, V. Mazzacurati and G. Ruocco [55] studied the low frequency atomic dynamics in a monoatomic Lennard-Jones glass.

On one hand, in 2008, H.Shintani and H. Tanaka [44] analyzed the boson peak that is believed to be the key to the fundamental understanding of the vibrational states of glassy and amorphous materials. The calculations were performed using molecular dynamic simulations and numerical methods. In this work some of the parameters of our interest were computed, but all of them in 2D systems or in small 3D systems. In their work 10 different configuration systems were used and averaged to obtain the final result. Moreover, in the study of the origin of the BP some controversial issues were found. The relation of the BP frequency to a limiting frequency for the propagation nature of the acoustic modes, the Ioffe-Regel limit.

On the other hand, P.M.Derlet, R. Maaß and J.F. Löffler studied the local atomic structure for 3D systems using numerical simulations and numerical methods [56]. In this work they investigated the nature of the low-frequency modes and how they are influenced by local atomic structure.

As mentioned before the BP is associated to some sort of disorder in metallic glasses with an unclear origin. In order to understand this origin of the BP, different frameworks have been proposed. In 2012, N. Jackse and A. Nassour studied the short-time dynamics of the $Cu_{50}Zr_{50}$ metallic glass. The structural origin of the BP is associated to the mean square displacement in low density defective local structures from Cu, Zr atoms. Moreover, B. Ruffle already pointed in 2006 that the boson-peak frequency is closely related with the Ioffe-Regel limit for sound in many glasses. They conjecture that this relation, specific to glassy materials, might be rather common among them. Ruffle, Ruocco et al. and Scopigno studied the existence of a strong damping for the acoustic modes with Ω^4 frequency dependence near and above the BP[45, 46, 43]. Furthermore, the apparent sound velocity display a characteristic behaviour in the area where the BP occurs. Ichitsubo studied experimentally for a Pd-based metallic glass how the sound velocity of nanometer wavelength exceeds that of millimeter wavelength [47].

Using inelastic x-ray scattering Scopigno studied, for first time, the dynamics of the first pseudo-Brillouin-zone.The momentum transfer dependence of the sound velocity and the acoustic damping of the glassy alloy $Ni_{33}Zr_{67}$ was defined. Specifically, the existence in this strong glass of well defined (in the Ioffe-Regel sense) acoustic-like excitations well above the boson peak energy was proved [46].

B. Ruta performed an experimental study of the high-frequency acoustic dynamics and a study of the vibrational density of states (VDOS) as a function of temperature in a glass. They found that the quasiharmonic temperature dependence of the acoustic dispersion curves offers a natural explanation for the observed scaling of the boson peak with the elastic medium properties [48].

At the same time and under collaboration, Baldi established a direct connection between the BP and the acoustic dispersion curves in vitreous silica. The apparent sound velocity shows a marked dispersion with frequency while the sound attenuation undergoes a crossover from a fourth to a second power law frequency dependence at the position of the BP [49] .

In 2011, P. Bruna, G. Baldi, E. Pineda, J. Serrano, J.B. Suck, D. Crespo, and G. Monaco studied the collective dynamics of the $Pd_{77}Si_{16.5}Cu_{6.5}$ metallic glass using high resolution X-ray scattering. The dispersion relation and the width of the acoustic excitations were determined showing how the longitudinal acoustic modes maintain their dispersive character for frequencies well above the boson peak frequencies. [50]

Moreover, the position and intensity of the BP was studied by M. Bauchy for densified silicate in small systems. For systems with lower density the BP intensity decreases an shift to higher frequencies [57] results that were already observed experimentally in silicate systems and polymers [58, 59, 60, 61].

Chapter 4

Methodology

In this chapter the methodology used will be explained in more detail. On the one hand, most of the work in this project is performed by using Molecular Dynamics simulations [62, 63, 64]. This part is addressed to describe the main functions implemented and the parameters used in the simulations.

On the other hand, in the discussion of the following chapter, the simulation results will be compared with experimental data from real metallic glass systems. Thus, some of the experimental techniques used to obtain the suitable experimental data are also described here.

4.1 Molecular dynamics

Molecular dynamics simulations are a major tool in the study of Metallic glasses. They are used for computing the equilibrium and transport properties [62, 64].

The results obtained from computer simulations are compared with analytical predictions and experimental data to test the accuracy of the models.

Moreover, they are used as a complement to conventional experiments or to gain a deeper insight on MG, carrying out simulations that are difficult or impossible in the laboratory (for example, working at extreme conditions of temperature or pressure). Molecular dynamics simulations also help one to understand experiments on a microscopic level. Molecular dynamic simulations can be considered and intermediate trade between experiments and theory, and provide a good test for theory. The predictions are 'exact' in the sense that they can be made as accurate as desired, subject mostly to the limitations imposed by the available computing infrastructure.

Molecular dynamics simulation is a technique of numerical integration of the Newton's equations of motion, for a specific interatomic potential, with given initial conditions and boundary conditions. This way it is possible to generate the atomic trajectories of the atoms in the system, allowing to access to the static and dynamic properties of the system.

Simulations can be treated like an experiment in which the system is adjusted until it reaches the desired condition, and then it is possible to compute property averages. In order to eliminate the influence of the initial conditions it is required to allow the system to evolve under stationary boundary conditions until the macroscopic properties of the system, such as average energy and box size, are

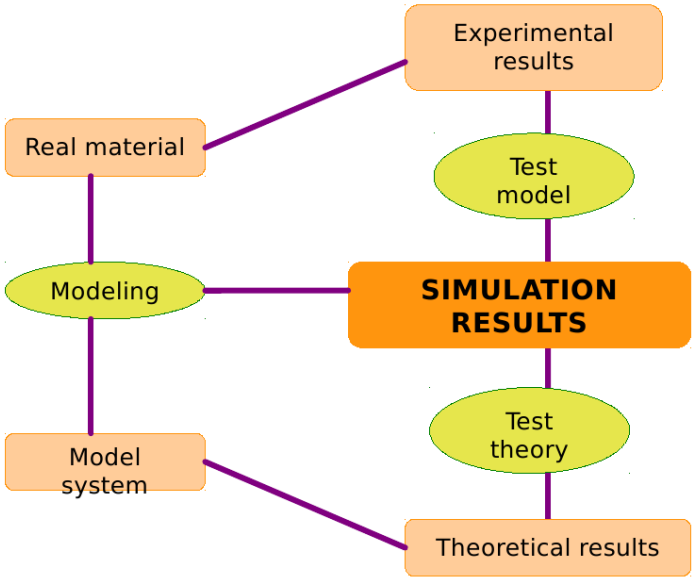

Figure 4.1: Molecular dynamics simulations diagram.

independent of time; this process is called equilibration. After equilibration, measurements can be performed, always taking into account that they have to be expressed in terms of the microscopic observables, namely position and moment of the system's particles.

4.1.1 Interatomic potentials

In order to use Molecular Dynamics Simulations the rules that define the atomic interactions in the system must be defined. These are given by the Schrödinger equation. Nowadays it is possible to integrate numerically the Schrödinger equations for a moderate number of atoms, thus obtaining the exact value of the energy of the system; this is called 'ab-initio' simulation, and is commonly used in quantum chemistry to resolve the structure of molecules. However, when collective properties are the subject of interest, ab-initio computations are extremely slow and thus impractical. Furthermore, interatomic forces are consequence of the interaction of the outer atomic orbitals only. Up to a reasonable level of accuracy, these interactions can be modeled with simple interatomic potentials, often analytical, which allow the simulation of a large number of particles with a moderate computational cost.

To obtain the potential functions for a particular system one can assume a functional form for the potential function and then adjust the parameters to reproduce a set of experimental data (Lennard-Jones [65], Morse [66]). Alternatively, one could try to determine the electronic wave function for fixed atomic positions. This second option becomes really complex for systems with many atoms. For this reason, different approximations are used and semi-empirical potentials are derived from quantum-mechanical arguments (EAM [67, 68]).

The choice of an appropriate potential can influence the results. The ac-

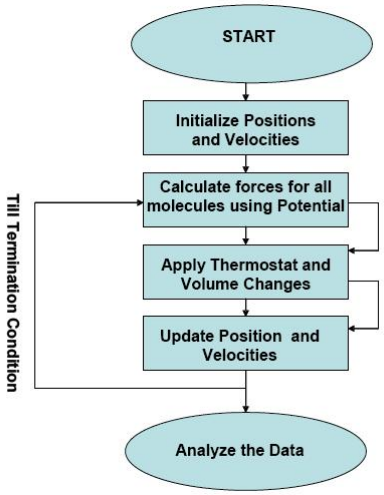

Figure 4.2: Molecular dynamics simulations process.

curacy, transferability and computational speed must be taken into account in order to study the problem.

In general, in Material Science where processes have a collective character and big systems are simulated for long periods, computing time is the limiting factor. In this case computational speed is relevant and simple potentials are used.

The forces in molecular dynamics are derived from a potential energy function U, which depend on the particle coordinates:

$$F_i = -\nabla \overrightarrow{U}(\overrightarrow{r}_1, \overrightarrow{r}_2, ..., \overrightarrow{r}_N) \tag{4.1}$$

The potential energy between N particles ,can be developed into terms that depend on individual atoms, pairs, triplets and so on :

$$\overrightarrow{U}(r_N) = \sum U_1(\overrightarrow{r}_i) + \sum\sum U_2(\overrightarrow{r}_i, \overrightarrow{r}_j) + \sum\sum\sum U_3(\overrightarrow{r}_i, \overrightarrow{r}_j, \overrightarrow{r}_k) + ... \tag{4.2}$$

where $r_N = (\overrightarrow{r}_1, \overrightarrow{r}_2, ..., \overrightarrow{r}_N)$ stands for the complete set on 3N particle coordinates, U_1corresponds to one-body term due to an external field or boundary conditions, U_2 is associated to two body term or pair-potential and it depends on the distance between the atoms without taking into account other atoms. U_3 is related with three-body term, when the interaction of a pair of atoms is modified by the presence of a third atom.

Mainly pair-wise interactions are considered because this contribution is the most significant. Therefore the total potential energy of the system of N atoms interacting via pair potential can be defined as:

$$\overrightarrow{U}(\overrightarrow{r}_1, \overrightarrow{r}_2, ..., \overrightarrow{r}_N) = \sum\sum U_2(r_{ij}) \tag{4.3}$$

where $r_{ij} = \mid \overrightarrow{r}_j - \overrightarrow{r}_i \mid$

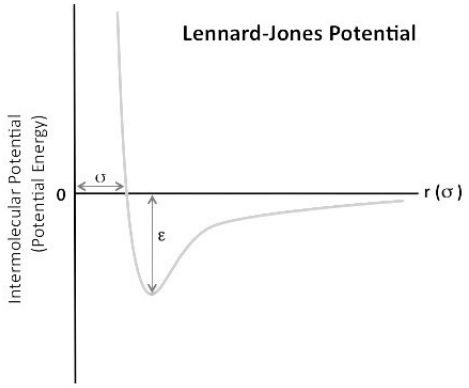

Figure 4.3: Lennard-Jones potential.

4.1.1.1 Lennard-Jones

The Lennard-Jones Potential (LJ) [65] is a mathematical approximation that exemplifies the interaction energy between two non-bonding atoms or molecules based on their distance of separation. The equation takes into account the difference between attractive forces and repulsive forces.

This potential is used often to model general effects rather than properties of a specific material.

Lennard-Jones is a pair-potential defined by:

$$V_{LJ} = 4\varepsilon \left[\left(\frac{\sigma}{r} \right)^{12} - \left(\frac{\sigma}{r} \right)^{6} \right] \tag{4.4}$$

where V is the intermolecular potential between the two atoms or molecules, ε is the energy well depth and σ is the distance at which the intermolecular potential between the two particles is zero and gives a measurement of how close two non-bonding particles can get; it is thus referred to as the Van der Waals radius. Finally, r is the distance of separation between both particles (measured between the center of both particles).

Note that the deeper the well depth ε the stronger the interactions between the two particles. When the bonding potential energy is equal to zero, the distance of the separation r will be equal to σ.

4.1.1.2 Morse

Morse potential is similar to Lennard-Jones potential but it is a more "bonding-type" potential and more suitable for cases when attractive interaction comes from the formation of a chemical bond. It is a popular potential for simulation of metals that have fcc and hcp structures [66, 69, 70, 71]. In a Morse potential,

the pair potential energy of two atoms i and j separated by a distance r_{ij} is given by

$$\phi(r_{ij}) = D\left[\exp(-2\alpha(r_{ij} - r_e)) - 2\exp(-\alpha(r_{ij} - r_e))\right] \tag{4.5}$$

where α and D are constants and they have respectively the dimension of reciprocal distance and energy. Both parameters are determined empirically for every element.

The parameter r_e is the equilibrium distance between the atoms i and j within the first nearest neighbor, and is given as $r_e = a_0/\sqrt{2}$, where a_0 is the equilibrium lattice constant of the crystal.

Several combining rules for Morse potential have been suggested [70]:

$$\left(\frac{D_{12}\alpha_{12}\exp(2\alpha_{12})}{4r_{e12}}\right)^{r_{e12}/\alpha_{12}} = \left(\frac{D_{11}\alpha_{11}\exp(2\alpha_{11})}{4r_{e11}}\right)^{r_{e11}/2\alpha_{11}} \left(\frac{D_{22}\alpha_{22}\exp(2\alpha_{22})}{4r_{e22}}\right)^{r_{e22}/\alpha_{22}} \tag{4.6}$$

$$\frac{r_{e12}}{\alpha_{12}} = \frac{1}{2}\left(\frac{r_{e11}}{\alpha_{11}} + \frac{r_{e22}}{\alpha_{22}}\right) \tag{4.7}$$

$$\frac{D_{12}}{4}\exp(r_{e12}\left(\frac{\alpha_{11}}{2r_{e11}} + \frac{\alpha_{22}}{2r_{e22}}\right)) = \frac{1}{4}\left(D_{11}\exp(\alpha 11)D_{22}\exp(\alpha 22)\right)^{1/2} \tag{4.8}$$

4.1.1.3 Embedded Atom Method (EAM)

The embedded atom method is a semi-empirical method based on the density-functional theory [3].

Semi-empirical potentials are an intermediate trade between simple Lennard-Jones and Morse potential and realistic ab-initio simulations. They capture the atomic potential behavior by considering explicitly only some atomic degrees of freedom, with a certain reduction in accuracy respect to ab-inito simulations.

The Embedded Atom Method was suggested by Daw and Baskes [67, 68] as a way to overcome the main problem with two-body potentials, the coordination independence of the bond strength, without increasing too much the computational time.

From density functional theory, the form for the total energy can be defined:

$$E_{TOTAL} = \frac{1}{2}\sum \Phi_{ij}(r_{ij}) + \sum F_i(n_i) \tag{4.9}$$

where $n_i = \sum \rho_j(r_{ij})$,$\Phi_{ij}(r_{ij})$ represents the pair potential term with the electrostatic core-core repulsion and $F_i(n_i)$ represents the energy won by the ion when it is "embedded" in the local electron density.

4.1.2 Boundary conditions

In Molecular dynamics simulations Periodic Boundary Conditions (PBC) are used to overcome the problem of surface effects. The macroscopic properties of a physical system are averaged on many millions of atoms; however, to simulate such amount of atoms is at present impossible. By molecular dynamics it is only possible to simulate only a small sample of it [62, 64].

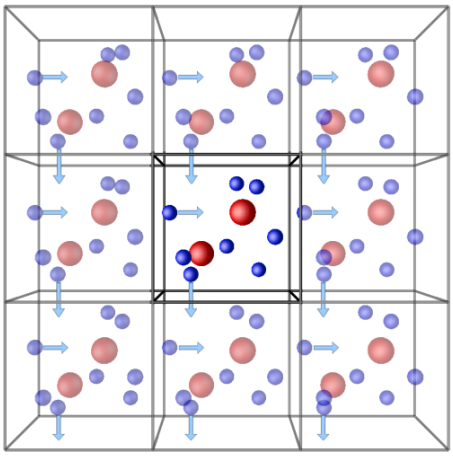

Figure 4.4: Periodic Boundary conditions in a simulation box. As a molecule leaves the central box, one of its images will enter through the opposite face.

PBC are used to simulate a large system by modeling a small part that is far from the edge. They are implemented for removing the surface effects implementing an infinite bulk surrounding.

The track of the N particles is studied in a cubic box. By imposing PBC the sample is replicated infinitely in each of the coordinate directions. In other words, spatial periodicity of length L_i is assumed, L_i being the length of the simulation box in the coordinate direction i. When a particle moves out from the simulation box by crossing one of the box walls, its periodic image moves into the simulation box by crossing the opposite wall. Thus, as a particle passes through one face of the unit cell, it reappears on the opposite face with the same velocity, as shown in 4.4[72].

This way, during the simulation only the properties of the unit cell need to be recorded, with the corresponding saving of memory space.

4.1.3 Equations of motion

Newton's equation of motion is integrated in order to obtain the velocity of the particles of the system [73, 62].

Time integration algorithms, are required to integrate the equation of motion of the interacting particles and follow their trajectory. The most commonly used time integration is the Verlet algorithm. In this case, the Verlet Velocity algorithm is used [74, 75].

The basic idea is to use Taylor expansion of the coordinates of a particle around time t.

$$r(t+\triangle t) = r(t) + v(t)\cdot\triangle t + \frac{1}{2}\cdot a(t)\cdot\triangle t^2 + \frac{1}{6}\cdot\dot{b(t)}\cdot\triangle t^3 + \mathcal{O}\left(\triangle t^4\right) \tag{4.10}$$

$$r(t-\triangle t) = r(t) - v(t)\cdot\triangle t + \frac{1}{2}\cdot a(t)\cdot\triangle t^2 - \frac{1}{6}\cdot\dot{b(t)}\cdot\triangle t^3 + \mathcal{O}\left(\triangle t^4\right) \tag{4.11}$$

Adding equation (4.10) and equation (4.11)

$$r(t+\triangle t) = 2r(t) - r(t-\triangle t) + a(t)\cdot\triangle t^2 + \mathcal{O}\left(\triangle t^4\right) \tag{4.12}$$

the truncation error is $\mathcal{O}(\triangle t^4)$. Using this expression and derivation, the velocity of the particle is:

$$v(t) = \frac{r(t+\triangle t) - r(t-\triangle t-)}{2\cdot\triangle t} + \mathcal{O}\left(\triangle t^4\right) \tag{4.13}$$

The velocity Verlet algorithm, it is a variant of the Verlet algorithm, although with small differences. It obtains positions at time $t+\triangle t$ using only positions at time t and their time derivation. In this case, there is no need for storing the positions from two previous steps. The equations are defined as:

$$r(t+\triangle t) = r(t) + v(t)\cdot\triangle t + \frac{1}{2}a(t)\cdot\triangle t^2 \tag{4.14}$$

$$v(t+{}^{\triangle t}/_2) = v(t) + \frac{1}{2}\cdot a(t)\cdot\triangle t \tag{4.15}$$

4.1.4 Nosé-Hoover thermostat and Parinello-Rahman barostat

Nose-Hoover thermostat [76, 77] and Parrinello-Rahman barostat [78, 79] are used to provide realistic fluctuations in temperature and pressure when the interest relies on the thermodynamic properties of a system.

Nose-Hoover thermostat is a method for controlling the temperature in molecular dynamics simulations. It uses a friction factor, μ, in order to control the velocity of the particles. This friction factor is the scaled velocity $d\mu/dt$ of an additional and dimensionless degree of freedom. The friction parameter is determined using a differential equation:

$$\frac{d\mu}{dt} = (\sum v_i^2 - 2\cdot N\cdot k_B\cdot T)/Q \tag{4.16}$$

where Q is a mass associated to the friction factor, which determines the strength of the thermostat.

The thermostat tries to reproduce the canonical phase-space distribution. In order to do this, modifies the equations of motion to include a non-Newtonian term in order to maintain the total kinetic energy constant.

The modified equations are given by:

$$\frac{d\overrightarrow{r_i}}{dt} = \frac{\overrightarrow{p_i}}{m} \tag{4.17}$$

$$\frac{d\overrightarrow{p_i}}{dt} = \overrightarrow{F_i} - \mu\overrightarrow{p_i} \tag{4.18}$$

The thermostat can be implemented using predictor-corrector method or a variation to Verlet Algorithm. The choice of Q is critical in the implementation of this thermostat.

The hydrostatic pressure applied to the system is controlled by using a barostat, such as the Parrinello-Rahman. Parinello and Rahman extended the

method initially proposed by Andersen [80]. The equations of movement of the individual particles are completed by a term which includes the potential energy stored by a volume submitted to an external pressure. Here, the volume is that of the simulation box V, and the pressure p is externally controlled. Andersen developed the equations for an orthogonal box; in this case, the motion equations become

$$\frac{d\overrightarrow{r_i}}{dt} = \frac{\overrightarrow{p_i}}{m_i} + \frac{1}{3}\overrightarrow{r_i}\frac{d\ln V}{dt}$$

$$\frac{d\overrightarrow{p_i}}{dt} = -\sum \hat{r}_{ij}U'\left(\overrightarrow{r_{ij}}\right) - \frac{1}{3}\overrightarrow{p_i}\frac{d\ln V}{dt}$$

$$\frac{Md^2V}{dt^2} = p_0 + \frac{1}{V}\left(\frac{2}{3}\sum\frac{p_i^2}{2m_i} - \frac{1}{3}\sum\overrightarrow{r_{ij}}U'\left(\overrightarrow{r_{ij}}\right)\right)$$

The new parameter M appearing here accounts for the *box mass*, which establishes the relaxation time of the system under pressure fluctuations. Andersen suggested that it should be chosen such as this relaxation time is of the order of the time L/c, where L is the length of the box and c the sound speed. However, static averages are independent of the value of M. Parrinello and Rahman modified the Andersen method to allow the box to change its shape, which is needed to allow crystallographic transformations in crystals. In the case of glasses, however, this is not needed and simulations can be performed in orthogonal boxes.

4.1.5 MoldyPSI software

At present there are several MD software implementations available. This work was performed by using the MoldyPSI software, developed by Dr. Peter Derlet from Paul Scherrer Institute (PSI) [81, 82], Switzerland. MoldyPSI is an extension of MOLDY/MDCASK, initially developed at the Lawrence Livermore National Laboratory [83]. MoldyPSI is written in FORTRAN and uses MPI to allow parallel processing. It can handle multimillion atom structures and computes several thousand time-steps with a reasonable computing cost. Simple interatomic potentials were used to simulate metallic glasses. Initially Lennard-Jones potentials were used, and further other potentials were implement, such as Morse potential and Embedded Atom Method potential.

Parallelization of the code is necessary to study large systems. The behavior of glasses is controlled by the collective interaction of a large number of atoms: to obtain more realistic results, simulations of metallic glasses must be performed at a really large atomic scale.

After a short stay at PSI, some additional subroutines were developed and implemented into MoldyPSI in order to allow the study of structural and vibrational properties.

For the parallelization of the code Open MPI libraries are used and the different routines in the program are adapted to this parallelization. The program was installed at Barcelona Supercomputing Center (BSC) [84] and large scale atomic simulations (up to 10 millions atoms) were performed.

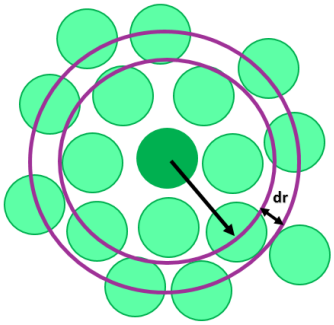

Figure 4.5: Atoms at a r distance from a given reference particle

4.2 Structural properties

Metallic glasses are solid metallic materials with a disordered atomic-scale structure. In order to ensure that we are studying an amorphous material it is important to check that the sample creation process (equilibration plus fast quench) produces a disordered structure, that is a metallic glass. Here we will recall the structural parameters that characterize the atomic structure.

4.2.1 Pair correlation function

Pair Correlation Function (PCF) infers information about the topology of the material. It describes how the atomic density varies as a function of the distance from a particular atom [62].

It is a measure of the spatial correlation between particles within a system. More specifically, it is measure of the average probability of finding a particle at a distance of r from a given reference particle, averaged over all particles of the system. For small r , $g(r) = 0$ indication that the width of the atoms limits their separation.

For three dimensions, this normalization is the number density of the system multiplied by the volume of the spherical shell. It can be expressed mathematically as:

$$g(r) = 4\pi \cdot r^2 \cdot \rho(r) \cdot dr \tag{4.19}$$

where ρ , is the number density.

The pair correlation function has distinguishable features for gas, liquid and solid [85]. In a gas, atoms are constantly moving, for this reason there are not prominent peaks. In contrast, in a liquid, one marked peak can be found easily, corresponding to the average first interatomic distance. Glasses show a similar pattern, as they keep the structure of the liquid. Finally, in a crystalline solid, different sharp peaks can be observed due to the reference network. Figure 4.6[86] shows an sketch of the pair correlation functions corresponding to the different states of matter.

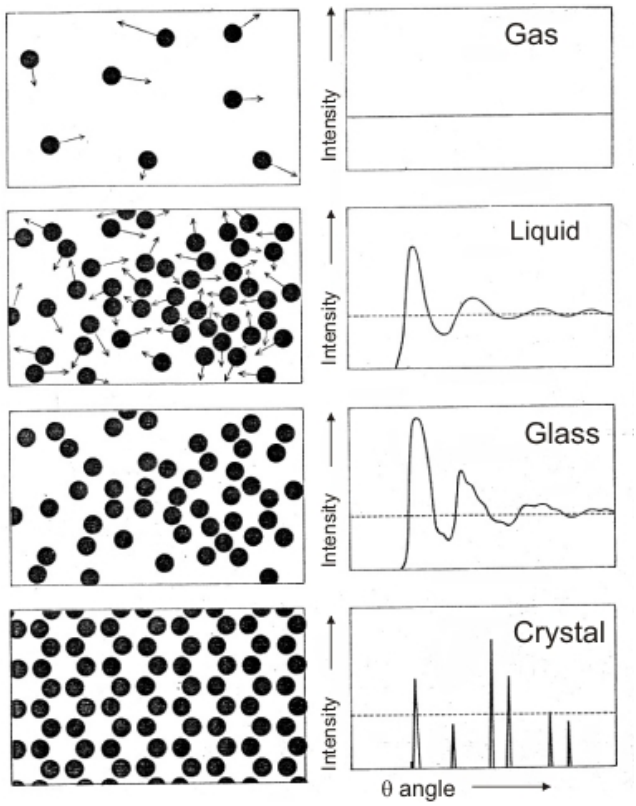

Figure 4.6: PCF for gaseous, liquid, glassy and solid state

In crystalline solids some peaks are observed indicating the atoms pack around each other in 'shells' of nearest neighbors. As r increases, the peaks are becoming weaker, due to the average over a large number of atoms in different crystallographic orientations that are at the same distance of the reference atom. Finally, for r large enough, PCF tends to 1, corresponding to the macroscopic density of the material.

This characteristic features of the PCF are useful for checking the disordered structure in metallic glasses.

4.2.2 Static Structure factor

The static structure factor, $S(q)$, can be calculated in different computational ways and can be measured with diffraction techniques.

The $S(q)$ can be defined in terms of the real-space pair density via the sinus Fourier transform [87].

$$S(q) = 1 + \frac{4\pi\rho}{q}\int [g(r) - 1]sin(qr)dr \tag{4.20}$$

where q, is the magnitude of the momentum transfer vector, and ρ is the number density of the material.

In the same way than with the pair correlation function, the static structure factor has some key features for liquids and amorphous structures. Crystalline solids show well defined peaks, corresponding to the well defined interatomic distances in the crystal. The positions of the peaks r_i and q_i shown in both $g(r)$ and $S(q)$ satisfy the Bragg condition, namely $q_i r_i = 2\pi$. As q increases, $S(q)$ approaches to 1.

Liquids, and consequently also glasses, have no well defined interatomic distances; as shown by the pair correlation function, they have a continuous distribution of interatomic distances. Their static structure factor shows also a few broad peaks, which satisfy also the Bragg condition; thus, the maximum of the first peak of $S(q)$ appears at $q_1 = 2\pi/r_1$, r_1 being the position of the maximum of the first peak of $g(r)$. These features are useful in order to check the true amorphous structure present in metallic glasses, both in MD simulations and experimentally. The absence of Bragg peaks in X-ray and neutron diffraction reveals also the amorphous structure in metallic glasses [39].

4.3 Vibrational properties

In a crystal where periodicity is present, vibrational states can be well understood as plane-wave phonons modes, but in disordered systems vibrational states remain elusive.

The vibrational properties of Bulk Metallic Glasses are directly related to their thermodynamic and kinetic properties. Their general trends are those of glasses and, in particular, an excess of vibrational modes appears at low frequencies. This is the so-called Boson Peak, related to the Debye level, and has been reported in a large number of glasses.

The vibrational properties of a material are manifested in the dynamic structure factor and in the vibrational density of states.

4.3.1 Dynamic Structure factor

The dynamic structure factor, $S(\overrightarrow{q},\omega)$, contains information about the time evolution of the inter-particle correlation. $S(\overrightarrow{q},\omega)$ can be derived from the Fourier transform of the self-correlation function of the current $j_\alpha(\overrightarrow{q},t)$ [88], that is:

$$S_\alpha(\overrightarrow{q},\omega) = \frac{\overrightarrow{q}\cdot\overrightarrow{q}}{2\pi\omega^2 N}\int dt < j_\alpha(\overrightarrow{q},t)\cdot j_\alpha(-\overrightarrow{q},0) > \exp(i\omega t) \tag{4.21}$$

where α is L for the longitudinal case or T for the transverse case. These currents are defined as:

$$j_L(\overrightarrow{q},t) = \sum (v_i(t)\cdot\hat{q})\,\hat{q}\exp(i\overrightarrow{q}\cdot\overrightarrow{r_i}(t)) \tag{4.22}$$

$$j_T(\overrightarrow{q},t) = \sum (v_i(t) - (v_i(t)\cdot\hat{q})\,\hat{q})\exp(i\overrightarrow{q}\cdot\overrightarrow{r_i}(t)) \tag{4.23}$$

where $v_i(t)$ is the velocity of the i-th particle at a time t and $\hat{q} = \frac{\overrightarrow{q}}{|\overrightarrow{q}|}$.

In a crystalline solid, $S_\alpha(\overrightarrow{q},\omega)$ shows discrete peaks in each crystalline direction at the frequency ω of the different allowed - longitudinal or transverse -

phonons of wavevector $\overrightarrow{q}$. The corresponding relation between ω and $\overrightarrow{q}$ gives the phonon relation of dispersion of the material. In non-crystalline materials all crystalline directions are equivalent, and the discrete peaks are replaced by a distribution of allowed frequencies; $S_\alpha(\overrightarrow{q},\omega)$ loses its vectorial dependence and becomes $S_\alpha(q,\omega)$. The phonon relation of dispersion is then determined by the frequency of the maximum intensity of phonons. However, given this distribution of allowed frequencies for each wavenumber q, one would like to know how far out the dispersion curve can be followed and how the peaks in $S(q,\omega)$ broaden with increasing the temperature.

4.3.2 Vibrational Density of States (VDOS)

The Vibrational Density of States (VDOS) describes the preferred states of the system and reveals the underlying features of the dynamical processes.

It is computed through the velocity autocorrelation function (VACF) [89].

$$\frac{<\overrightarrow{v}(t)\cdot\overrightarrow{v}(0)>}{<\overrightarrow{v}(0)\cdot\overrightarrow{v}(0)>} \tag{4.24}$$

Using the MD trajectories at temperature T, the VDOS $D(\omega)$ can be calculated by Fourier transforming the velocity auto-correlation function, that is:

$$D_{FFT}(\omega) = \sum D_i(\omega) = \sum \frac{m_i}{2Nk_BT}\int <\overrightarrow{v_i}(t)\cdot\overrightarrow{v_i}(0)> \exp(i\omega t)dt \tag{4.25}$$

where m_i is the mass for the i particle, T is the temperature, k_B is the Boltzmann constant and ω the frequency [44] .

4.4 Viscosity

The viscosity of a fluid is a measure of its resistance to gradual deformation by shear stress or tensile stress and it is easy to determine by experiments. It is inverse to the relaxation time of the fluid.

In Molecular dynamic simulations, the shear viscosity of a liquid is related to the fluctuations of the off-diagonal elements of the pressure or stress tensor. Viscosity can thus be calculated in stationary conditions - constant T and P - through the pressure fluctuations.

The Green-Kubo (GK) expression allows to compute the shear viscosity by integration of the stress (pressure) autocorrelation function [90, 91]. That is

$$\eta = \frac{V}{k_BT}\int \left\langle \sum P_{\alpha\beta}(t)\cdot P_{\alpha\beta}(0)\right\rangle dt \tag{4.26}$$

where η is the shear viscosity, V is the volume of the system, T is the temperature, k_B is Boltzmann's constant, and $P_{\alpha\beta}$ refers to an independent component of the stress in the $\alpha\beta = xy, yz, zx$ direction.

This formulation takes into account the contribution of all atoms into an unique correlation function, for example

$$C_{xy}(t) = \left\langle \sum P_{xy}(t)\cdot P_{xy}(0)\right\rangle dt \tag{4.27}$$

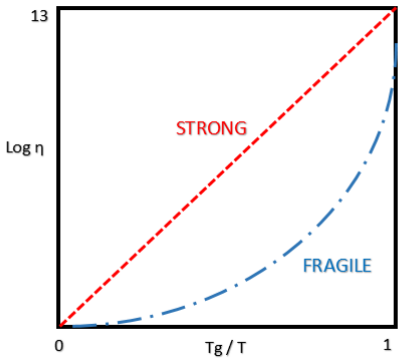

Figure 4.7: Logarithm of the viscosity vs. T_g/T for a strong and a fragile glass former. Fragility increases with the slope of curve at $T = T_g$. This plot is commonly know as *Angell plot*.

The transition of a liquid into a glass is controlled by the behavior of the viscosity as temperature decreases. At high temperatures, the relaxation time follows and Arrhenius dependence.

$$\tau = \tau_0 \exp\left(-\frac{A}{T}\right)$$

where τ is the infinite temperature relaxation time and A is a constant. When the temperature is decreased, this relaxation time deviates from Arrhenius dependence to the Vogel-Fulcher-Tammann law. In terms of viscosity, the Vogel-Fulcher-Tammann (VFT) [92] reads:

$$\eta = \eta_0 \exp(A/T - T_0) \tag{4.28}$$

where η_0, A and T_0 are constants. The VFT expression reduces to the Arrhenius dependence when $T_0 \to 0$.

The fragility concept was proposed to classify materials according to the temperature dependence of their kinetics in the liquid and supercooled liquid state. Fragility reflects the degree of departure of the viscosity (or relaxation time) with temperature from the Arrhenius behavior. This concept was originally proposed by Austen Angell [93].

The most common definition of fragility characterizes the slope of the viscosity (or relaxation time) of a material with temperature as it approaches the glass transition temperature from above [93]:

$$m = \frac{\partial log_{10}\eta}{\partial(T/T)_{T=T_g}} \tag{4.29}$$

where T_g is the glass transition temperature, m is fragility, and T is temperature.

Glass-formers with a high fragility are called "fragile"; those with a low fragility are called "strong".

4.5 Inelastic X-ray Scattering (IXS)

As previously mentioned, molecular dynamics simulations are an intermediate trade between experiments and theory, for this reason most of the results obtained can be compared and checked with the results obtained from experiments.

Inelastic X-ray scattering is a technique used in condensed matter to study atomic and molecular motion.

An X-ray beam is monochromatized and then focused at the sample stage. After colliding with the sample, the radiation is scattered in every direction. A particular scattering angle is chosen and the energy of the scattered radiation is analyzed in a spectrometer. In order to scan energies the temperature of the monochromator is varied in the range of mK, while the temperature of the subsequent energy analyzer is kept constant [94]. Finally, the spectrometer consists on the above cited crystal analyzer and a detector. (Figure 4.9).

The incident and scattered photons from the beam are characterized by their energy E, wave vector $\overrightarrow{k}$, and polarization vector $\overrightarrow{\varepsilon}$. The momentum and energy conservation laws impose that:

$$\overrightarrow{Q} = \overrightarrow{k_i} - \overrightarrow{k_f} \tag{4.30}$$

$$E = E_i - E_f \tag{4.31}$$

$$Q^2 = k_i^2 + k_f^2 - 2 \cdot k_i \cdot k_f \cos(\theta) \tag{4.32}$$

where $\overrightarrow{Q}$ and E are the momentum and energy of the phonon respectively, and θ is the scattering angle between the incident and scattered photons (Figure 4.10).

In the case of photons, the momentum and energy are related by $E(k) = \hbar ck$. Taking into account that the energy that the photon looses or gains associated to phonon excitations is always much smaller than the energy of the incident photon $E \ll E_i$, $k_i \cong k_f$ we obtain that:

$$\frac{Q}{k_i} = 2k_i sin\left(\frac{\theta}{2}\right) \tag{4.33}$$

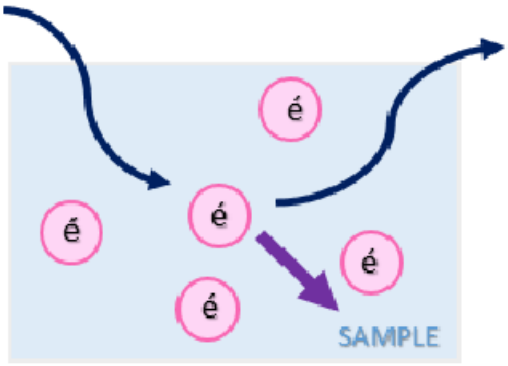

Figure 4.8: Collision between the X-rays and the sample.

Inelastic X-ray Scattering (IXS) is the only method to gain information on the high frequency collective dynamics in Metallic Glasses due to their usually high longitudinal sound speeds. Trough X-ray Scattering one can obtain information about the elastic and inelastic excitations. It covers the intensity region for the study of the acoustic excitations in amorphous systems. Results are presented as the $S(q, \omega)$, which is the space and time Fourier transform of the density-density correlation function.

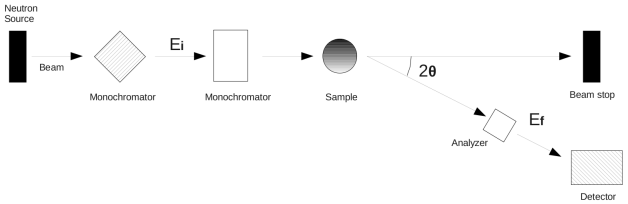

Figure 4.9: Experimental setup.

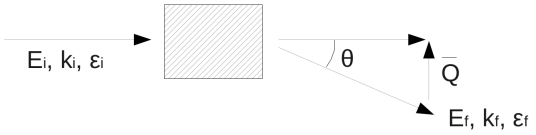

Figure 4.10: Schema of the Inelastic Scattering process.

Chapter 5

Results

The choice of the right potential and simulation parameters can effect the results. In this chapter, the results of Molecular Dynamic simulations preformed using the different potentials defined before are presented.

This chapter is structured in three parts according to the three different potentials used. In every chapter, the results obtained for the different potentials are shown and compared with each other to see the difference effects of the potential election. The results presented in this section are a selection of the complete set of results obtained for all system sizes, quenching rates and potentials. The whole set of results is presented in the Appendix and some further analysis of the results and comparison with the data obtained from experiments is given in the Discussion section.

5.1 Lennard-Jones systems

The Lennard-Jones potential (LJ) is one of the simplest potential that faithfully represents the essentials physics of interacting atoms having a small computational cost. This chapter displays the results obtained by using this potential.

The Lennard-Jones potential is an analytical potential defined as

$$V_{LJ}(r) = 4\varepsilon \left[\left(\frac{\sigma}{r}\right)^{12} - \left(\frac{\sigma}{r}\right)^{6} \right] \tag{5.1}$$

where σ and ε define the length and energy scales of the potential. The minimum potential energy is obtained at $2^{1/6}\sigma = 1.12\sigma$, and the depth of the potential well is ε, see Figure 5.1.

The Lennard-Jones potential is a soft, long range potential. It was designed to model the Van der Waals interactions between neutral atoms; however, it has been used as a model potential in many other cases and, in particular, in the study of glasses and the glass transition.

Molecular Dynamic simulations were performed on binary Lennard-Jones systems. All simulations were carried out at constant pressure and temperature (NPT). Periodic Boundary conditions were used for the study of all systems.

Wahnström parametrization was used [95], where $\varepsilon = 1$, $\sigma_{AA} = 1$, $\sigma_{AB} = \sigma_{BA} = 11/12$, $\sigma_{BB} = 5/6$ and cut-off distance $r_c = 2.5\sigma$. The masses of the LJ

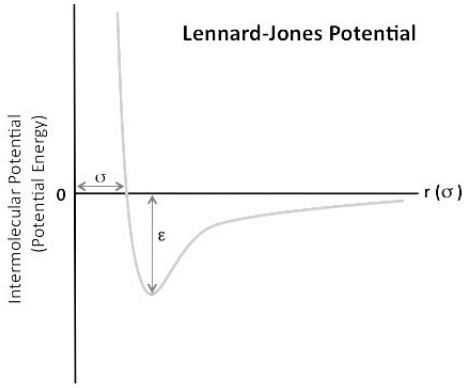

Figure 5.1: Lennard-Jones potential.

particles are taken as $m_A = 2$ and $m_B = 1$ and concentrations $c_B = 0.8$ and $c_B = 0.2$.

The results are reported in reduced units, following the standard convention when using LJ potentials. Energy is measured in ε, length in $\sigma_{AA} = \sigma$, temperatures in ε/k_B and time in $\tau = (m_A\sigma_{AA}^2/\varepsilon)^{1/2} = (m\sigma^2/\varepsilon)^{1/2}$.

5.1.1 Quenching procedure

Glasses are obtained from a melt by quenching. In order to obtain amorphous samples for computing the structural and vibrational properties, some well equilibrated liquid configurations at initial temperature $T_i = 10000 \cdot k_B[\varepsilon/k_B]$ and hydrostatic pressure $P_i = 8/160[\varepsilon/\sigma_{AA}^3]$ were prepared. The simulation time step is $\triangle t = 6.95 \cdot 10^{-4}[\tau]$.

After equilibrating the liquid configuration at these conditions, systems were quenched applying different quenching rates. Temperature and pressure were reduced periodically at a given time interval. The reduction for the temperature is chosen to be $\triangle T = -198.0 \cdot k_B[\varepsilon/k_B]$ and pressure $\triangle P = -0.158/160[\varepsilon/\sigma_{AA}^3]$ and applied every 500, 5000 and 50000 timesteps. The corresponding quench rates are $\eta_1 = 24.57/500$, $\eta_2 = 24.57/5000$ and $\eta_3 = 24.57/50000$ $[\varepsilon/(k_B\tau)]$. A Parinello-Rahman [79, 78] barostat is used to evolve the response of the periodic side length to the applied hydrostatic pressure and an Nose-Hoover [96] thermostat is used for the control of the temperature. After the quenching procedure, the samples at $T_f = 100 \cdot k_B[\varepsilon/k_B]$ and pressure $P_f = 0.1/160[\varepsilon/\sigma_{AA}^3]$ were relaxed to 1K and 0 hydrostatic pressure and equilibrated again.

For a first analysis of the properties and development of the code some sets of simulations were considered for N=1728, 13824 and 110592 atoms. After this, in order to be able to analyze lower frequency ranges, bigger systems were studied, N=1098500, 2048000, 3764768 and 5470524 atoms.

5.1.2 Glass transition

Along the quenching process a reduction of the pressure and temperature is applied. The effect of both reductions is significant in the average volume per atom. The temperature reduction results in a reduction in the average atomic volume, while the reduction on pressure allows an increase of the average atomic volume. In the conditions chosen in this work the dominant effect is the reduction of atomic volume due to the temperature reduction.

When the temperature is decreased below the melting temperature (T_m) of the material, the system enters the region where crystalline state is thermodynamicalle stable. For low quenching rates the material crystallizes. The developed crystalline structure has usually a lower average volume per atom. Crystallization is a first order phase transition showing a discontinuity in the thermodynamic variables and, in particular, in the atomic volume. On the contrary, if the quench rate is high enough - above some critical quenching rate - the material can reach temperatures below T_m, becoming a supercooled liquid. Here, the viscosity of the liquid increases too fast and prevents crystallization. Further, at lower temperatures, the atomic structure of the liquid is frozen and the material becomes an amorphous solid, a glass. The glass transition is not itself a phase transition. It is rather a kinetic phenomenon, as the atomic mobility decreases until a level in which no macroscopic changes can be observed in the laboratory time-scale. From the thermodynamic point of view, the glass is in a metastable state, but the characteristic time for evolution is, for practical purposes, infinite.

The glass transition can be visualized on the behavior of the average volume per atom. Figure 5.2 shows the behavior of the atomic volume in a simulation of a LJ mixture along the glass transition temperature (T_g). T_g can be determined from the intersection of the extrapolated linear behaviors of the atomic volume in the supercooled melt and the glass.

Given the kinetic origin of the glass transition, the determined value of T_g depends on the quenching rate. In fact, this dependence allows to determine the activation energy of the glass transition.

5.1.3 Amorphous structure

In order to check the amorphous structure of the samples the static structure factor, $S(q)$, and the pair correlation function, PCF, were calculated for every system after quenching.

The pair correlation function, shown in Figure 5.3, displays a first sharp peak at $r \sim \sigma$ splitted in three contributions corresponding to AA, AB and BB neighbouring pairs. The second atomic shell ranges from distance of at $r \sim 1.5\sigma$ to at $r \sim 2.2\sigma$ and displays the peak-with-shoulder structure typical of hard sphere and metallic glasses[97] .

The static structure factor, shown in Figure 5.4, displays no sharp peaks which may indicate crystallization. Thus, the amorphous character of the samples after quenching is confirmed.

The analysis of the PCF and $S(q)$ for all the samples shows similar results, indicating no crystallization in any of the studied systems. It is worth noting that the topology changes induced by the different cooling rates used in this work are too subtle to appear in the pair correlation function. This is shown in

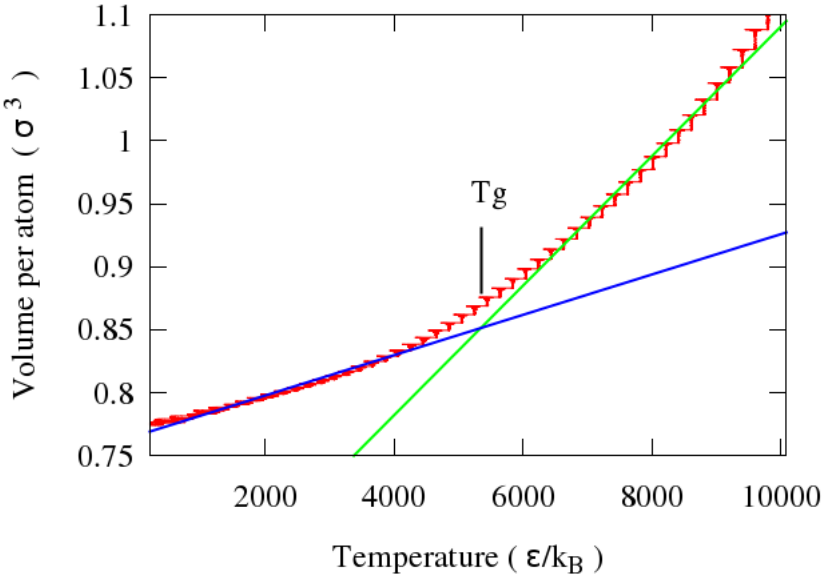

Figure 5.2: Change on the volume per atom during the quench η_2 in a Lennar-Jones binary system of 1098500 atoms.

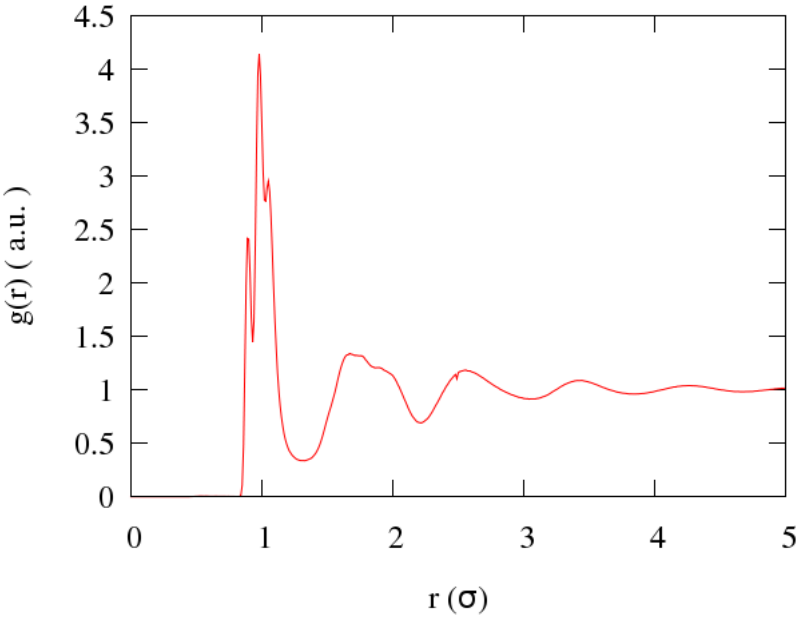

Figure 5.3: Pair Correlation Function of Lennar-Jones binary system of 1098500 atoms and quenching rate η_2.

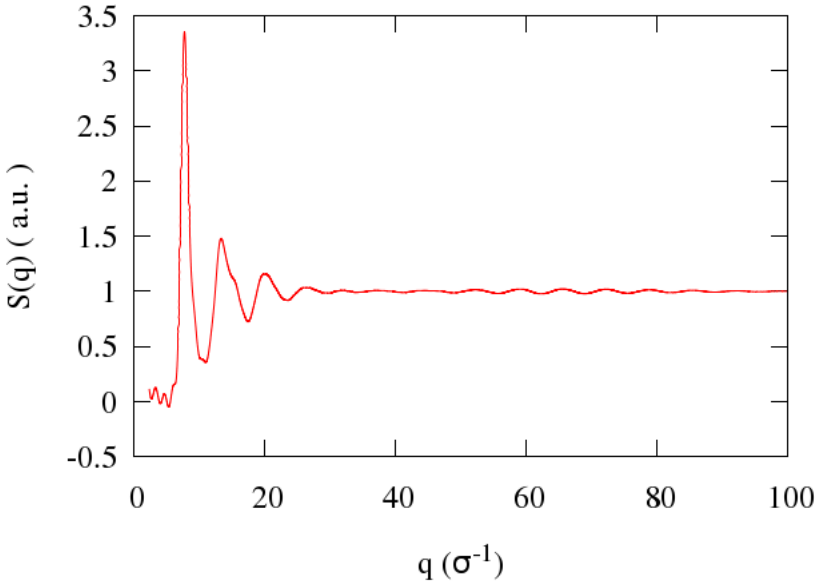

Figure 5.4: Static structure factor of Lennar-Jones binary system of 1098500 atoms and quenching rate η_2.

Table 5.1, were it can be seen that the positions of the main peaks of both the $S(q)$, and the PCF are unafected by either the quenching rate or the size of the simulation box. Furthermore, the box size is large enough, even in the smaller systems, to not introduce any unexpected periodicity.

Finally, the xMakemol software [98] was used in order to confirm again the amorphous structure of the samples. An example is shown in Figure 5.5. In every case, amorphous structures are obtained with a disordered structure and homogeneous distribution of the two atomic species.

5.1.4 Vibrational Density of States

The analysis starts with the vibrational density of states (VDOS). The VDOS is calculated by computing the Fourier transform of the velocity auto-correlation function as indicated in Section 4.3.

The VDOS computations were performed in all cases at a temperature of $1 \cdot k_B[\varepsilon/k_B]$ on well equilibrated systems and for times long enough to obtain a good frequency resolution. In Figure 5.6, the VACF for the system of 1098500 atoms and quenching rate η_2 is represented and from this the VDOS is calculated, see Figure 5.7.

The Debye frequency of the system is defined as:

$$\omega_D = \left(\frac{6\pi^2 N}{V}\right)^{1/3} \langle c \rangle \tag{5.2}$$

where V is the volume of the simulated system and $<$ c $>$ is the averaged sound velocity, calculated as:

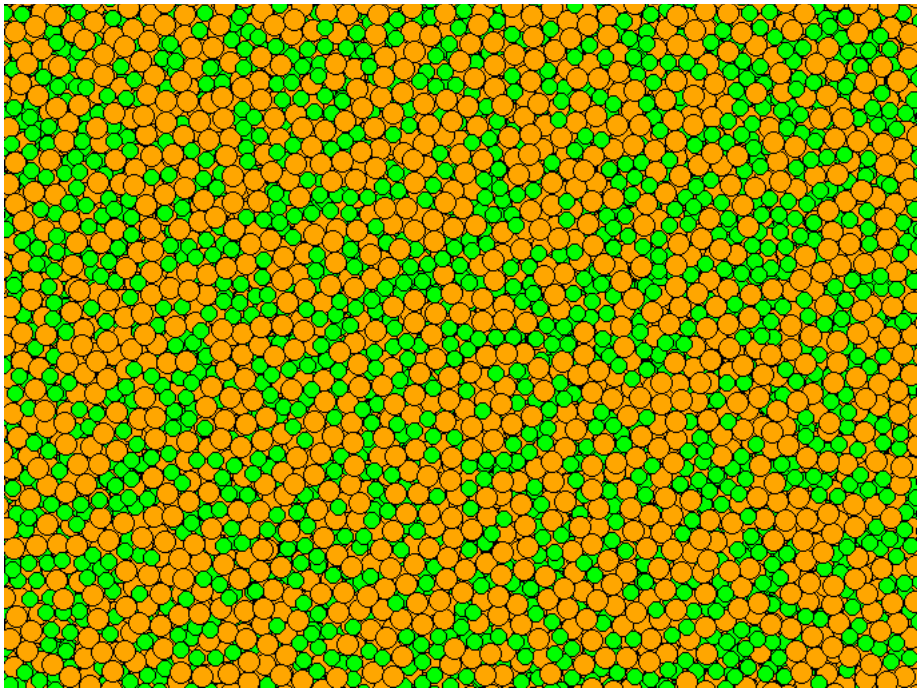

Figure 5.5: Atomic structure of a LJ system at 1K showing 80% of A atoms (orange) and 20% of B atoms (green). The disordered structure of the system and the density fluctuations are revealed.

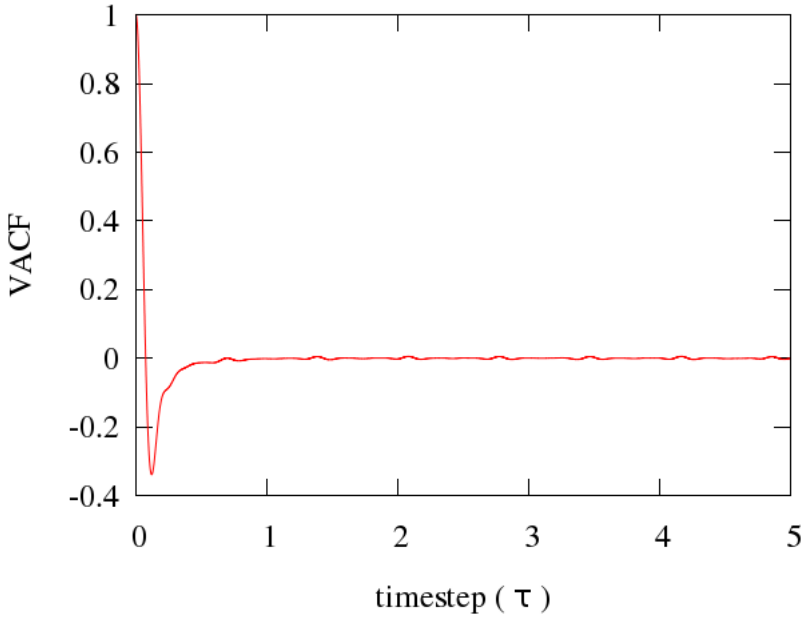

Figure 5.6: Velocity Autocorrelation Function of Lennard-Jones binary system of 1098500 atoms at the equilibrium and quenching rate η_2.

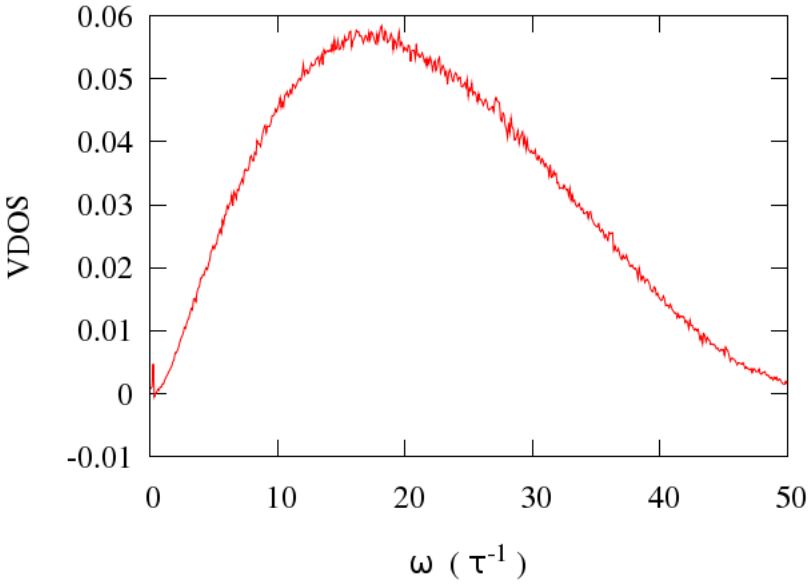

Figure 5.7: Vibrational Density of States calculated from the velocity autocorrelation function in a Lennar-Jones binary system of 1098500 atoms at the equilibrium and quenching rate η_2.

$$\langle c \rangle^3 = \frac{3}{\frac{1}{c_L^3} + \frac{2}{c_T^3}} \tag{5.3}$$

where c_L and c_T are longitudinal and transverse macroscopic sound velocities of sound respectively, assuming constant macroscopic values for the propagation velocities.

The Debye level defined as $9/\omega_D^3$ has a value of $7.99 \times 10^{-4}\tau^3$ in this system.

The Boson peak (BP) designates an excess over the Debye level in the vibrational density of states at low frequencies. Figure 5.8, shows the excess of vibrational states over the Debye level corresponding to the Boson peak. In this case, the peak position appears at $\omega_{BP} = 1.66\tau^{-1}$.

The study of the Debye level and the Boson peak was performed for all the samples, in table 5.1 the values of the macroscopic sound velocities (c_L, c_T), density (N/V), Debye frequency (ω_D), Boson Peak position (ω_{BP}), Boson Peak maximum intensity (I_{BP}) and the Ioffe-Regel frequencies (ω_{IR}^L,ω_{IR}^T), the peak positions for the pair correlation function ($max_1(PCF)$, $max_2(PCF)$) and the maximum of the static structure factor (q_m) are detailed for all the systems studied.

The increase of sample size leads to more realistic results. The density of the systems does not significantly change with the size of the simulation box. On one hand, by increasing the number of atoms, in most of the times, the Debye level increases slightly, although this is not a general tendency, see Figure 5.9. On the other hand, the Debye level decreases as the quenching rate decreases.

N	c_L $(\sigma\tau^{-1})$	c_T $(\sigma\tau^{-1})$	Density (N/V)	ϖ_{Debye} (τ^{-1})	*Debye level* (τ^3)	ϖ_{BP} (τ^{-1})	ϖ_{IR}^{L} (τ^{-1})	ϖ_{IR}^{T} (τ^{-1})	q_{BP}	PCF max_1	PCF max_2	q_m
$\eta_1 = 24.57/500[\varepsilon/(k_B\tau)]$												
13824	10,07	4,31	1,291	22,600	$7,80 \cdot 10^{-4}$	2,07	3,742	1,055	0,205	1,00	1,73	7,75
110592	9,89	4,25	1,291	22,275	$8,14 \cdot 10^{-4}$	1,65	3,907	0,971	0,166	1,00	1,73	7,75
1098500	9,63	4,14	1,291	21,694	$8,81 \cdot 10^{-4}$	1,61	3,617	0,865	0,160	1,00	1,73	7,75
2048000	9,82	4,03	1,291	21,289	$9,33 \cdot 10^{-4}$	1,35	3,688	0,914	0,139	1,00	1,73	7,75
3764768	9,80	4,01	1,291	21,196	$9,45 \cdot 10^{-4}$	1,234	3,795	0,998	0,126	1,00	1,73	7,75
$\eta_2 = 24.57/5000[\varepsilon/(k_B\tau)]$												
13824	10,202	4,48	1,296	23,338	$7,08 \cdot 10^{-4}$	2,51	3,700	1,124	0,247	1,00	1,73	7,75
110592	10,20	4,29	1,296	22,618	$7,78 \cdot 10^{-4}$	2,03	3,716	0,972	0,201	1,00	1,73	7,75
1098500	10,190	4,25	1,295	22,413	$7,99 \cdot 10^{-4}$	1,66	3,538	0,996	0,163	1,00	1,73	7,75
2048000	10,032	4,16	1,295	21,938	$8,52 \cdot 10^{-4}$	1,22	3,600	0,926	0,123	1,00	1,73	7,75
3764768	10,030	4,13	1,295	21,828	$8,65 \cdot 10^{-4}$	1,68	3,729	0,983	0,166	1,00	1,73	7,75
$\eta_3 = 24.57/50000[\varepsilon/(k_B\tau)]$												
13824	10,120	4,55	1,299	23,700	$6,76 \cdot 10^{-4}$	2,18	3,803	1,102	0,213	1,00	1,73	7,75
110592	10,080	4,31	1,299	22,655	$7,74 \cdot 10^{-4}$	2,32	3,884	1,226	0,230	1,00	1,73	7,75

Table 5.1: Results obtained from simulations using the Lennard-Jones potential.

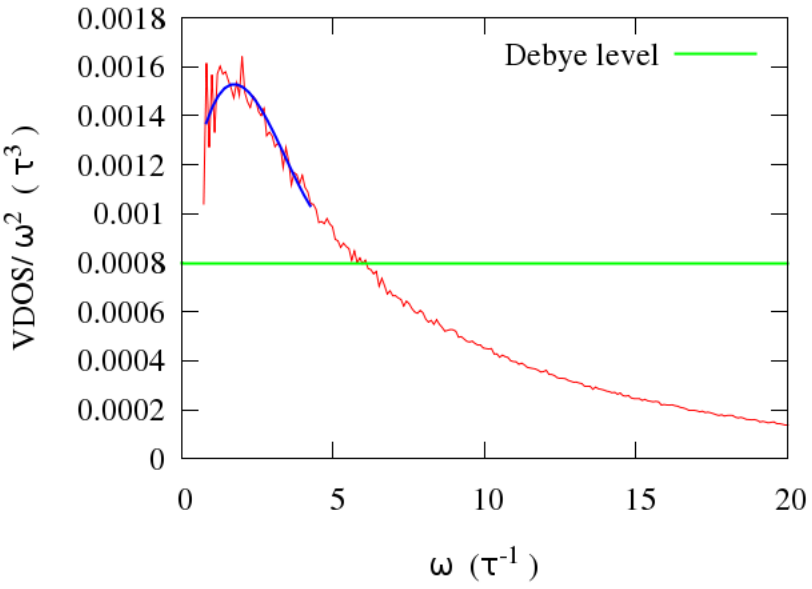

Figure 5.8: Boson Peak observed in of Lennar-Jones binary system of 1098500 atoms at the equilibrium and quenching rate η_2 .

When the quenching rate is decreased more relaxed systems are obtained, with less free volume and higher elastic constants. This increase on the density and the sound velocities of the glass affects the value of ω_D, obtaining higher values and consequently smaller values for the Debye level.

The position of the Boson peak is affected by the size effects. The increase of the number of atoms and the corresponding number of vibrational states permits a better study of the low frequency region. Figure 5.10, shows how the Boson peak intensity is higher when applying fast quenching rates and their position shifts slightly to smaller frequencies. More relaxed systems with higher density affect the elastic constants of the system that increase as the quenching rate decreases. A higher BP intensity for less relaxed glasses is expected and it is a well-known phenomenon. In metallic glasses the increase of BP intensity has been found to be correlated with the decrease of shear modulus [99] in the less dense (more defective) structures of the as-quenched materials.

The quenching rates applied in MD simulations are far higher than the ones applied in any real system. However, the change in the BP intensity shown in figure 5.10 proves that the different quenching rates used in this work can produce glass structures with significant differences in the vibrational properties, and similar to the ones experimentally observed between relaxed and as-quenched metallic glasses. More relaxed systems with higher density, obtained with decreasing quenching rates, results in higher elastic constants. These results are in agreement with the ones obtained by Bauchy on the study of densified silicates using MD in small systems [57]. Moreover, similar results were observed experimentally in different systems as pure silica [58], lithium silicate glass , $Na_2FeSi_3O_8$ glass [60], as well as in different polymers [61].

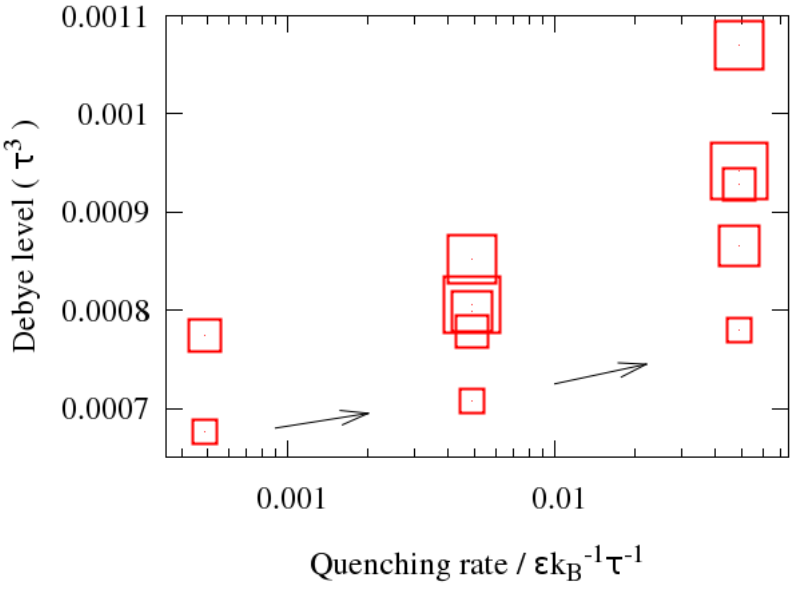

Figure 5.9: Debye level versus quenching rate determined in simulation boxes of different sizes. The size of the box, namely $1 \cdot 10^4$, $1 \cdot 10^5$, $1 \cdot 10^6$, $2 \cdot 10^6$ and $3 \cdot 10^6$ atoms, is indicated by the size of the corresponding symbol.

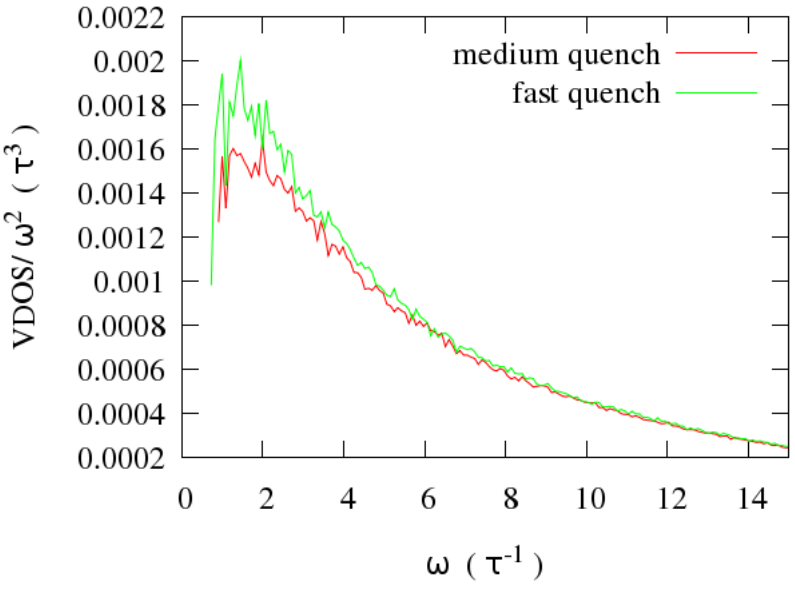

Figure 5.10: Effect of the quench rate on the Boson peak position and intensity in a Lennard-Jones binary system of 1098500 atoms with fast (η_1) and medium (η_2) quenching rate .

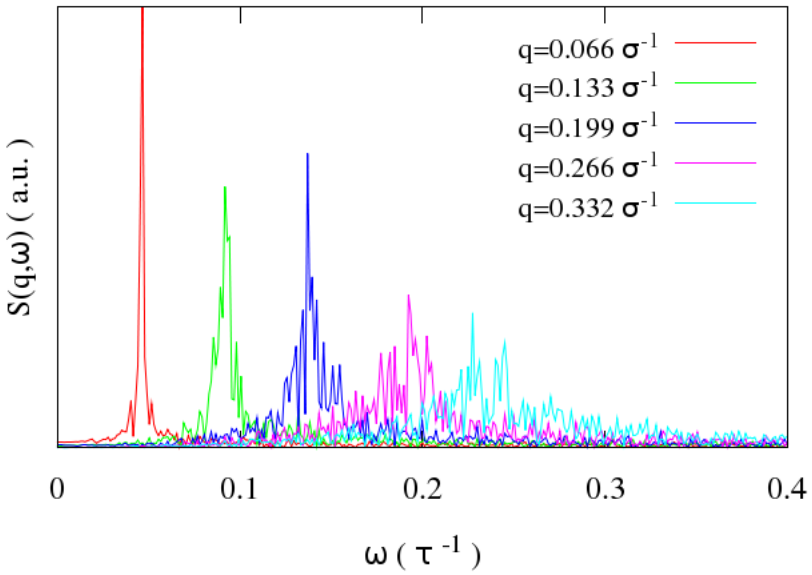

Figure 5.11: Longitudinal dynamic structure factor for 5 different q wave vectors in a Lennard-Jones system of 1098500 atoms and quenching rate η_2.

5.1.5 Dynamic Structure Factor (S(q,w))

The behavior of acoustic excitations in glasses is studied by means of the dynamic structure factor, $S(q,\omega)$. For that reason, the dependence of the longitudinal and transverse dynamics structure factor, $S_L(q,\omega)$ and $S_T(q,\omega)$ according to the wavevector (q) has been calculated as indicated in Section 4.3.

Figure 5.11 displays the longitudinal dynamic structure factor, computed for different wave vectors. The wave vectors considered, are defined as $q_i = 2\pi k_i/L$, where L is the box length and $k_i = 1, 2, ..., n$. Below $q_1 = 2\pi/L$ the physics of the system is altered by the periodic boundary conditions of the simulations, which would reproduce a crystalline-like phonon band structure with a first Brillouin zone border at π/L [56]. The vibrational modes below q_1 are affected by such artifact and this implies that the access to lower q values is limited by the box size.

As shown in the figure, the width of the peak in $S(q,\omega)$ increases and the characteristic frequency is shifted to higher frequencies as the wave-vector increases. In order to extract information on the peak position and width, the calculated $S(q,\omega)$ will be fitted by a Damped Harmonic Oscillator (DHO) model:

$$S_{L,T}(q,\omega) \propto \frac{\Omega_{L,T}(q)^2 \Gamma_{L,T}(q)}{(\omega^2 - \Omega_{L,T}(q)^2)^2 + \omega^2 \Gamma_{L,T}(q)^2} \tag{5.4}$$

where $\Omega_{L,T}(q)$ and $\Gamma_{L,T}(q)$ are the peak frequency and the full width at half maximum respectively, and L and T stand for the longitudinal and transverse acoustic modes. In this case, the fitting is performed by using a Levenberg-

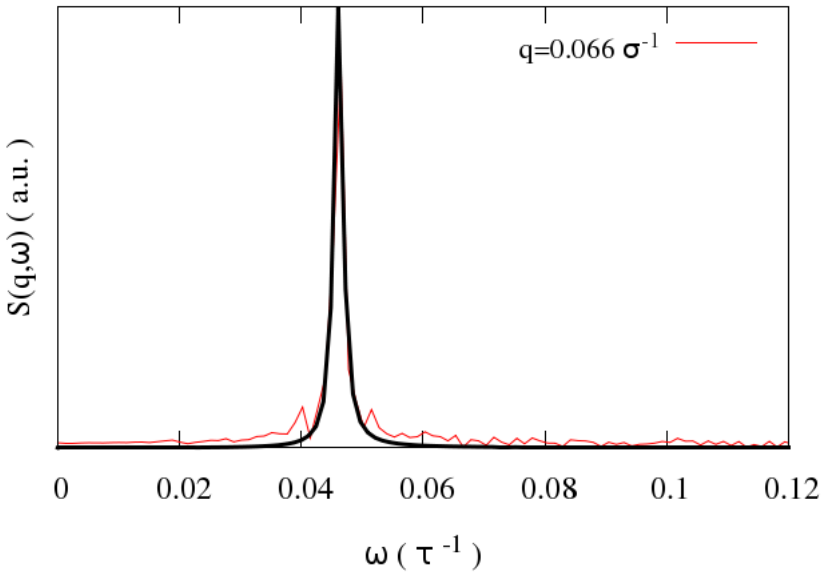

Figure 5.12: Fit for the longitudinal dynamic structure factor for a wave-vector $q = 0.066\sigma^{-1}$ in a Lennard-Jones system of 1098500 atoms and quenching rate η_2.

Marquard algorithm with a tolerance of $1 \cdot 10^{-8}$. Figure 5.12 shows an example of the fitting. The DHO model used for $S(q,\omega)$ is a valid approximation in the low-frequency region [100], and it is commonly used to model the experimental INS and IXS results in metallic liquids and glasses [46, 50].

The fitted values of $\Omega_{L,T}(q)$ allow us to build the dispersion relation of the material. Acoustic excitations in glasses show dispersion curves $\Omega_{L,T}(q)$ similar to that of the crystalline acoustic modes with an almost linear region at low q numbers and a bending when approaching the limit of the first pseudo-Brillouin zone $q_m/2$, where q_m is the position of the maximum of the static structure factor $S(q)$.

The broadening of the excitation $\Gamma_{L,T}(q)$ describes the attenuation of the acoustic propagation modes. The Ioffe-Regel (IR) limit condition is given by:

$$\Omega(q) = \pi\Gamma(q) \tag{5.5}$$

Above the IR limit, the mean path-length is smaller than the wave-length of the acoustic excitations and, therefore, the propagating nature of the vibrational modes is suppressed. Figure 5.13, shows an example of the dispersion relations $\Omega(q)$ of the longitudinal and transverse phonons obtained in the simulations. For low q wave vectors they display a linear behavior. Because the access to low q values and the data in this region is limited by the box size, an improved and more detailed description of the low-q region requires multimillion atom systems.

In the case shown in the figure, the Iofffe-Regel limit for the longitudinal wave, ω_{IR}^{L}, is determined as $3.538\tau^{-1}$and for the transverse wave, $\omega_{IR}^{T} =$

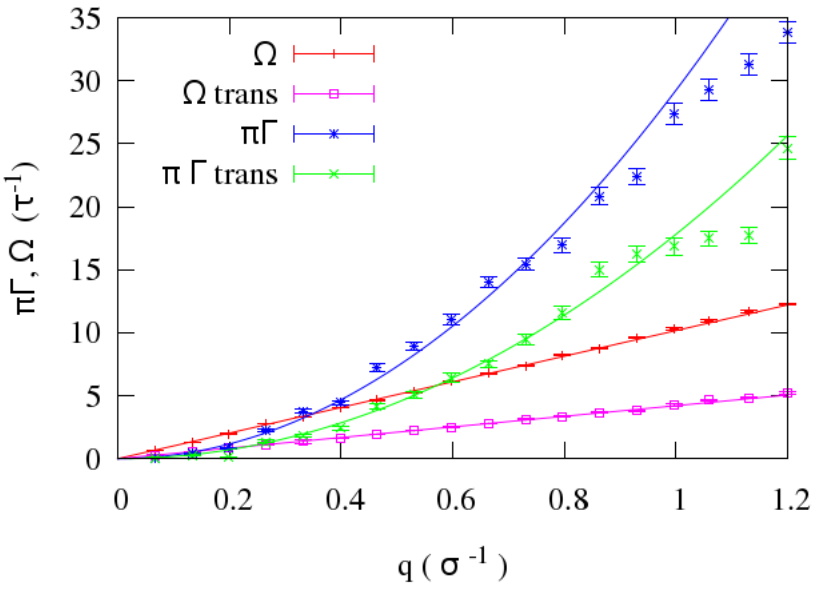

Figure 5.13: Dispersion curve $\Omega_{L,T}(q)$ and broadening $\pi\Gamma_{L,T}(q)$ obtained from $S_{L,T}(q,\omega)$ in a Lennard-Jones system of 1098500 atoms and quenching rate η_2.

$0.996\tau^{-1}$. The ω_{IR}^{L} is found at frequencies higher than the Boson peak frequency (ω_{BP}) see Figure 5.14 ($\omega_{IR}^{L} > \omega_{BP}$).

The corresponding dispersion relationships and Boson peak frequencies are calculated for the different size systems and applying different quenching rates. Slow quenching rates applied to large boxes imply a high computational cost; for this reason the slow quench is performed only in smaller systems. The study performed in different size systems and different quenching rates shows that in all cases $\omega_{IR}^{L} > \omega_{BP}$; contrarily, ω_{IR}^{T} has values lower but close to that of ω_{BP}.

The relation between the BP and the limiting frequency for the propagating nature of the acoustic modes has been discussed in many works. In ref.[43] the ω_{BP} was found to coincide with the ω_{IR}^{L} in a Li_2O-B_2O_3 glass, and it was suggested that such relation could be extended to many other glassy materials. On the contrary, Scopigno et al. [46] showed that in a $Ni_{33}Zr_{67}$ metallic glass the ω_{IR}^{L} was well above the ω_{BP} and, therefore, the propagating nature of the longitudinal acoustic excitation was extended to frequencies above BP. In Shintani et al. [44], by means of 2D and 3D simulations of systems with very different potentials and fragility parameters, they showed that the ω_{BP} was systematically related with the transverse ω_{IR}^{T}. One of the systems studied in ref. [44] was a 3D Lennard-Jones glass with $N = 6000$ and concentration $A_{33}B_{67}$ where A and B are the big and small atoms respectively. The system was chosen for approximating the $Ni_{33}Zr_{67}$ metallic glass studied experimentally by IXS.

The results presented here confirm the same result in a 3D Lennard-Jones system with concentration $A_{80}B_{20}$. This composition is chosen in order to approximate a large family of metallic glasses, including Fe, Pd and Pt-based glasses, that have similar compositions. In ref. [44], it is proposed that the

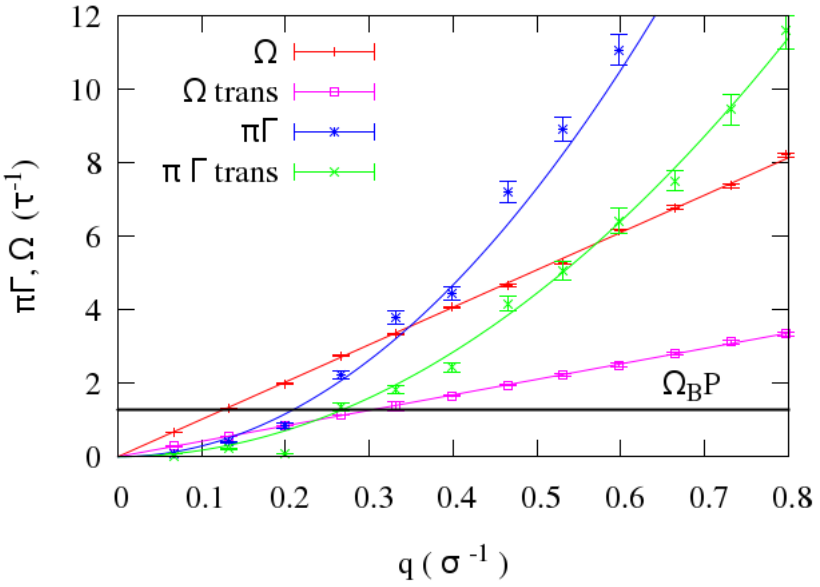

Figure 5.14: Dispersion curve $\Omega_{L,T}(q)$ and broadening $\pi\Gamma_{L,T}(q)$ obtained from $S_{L,T}(q,\omega)$ and frequency of the Boson Peak Lennard-Jones system of 1098500 atoms and quenching rate η_2.

excess modes generating the BP correspond to transverse localized vibrational modes generated by some kind of defective configurations of the glass structure. These localized modes strongly couple with the propagating transverse excitations and govern their damping and dissipation [101], this giving rise to the relation $\omega_{IR}^{T} \simeq \omega_{BP}$. In this picture, the ω_{BP} indicates the frequency at which the transverse excitations in glasses change from propagating to diffusive modes. The extension of the propagating nature of the longitudinal modes above ω_{BP} is interpreted as an indication of the predominantly transverse character of the BP. Indeed, it is widely recognized that the origin of the BP is predominantly related to localized transverse modes and to the fluctuations of shear modulus [102]. However, although ω_{IR}^{L} is above the maximum of the BP ω_{BP}, the IR limit for longitudinal modes is always within the frequency region of the BP.

The results obtained here for the $A_{80}B_{20}$ 3D Lennard-Jones system are also in agreement with the experimental IXS results obtained for the $Pd_{77}Si_{16.5}Cu_{6.5}$ metallic glass shown in ref. [50]. The IXS technique is limited to the measurement of longitudinal excitations. However, from the ratio between shear and bulk modulus of the material, it seems plausible that the same overall picture with $\omega_{IR}^{T} \simeq \omega_{BP}$ and $\omega_{IR}^{L} > \omega_{BP}$ will hold in $Pd_{77}Si_{16.5}Cu_{6.5}$ glass.

The analysis of the dynamic structure factor gives information on the length-scales governing the microscopic dynamics of the system. For the system shown in Figure 5.14, the q-value for the Boson peak, q_{BP} is found at $0.16\sigma^{-1}$. Here q_{BP} is defined as the intersection between the ω_{BP} and the longitudinal dispersion curve. This value, calculated for all systems shows small changes by increasing the size of the system and modifying the quenching rate. Figure

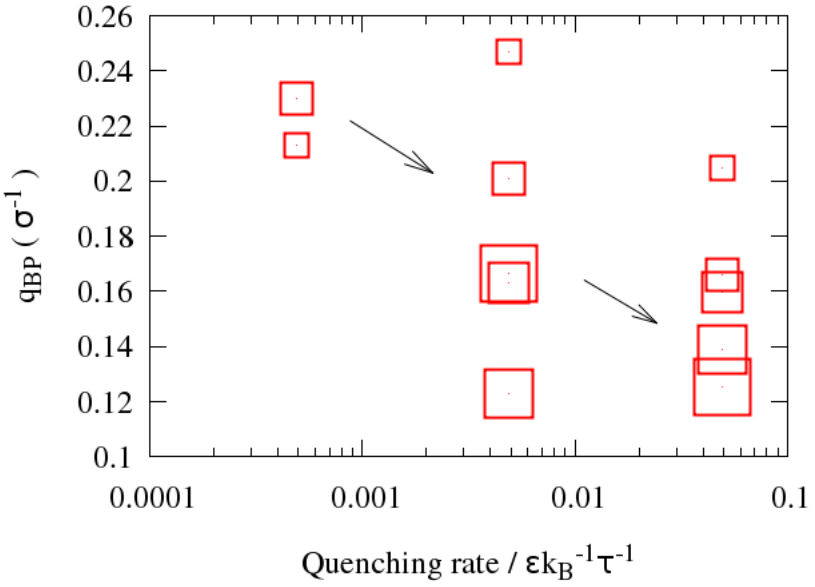

Figure 5.15: q_{BP} versus quenching rate determined in simulation boxes of different sizes. The size of the box, namely $1 \cdot 10^4$, $1 \cdot 10^5$, $1 \cdot 10^6$, $2 \cdot 10^6$ and $3 \cdot 10^6$ atoms, is indicated by the size of the corresponding symbol.

5.15 presents the q_{BP} obtained for different size systems and applying different quenching rates, showing that q_{BP} increases as the quenching rate decreases. Figure 5.10 shows that decreasing the quenching rate the position of the BP shifts to higher frequencies. Furthermore, the slope of the dispersion curve is also reduced for higher quenching rates. Both effects contribute to the increase of the q_{BP} in more relaxed systems (lower quenching rates). The influence of the box size is also observed in figure 5.15, q_{BP} increases when studying smaller systems.

The q-values corresponding to the Ioffe-Regel (IR) limits of the longitudinal and transverse polarizations, q_{IR}, are shown in Figure 5.16. The values computed in small systems, up to 10^6atoms, present a higher dispersion than those obtained from larger systems. As already discussed before, the periodic boundary conditions restrict the number of allowed wave-vectors in small boxes, larger boxes allow us to access lower q-values allowing better determination of the Ioffe-Regel limit. For this reason, the IR limit cannot be determined precisely in small systems and we will concentrate our analysis on the behavior observed in large systems. Unfortunately, due to the computational cost of applying slow quenching to large systems, only fast quenching rates are compared in large boxes.

For the system with $N = 1098500$ (shown in figure 5.14) the values are found $q_{IR}^L = 0.34\sigma^{-1}$ and $q_{IR}^T = 0.236\sigma^{-1}$. When considering different quenching rates in large systems, the q_{IR} values decrease as the quench rate is decreased, both for longitudinal and transverse vibrations. This reduction indicates that the coherence length increases in more relaxed systems, as expected. As per the

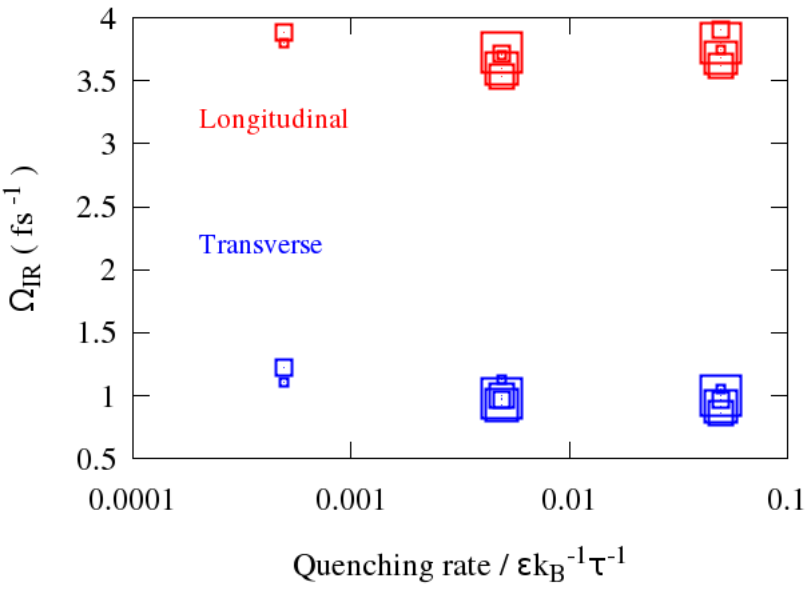

Figure 5.16: Ioffe-Regel limit frequency versus quenching rate for longitudinal and transverse phonons, determined in simulation boxes of different sizes. The size of the box, namely$1 \cdot 10^4$, $1 \cdot 10^5$, $1 \cdot 10^6$, $2 \cdot 10^6$ and $3 \cdot 10^6$ atoms, is indicated by the size of the corresponding symbol.

dependence of the Ioffe-Regel limit on the size of the box, for the three larger systems there is a consistent tendency to increase the value q_{IR} when the size of the box is increased, but the tendency is far less clear than the one observed for q_{BP}. From these results it is not clear if there is a dependency of the q_{IR} on the size of the box.

The elastic medium of glasses and liquids is characterized by the presence of heterogeneities at the nm-length scale. The connection between the macroscopic homogeneous continuum and the atomic-scale short range order (SRO) generates structural and elastic fluctuations with correlation lengths of the order of tenths atomic sizes. The intensity of the fluctuations slightly decreases when cooling down the liquid above T_g. Below the glass transition, the fluctuations are frozen in the glassy structure and their intensity is expected to diminish when increasing the degree of relaxation of the system [103]. As for the average correlation length of such fluctuations, it is expected to increase as the liquid is cooled down towards the glass transition [104] or the glassy state is more deeply relaxed. In LJ simulations, the correlation length in the supercooled liquid regime (above Tg) is found of the order of few atomic sizes [104]. Below Tg, the correlation lengths of the frozen structure are found to be much larger. In ref. [8], the mean correlation length of elastic fluctuations was found to be $\xi \simeq 23\sigma$ in a LJ simulation of a system with a poly disperse distribution of atomic sizes.

In this work, for the case of $N = 1098500$ and quenching rate η_2, the wave-lengths $\xi = \frac{2\pi}{q}$ of the phonons corresponding to the q_{BP}, q_{IR}^L and q_{IR}^T values are found $\xi_{BP} = 52\sigma$ (24σ if calculated using the transverse dispersion curve), $\xi_{IR}^L = 18\sigma$ and $\xi_{IR}^T \simeq 26\sigma$. As discussed before, all these correlation lengths are increased when reducing the quenching rate. Therefore, the BP position and the IR limit coincide well with the expected behavior if they were related to the elastic heterogeneities and the break-down of the continuous elastic medium.

The size of the boxes L of the LJ simulations of this work goes from $L \simeq 10\sigma$ to $L \simeq 175\sigma$. The study of the effects of heterogeneities with sizes around 20 atomic sizes on the microscopic dynamics is then utterly affected in the smaller systems. The existence of correlation lengths $\xi > L$ is suppressed by the periodic boundary conditions, thus changing artificially the distribution of correlation lengths that would be present in an ideal system with infinite length. It is then expected that all the quantities associated with the presence of mesoscopic inhomogeneity are affected by the size of the system. This effect is clearly seen in the change of q_{BP} as function of L in figure 5.15. The difference between the two largest systems indicates that, even for systems much more larger than the wave-length of the studied acoustic excitations, the size of the box is still influencing the distribution of elastic heterogeneities of the system.

Some extra information can be obtained from the q-dependence of the apparent sound phase velocity $c_{L,T}(q)$ and the sound attenuation $\Gamma_{L;T}(q)$. The apparent sound velocity is calculated as:

$$c_{L,T=}\frac{\Omega_{L,T}(q)}{q} \tag{5.6}$$

In Figure 5.17, the apparent sound phase velocity is represented for the transverse and longitudinal cases presenting values around $4.2\sigma\tau^{-1}$ and $10\sigma\tau^{-1}$ respectively. For all the systems studied, the macroscopic longitudinal sound

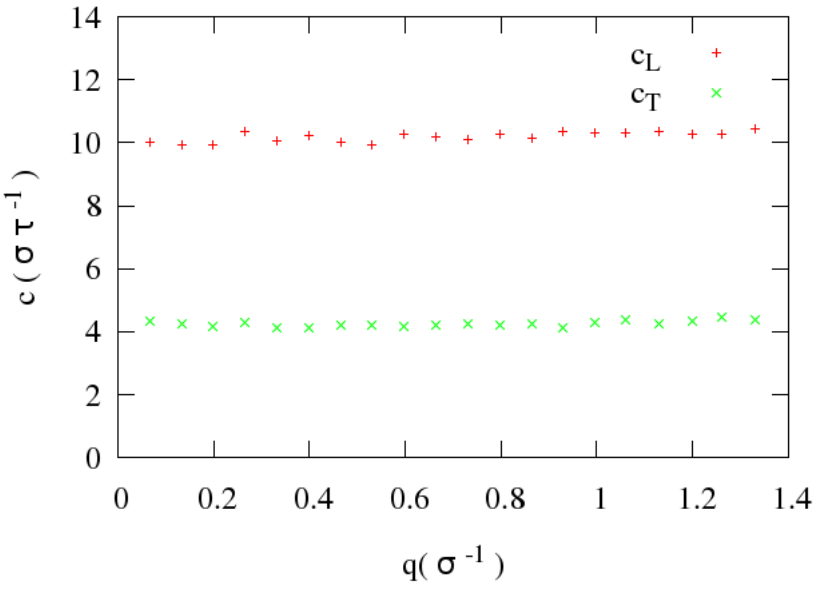

Figure 5.17: Apparent longitudinal and transverse phase velocity as a function of moment transfer q in a Lennard-Jones system of 1098500 atoms and quenching rate η_2.

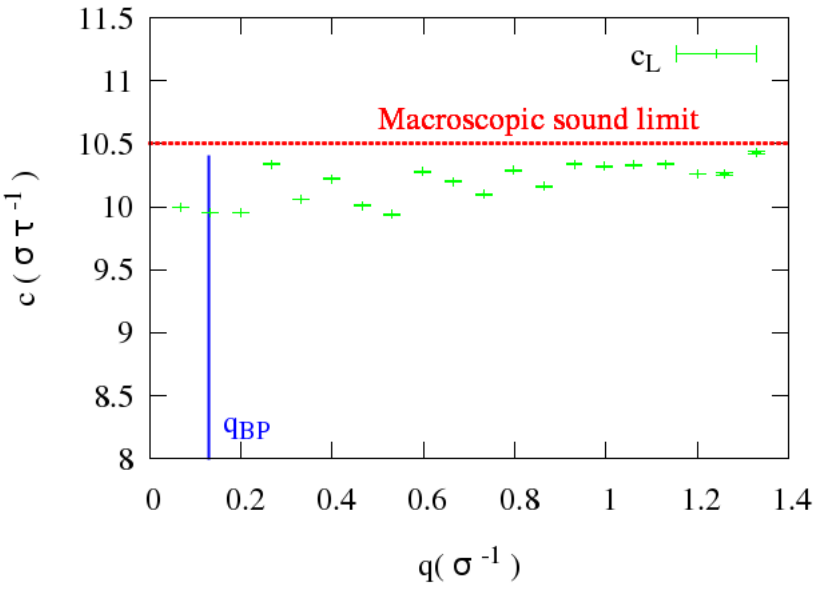

Figure 5.18: Apparent longitudinal phase velocity as a function of moment transfer q, q_{BP} and Macroscopic sound limit in a Lennard-Jones system of 1098500 atoms and quenching rate η_2.

limit has a value around $10.5\sigma\tau^{-1}$with small differences due to the different quenching rates and box sizes. The values obtained in the $A_{80}B_{20}$ Lennard-Jones systems of this work are similar to the ones obtained in the study of a monoatomic Lennard-Jones systems[88]. Different quenching rate leads to diverse glassy states with different overall properties such as the sound velocity. By decreasing the quenching rate the sound speed increases slightly. This is coherent with the reduction of the free volume and the increase in the rigidity of the material.

For low q values the determined sound speeds are almost independent of the box size, while for larger values small boxes give systematically larger values than larger boxes. Thus, we consider that the analysis has to be focused in the results obtained for larger boxes.

At small q it is observed a softening of the apparent sound velocity, see Figure 5.18. In previous references [88] the softening region in a monoatomic Lennard-Jones glass was obtained at $q < 0.27\sigma^{-1}$ and it was showed that this regime is accompanied by strong scattering with $\Gamma(q) \propto q^4$. It was proposed [88, 7] that this softening is originated by a Rayleigh-like scattering of sound waves by the elastic fluctuations in the media. This reduction of the apparent sound velocity was already observed in experimental results and also in monoatomic LJ glasses [88, 50]. In our case, the acoustic waves with wave vectors smaller than $0.1\sigma^{-1}$ show a 6% reduction of the apparent sound velocity.

Figure 5.19 shows the q-dependence of the longitudinal damping. Although the softening of the $c_L(q)$ is detected at the lowest q values, the size of the simulation boxes does not allow us to investigate the q^4 regime predicted by the model up to the BP zone as there are just two points in this region. On increasing the wave-vector q, there is a transition region characterized by a plateau on the $c_L\,(q)$ values and in concordance with the change to a quadratic $\Gamma(q) \propto q^2$ dependence (see Figures 5.18 and 5.19); this region is extended until $q \sim 0.8{-}1\sigma^{-1}$. Above this region the $\Gamma(q)$ shows a change in the slope towards a linear q-dependence that is consistent with experimental observations in metallic liquids and glasses [50, 46].

Finally, moving to higher frequencies, at q values approaching the pseudo-Brillouin zone limit, the dispersion curve exhibits a bending on a very broad shape. The bending expected at the limit of the first pseudo-Brillouin zone should be observed as maximum of the dispersion curve $\Omega(q)$ at $q_m/2$, where q_m is the position of the maximum of the $S\,(q)$. [105] These q values are only achieved in small systems due to the wavevector range studied, see Figure 5.20.

For all the systems studied previously the behavior of the sound velocity is studied. In all the systems studied, the macroscopic longitudinal sound limit has a value around $10.5\sigma\tau^{-1}$with small differences due to the different quenching rates and the box sizes. The values obtained in this simulations are in agreement with the ones obtained in the study of a monoatomic Lennard-Jones systems[88]. Although these values are higher than the ones obtained in experiments, the systems keep identical behavior. [50]

Different quenching rates lead to diverse glassy states with different overall properties such as the sound velocity. By decreasing the quenching rate the sound speed increases slightly. This is coherent with the reduction of the free volume and the increase in the rigidity of the material.

Moreover, an increase on the simulation box shows in all cases a reduction

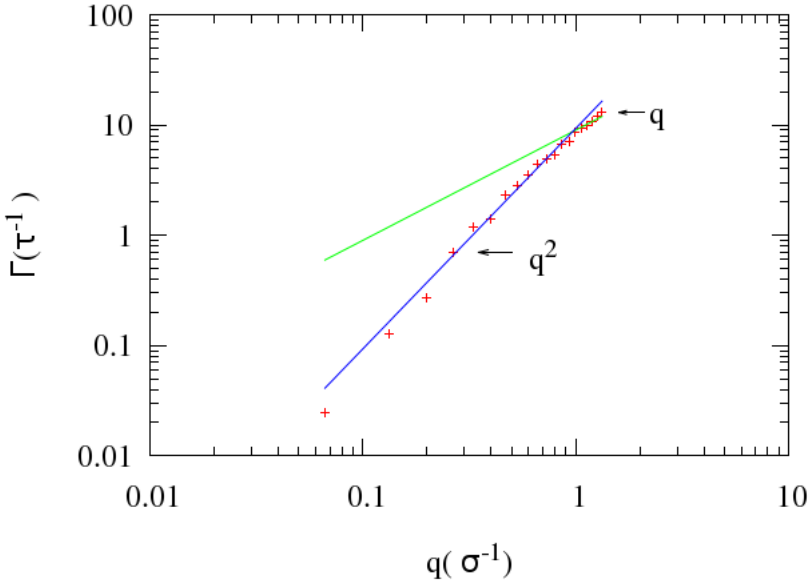

Figure 5.19: q-dependence of the acoustic excitations for the longitudinal in a Lennard-Jones system of 1098500 atoms and quenching rate η_2.

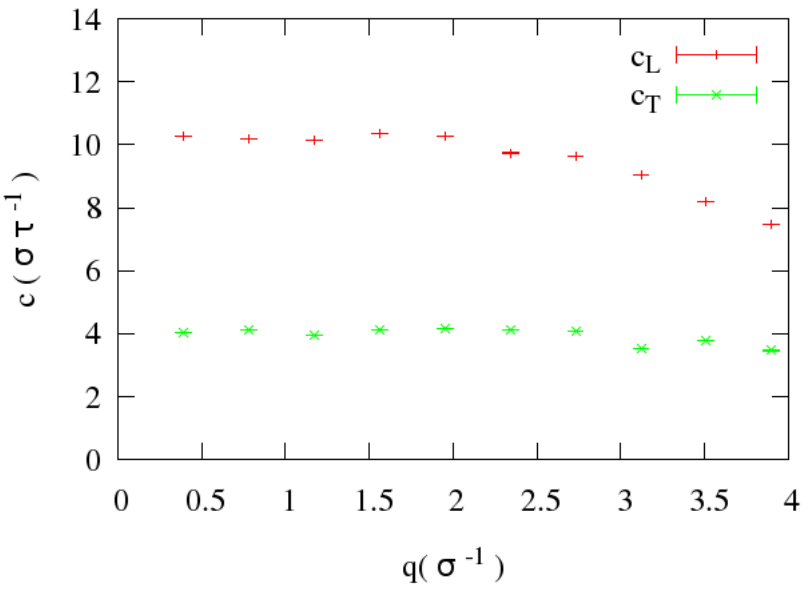

Figure 5.20: Apparent longitudinal and transverse phase velocity as a function of moment transfer q in a Lennard-Jones system of 5324at atoms and quenching rate η_2. The boundary of the pseudo-Brillouin zone is found at $\frac{q_m}{2} \sim 3,87\sigma^{-1}$.

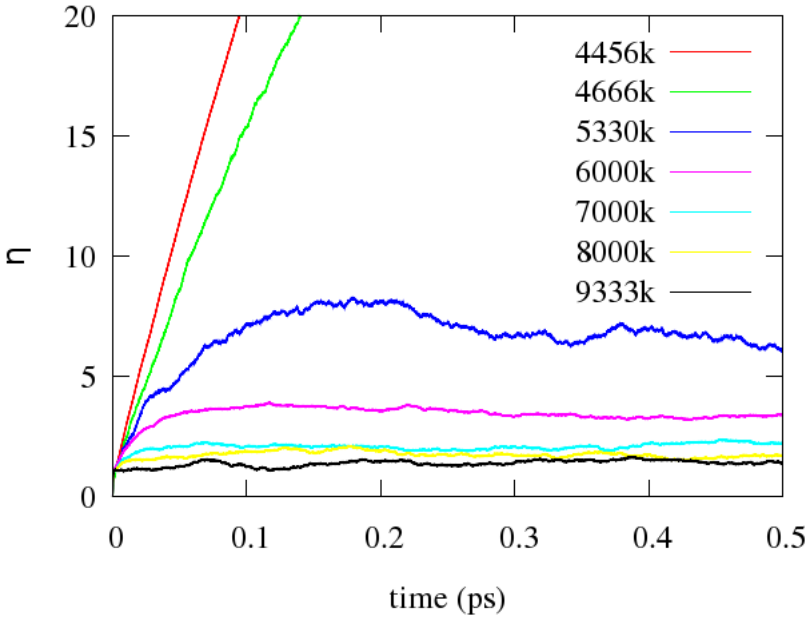

Figure 5.21: Stress autocorrelation function for a binary Lennard-Jones system of 55296 atoms and quenching rate η_2.

on the sound speed.

5.1.6 Viscosity

The shear viscosity is calculated by integration of the stress auto-correlation function.

$$\eta = \frac{V}{k_B T} \int < \sum P_{\alpha\beta}(t) \cdot P_{\alpha\beta}(0) > dt \tag{5.7}$$

Starting from an equilibrated configuration of 55296 atoms, the stress auto-correlation function is calculated at different temperatures. The auto-correlations of the three off-diagonal elements were computed until convergence and averaged, and from that the corresponding shear viscosity was computed. The choice of the optimal system size of 55296 was performed by analyzing the influence of the box size on the results and the computational cost.

The viscosity was calculated for a range of temperatures The stress auto-correlation is computed for a range of temperatures between 10000 and T_g, see Figure 5.21. From this and by using Equation 5.7, the viscosity at each temperature is calculated.

A common way to display the temperature dependence of the viscosity in supercooled liquids is the so called Angell plot, in which $\log(\eta)$ is plotted against T_g/T. This is done for several temperatures in the range between 10000k and T_g, see Figure 5.22

To reduce the stochastic noise, the pressure autocorrelation was fitted in each case to a linear combination of two exponential functions:

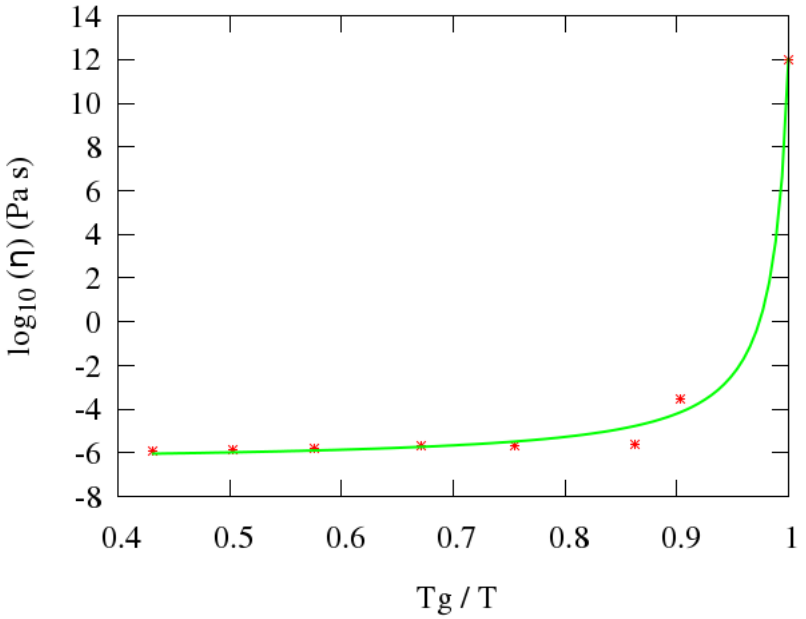

Figure 5.22: Angell plot for a binary Lennard-Jones system of 55296 atoms and quenching rate η_2.

$$a_1 \exp(-\omega_1 \cdot x) + a_2 \exp(-\omega_2 \cdot x) \tag{5.8}$$

which allowed us to obtain a consistent estimation of the viscosity.

The Vogel Fulcher Tammann equation describes the temperature dependence of viscosity:

$$\eta = \eta_0 \exp(A/T - T_0) \tag{5.9}$$

where η_0, A and T_0 are constants.

This function fits the values obtained for the viscosity at different temperatures.

$$log(\eta) = log(\eta_0) + \frac{A}{T - T_0} \cdot \frac{1}{ln(10)} \tag{5.10}$$

Consequently, by fitting the values for the temperatures calculated, the values for η_0, A and T_0 can be obtained.

The fragility, m, is defined by the slop of Angell plot at $T_g/T = 1$.

$$m = \frac{\partial log_{10}\eta}{\partial(T/T)_{T=T_g}} = \frac{B \cdot T_g}{(T_g - T_0)^2 \cdot ln(10)} \tag{5.11}$$

By convention, the glass transition, T_g, is where the viscosity reaches a value of 10^{12}Pa·s and then when the temperature tends to 0 reaches a value of 10^{-2}Pa·s. With this definition, an ideal strong glass would have a fragility $m \approx 17$, while higher values indicate higher fragility. [106, 107, 108, 109].

These values have been used to refine the value of T_g and accordingly the value of the fragility

$$T_g = T_0 + \frac{B}{17 \cdot ln(10)} \tag{5.12}$$

The values of T_g and B were computed iteratively, until convergence was reached. In this case, the system studied gives a fragility $m = 1316$ this result is in agreement with results indicating that Lennard-Jones systems are highly fragile systems [110]. Moreover, the fitted value for T_g resulted to be $4027K$, in concordance with that obtained monitoring the volume change during the quench.

5.2 Morse systems

The Morse potential is similar to the Lennard-Jones potential but is a more "bonding-type" potential, suitable for cases when attractive interaction comes from the formation of a chemical bond. The Morse potential is adequate to analyze the behaviour of atoms in the metallic state, where the bond is non-directional. In this sense, it is expected that its results be more realistic and closer to those obtained with more sophisticated potentials such as the Embedded atom method potential.

The Morse potential is defined as

$$V_M(r) = D\left[e^{-2a(r-r_e)} - 2e^{-a(r-r_e)}\right]$$

where D is the depth of the potential well, a defines the width of the potential and r_e is the equilibrium bond distance. The values of D, a and $r_e$are chosen to describe the interatomic potential of the desired species. In particular, the width of the potential is related with the interatomic force (and thus the elastic constants of the material), as $a = \sqrt{\frac{k_e}{2D}}$, $k_e$being the force constant at the energy minimum. Figure 5.23 shows the shape of both potentials with the same bonding energies and almost the same repulsive component. It can be appreciated that the tail of the Morse potential is shorter than that of the Lennard-Jones.

There are several reasons to analyze the behaviour of systems with the Morse potential. Firstly, the longer tail of the Lennard-Jones potential may induce an artificial long range order without much physical sense. With the LJ potential an atom may feel the potential of the second neighbour when this is not in a perfect row with its first neighbour. This is quite unphysical inside a metallic material, where the valence electronic clouds are mostly spherical, and induces a "second-neighbour" ordering. For this reason it can be expected that LJ glasses be more fragile than Morse glasses. Secondly, the numerical parameters of the LJ potential have no relation with the actual parameters of a real glass, and so the results obtained with the LJ potential can be compared only qualitatively to the experimental results. Finally, the anharmonic component of the Morse potential is different from that of the LJ potential, allowing us to check the influence of anharmonicity on the properties of the material and, in particular, in its fragility. It may be argued that the Embedded Atom Method potential is even more realistic than the Morse potential, but, on the one hand, it is computationally more costly and, in the other hand, it is not possible to define

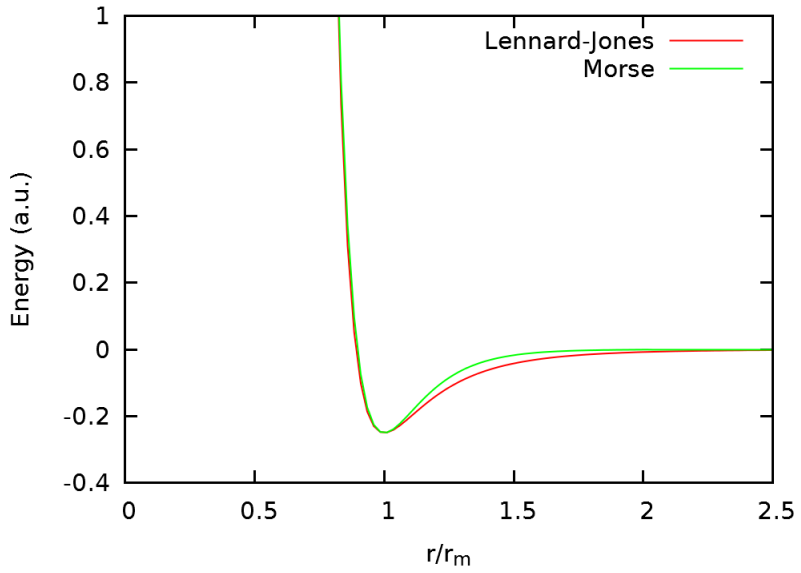

Figure 5.23: Comparison between Lennard-Jones and Morse potential. The parameters of the Morse potential were chosen to have the same bonding energy and almost the same repulsive component. To help comparison, interatomic distances are normalized by the position of the potential minimum r_m.

Table 5.2: Parameters of the Morse potential

	mass/AMU	D/eV	r_e/Å	a
Cu	63.546	0.2414	2.5562	1.4342
Pd	106.42	0.1713	2.7506	1.6464
Cu-Pd		0.2031	2.6589	1.5401

its anharmonicity in a clear way, as it considers the effect of the neighbourhood electronic density as a many-body interaction. Thus, the Morse potential allows us to use an analytical, computationally fast potential with realistic parameters and known anharmonicity.

The studied system is a binary system $Cu_{20}Pd_{80}$. To help comparison, most of the configurations simulated with the Morse potential coincide with those simulated with the EAM potential, presented in the next Section.

The parameters of the potential were taken from [66, 69, 70, 71] and are given in Table 5.2. These parameters were determined for the pure metals. In order to obtain the interspecies potentials we followed the prescription from [70]

$$\left(\frac{D_{12}\alpha_{12}\exp(2\alpha_{12})}{4r_{e12}}\right)^{r_{e12}/\alpha_{12}} = \left(\frac{D_{11}\alpha_{11}\exp(2\alpha_{11})}{4r_{e11}}\right)^{r_{e11}/2\alpha_{11}} \left(\frac{D_{22}\alpha_{22}\exp(2\alpha_{22})}{4r_{e22}}\right)^{r_{e22}/\alpha_{22}} \tag{5.13}$$

$$\frac{r_{e12}}{\alpha_{12}} = \frac{1}{2}\left(\frac{r_{e11}}{\alpha_{11}} + \frac{r_{e22}}{\alpha_{22}}\right) \tag{5.14}$$

$$\frac{D_{12}}{4}\exp(r_{e12}\left(\frac{\alpha_{11}}{2r_{e11}}+\frac{\alpha_{22}}{2r_{e22}}\right))=\frac{1}{4}\left(D_{11}\exp(\alpha 11)D_{22}\exp(\alpha 22)\right)^{1/2} \quad (5.15)$$

The simulations were ran using a timestep of 0.35 fs and a potential range of 6.5 Å, the same values used further for the EAM simulations. All simulations are performed at constant pressure and temperature (NPT) and using periodical boundary conditions.

5.2.1 Quenching procedure and glass transition

Some well equilibrated liquid configurations at initial temperature $T_i = 2000K$ and hydrostatic pressure $P_i = 0.135GPa$ were used as starting point for the simulations. After equilibrating the liquid configuration at these conditions, the structures were quenched until the system reached a final temperature $T_f = 300K$ and $P_f = 0GPa$. Temperature and pressure are reduced at a given time interval. The reduction for the temperature is chosen to be $\triangle T = -34K$ and pressure $\triangle P = -0.0027GPa$ and applied every 9700 timesteps. This quench rate is $\eta_1 = 10^{13}K/s$. At the final temperature the system is left to equilibrate again in NPT conditions prior starting the system analysis. The quenching rate and equilibration process will be the same in the study of the systems by using Embedded Atom Method potentials. The glass transition appears at a temperature of about $628K$.

5.2.2 Amorphous structure

In the same way that was done with the LJ systems, the existence of an amorphous structure is checked both at the end of the quenching process and after the subsequent equilibration. The verification is done by calculating the static structure factor and the pair correlation function of the samples.

The pair correlation function, Figure 5.24, shows a well defined first peak corresponding to the first neighbour.

It is interesting to notice that the first peak of the PCF is well defined, while in the case of the Lennard-Jones potential (Figure 5.24) the first peak had a clear substructure due to the three partial pair correlation functions. On the contrary, the oscillations in the Morse PCF due to the second and successive neighbours are more intense than for the Lennard-Jones case. When comparing both potentials, the main difference is that in the LJ potential the depth of the potential well is the same for both species, while in the present case the depth of the potential wells are different. The combination of a different potential well with a different atomic radius seems to allow a better atomic packing in the case of the Morse potential.

In the case of the static structure factor, Figure 5.25, no sharp peaks are observed indicating the crystallization pattern. No significant differences are found in this case with the LJ case (Figure 5.25) although the oscillation at high frequencies seem to also more intense in the Morse case. Both tests, confirm the lack of crystalline structure on the sample.

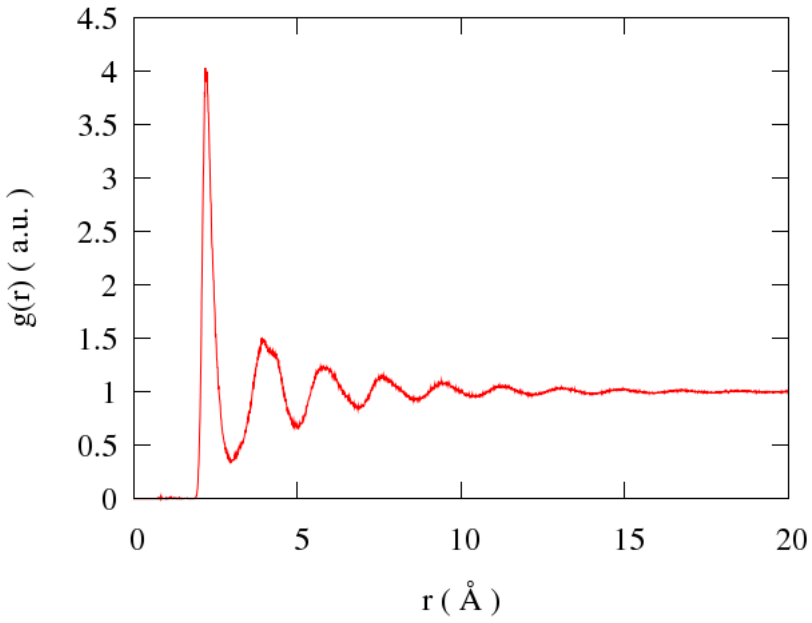

Figure 5.24: Pair Correlation Function of Morse binary system of 32000 atoms and quenching rate η_1.

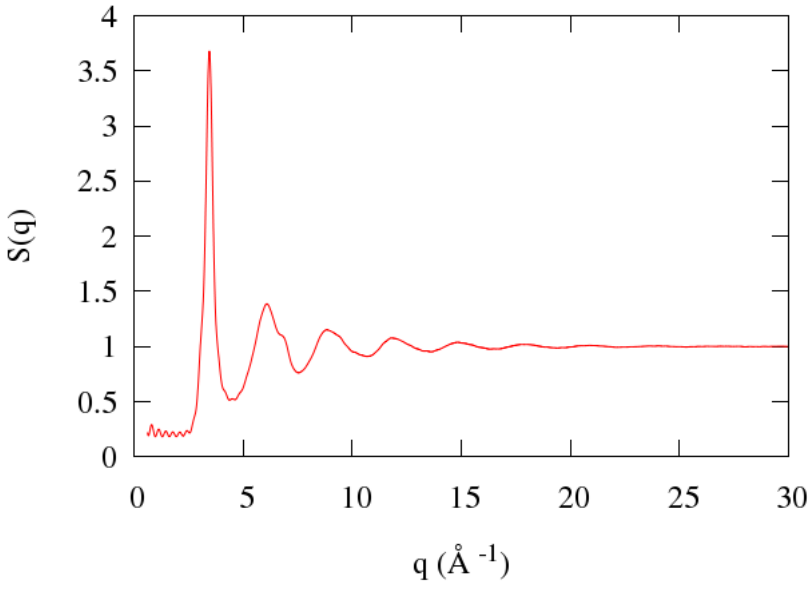

Figure 5.25: Static structure factor of Morse binary system of 32000 atoms and quenching rate η_1.

N	System	Quenching rate	q_m (Å^{-1})	PCFmax_1(Å)	PCFmax_2(Å)
32000	$Cu_{20}Pd_{80}$	$\eta_1 = 10^{13} K/s$	$3,45$	$2,2$	$4,0$

Table 5.3: Peak position q_m of S(q) and of the two main peaks max_1 and max_2 in the PCF in the studied Morse system.

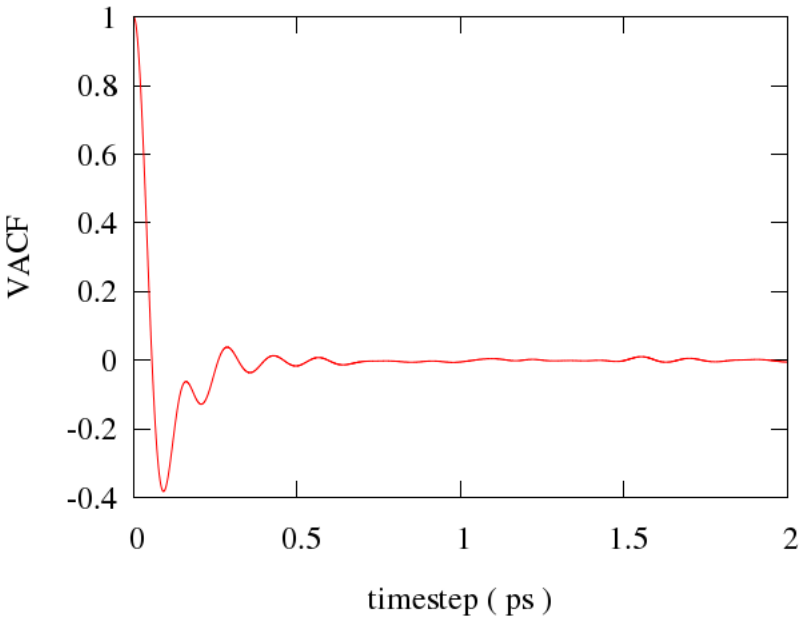

Figure 5.26: Velocity Autocorrelation Function in a Morse binary system of 32000 atoms $Pd_{80}Cu_{20}$ at the equilibrium and quenching rate η_1.

5.2.3 Vibrational Density of States

After checking the amorphous structure of the samples, the analysis of the vibrational density of states (VDOS) is performed. From the molecular dynamics trajectories at a temperature T in a well equilibrated system, the VDOS is calculated by Fourier transforming the velocity auto-correlation function (VACF), shown in Figure 5.26. The VACF tends to 0 in a timescale of about 1 ps. Comparison with the VACF computed with the Lennard-Jones potential -5.6- shows that the Morse's VACF displays several secondary peaks not present in the Lennard-Jones' VACF. The shorter extent of the Morse potential, together with the stronger atomic correlation shown in the Morse's PCF, may induce a stronger correlation between the atomic movement which may be responsible of the secondary peaks in the Morse's VACF.

The VDOS is calculated and plotted in Figure 5.27. It is noticeable that the VDOS shows two peaks, while the VDOS of the LJ system, shown in Figure 5.7, is single peaked. Due to the mixed transverse-longitudinal nature of phonons in amorphous materials it is difficult to interpret this result, which is probably related to the above cited secondary peaks of the VACF.

The Debye frequency and Debye level are calculated as specified in the pre-

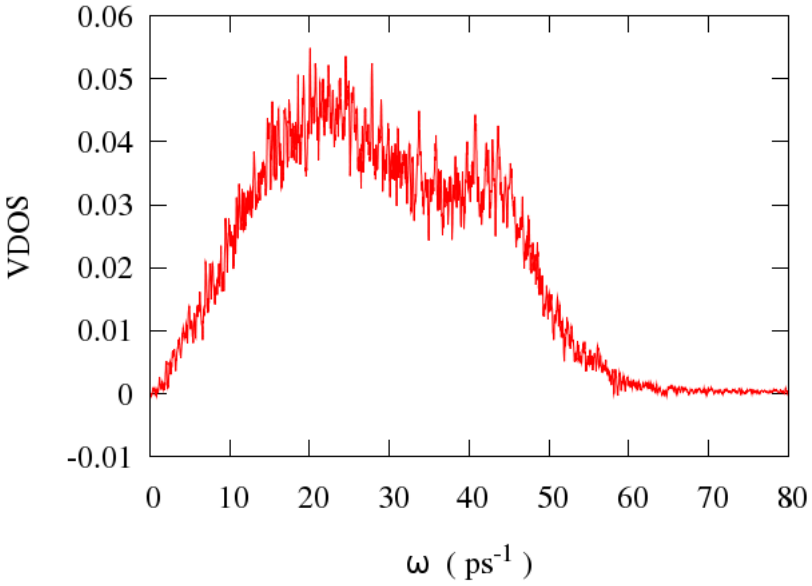

Figure 5.27: Vibrational Density of States calculated from the velocity autocorrelation function in a Morse binary system of 32000 atoms $Pd_{80}Cu_{20}$ at the equilibrium and quenching rate η_1 .

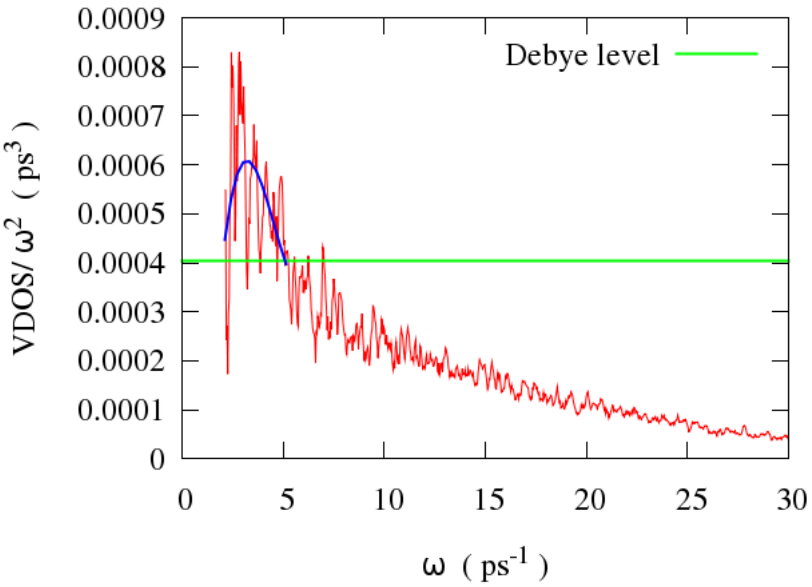

Figure 5.28: Boson Peak observed in a Morse binary system of 32000 atoms $Pd_{80}Cu_{20}$ at the equilibrium and quenching rate η_1.

N	Tg	m	c_L (km/s)	c_T (km/s)	Density (N/V)	$\varpi_{Debye})$ (ps^{-1})	*Debye level* (ps^3)
$\eta_1 = 10^{13} K/s$							
32000	628	325	$3,0$	$1,2$	$0,112$	$2,82 \cdot 10^1$	$4,03 \cdot 10^{-4}$

N	ϖ_{BP} (ps^{-1})	ϖ_{IR}^L (ps^{-1})	ϖ_{IR}^T (ps^{-1})	q_{BP}	PCF max_1	PCF max_2	q_m
$\eta_1 = 10^{13} K/s$							
32000	$3,2$	4.9	1.1	9.9	$2,2$	$14,0$	$3,45$

Table 5.4: Results obtained from simulations using the Morse potential.

vious section. In this case, the Debye level corresponding to $9/\omega_D^3$ has a value of $4{\cdot}10^{-4} ps$. The Boson Peak designates and excess over the Debye level in the vibration density of states at low frequencies. In Figure 5.28, a well defined Boson Peak is observed with a maximum at $\omega_{BP} = 3.2 ps^{-1}$. These values are in qualitative agreement with the available experimental data [50, 42]. Comparing to the BP found in the LJ case, there are no significant differences.

A review of all the data calculated is presented in table 5.4. The values of the macroscopic sound velocities (c_L, c_T), density (N/V), Debye frequency (ω_D), Boson Peak position (ω_{BP}), Boson Peak maximum intensity (I_{BP}), the Ioffe-Regel frequencies (ω_{IR}^L,ω_{IR}^T) ,

5.2.4 Dynamic Structure Factor (S(q,w))

The dynamic structure factor for longitudinal excitations is calculated for different wave vectors, and is shown in Figure 5.29. The wave vectors considered, are defined as $q_i = 2\pi k_i/L$, where L is the box length and k_i=1,2,...n.

It can be observed that the width of the peak in $S(q,\omega)$ increases and the characteristic frequency is shifted to higher frequencies, as the wave-vector (q) is increased. As in the previous cases, the shape of the resonance peak is fitted by a damped harmonic oscillator model, as shown in Figure 5.30.

The Ioffe-Regel limit condition is given by:

$$\Omega(q) = \pi\Gamma(q) \tag{5.16}$$

In Figure 5.31, a linear dispersion relation is observed for $\Omega(q)$ for the longitudinal and transverse phonons. For low q wave vectors it has a linear behaviors that bends when increasing q.

In this case, the Iofffe-Regel limit for the longitudinal wave, ω_{IR}^L, is determined as $0.004966 fs^{-1}$ and for the transverse wave, ω_{IR}^T, as $0.00112 fs^{-1}$. When comparing both IR limits we find that $\omega_{IR}^L > \omega_{BP}$ as obtained in a similar system ($Pd_{77}Si_{16.5}Cu_{6.5}$) studied by Inelastic X-Ray Scattering (IXS).

Moreover, some extra information can be obtained from the q dependence on the apparent sound phase velocity. This apparent sound phase velocity is defined as:

$$c_{L,T=}\frac{\Omega_{L,T}(q)}{q} \tag{5.17}$$

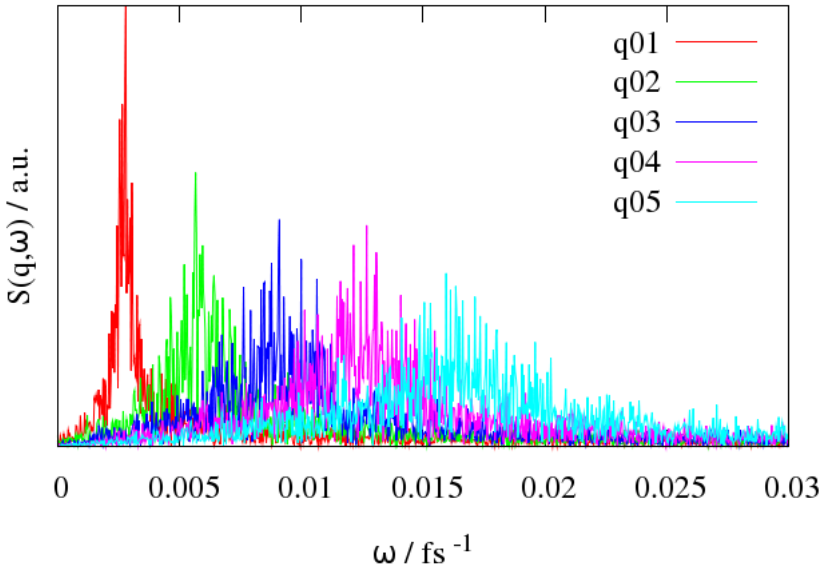

Figure 5.29: Longitudinal dynamic structure factor for 5 different q wave vectors of the Morse binary system of 32000 atoms $Pd_{80}Cu_{20}$ at the equilibrium, after quenching at a cooling rate η_1 .

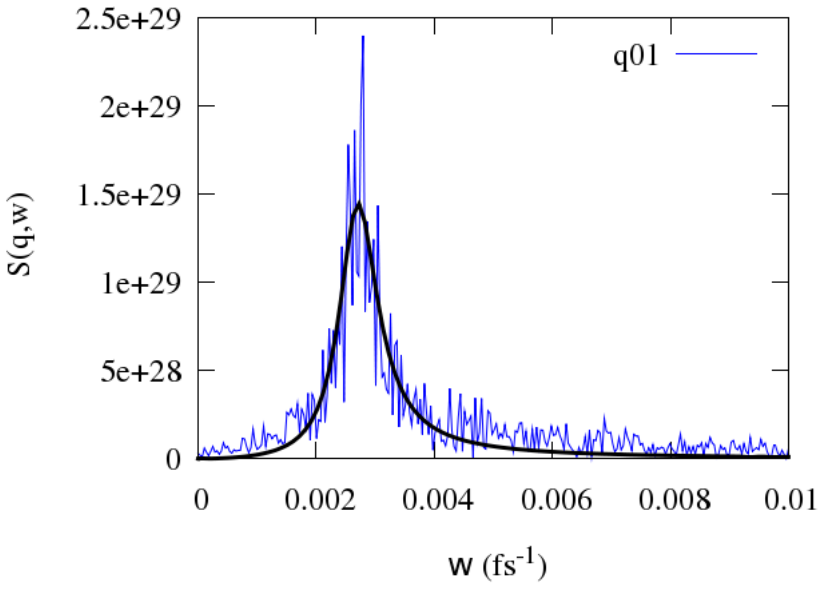

Figure 5.30: Fit for the longitudinal dynamic structure factor for a wave-vector q in the Morse binary system of 32000 atoms $Pd_{80}Cu_{20}$ at the equilibrium , after quenching at a cooling rate η_1.

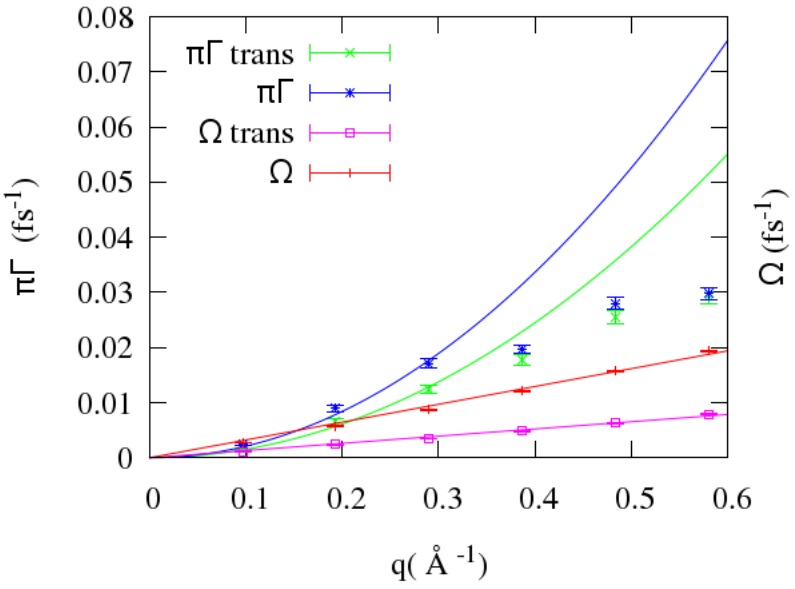

Figure 5.31: Dispersion curve $\Omega_{L,T}(q)$ and broadening $\pi\Gamma_{L,T}(q)$ obtained from $S_{L,T}(q,\omega)$ of a Morse binary system of 32000 atoms $Pd_{80}Cu_{20}$ and quenching rate η_1.

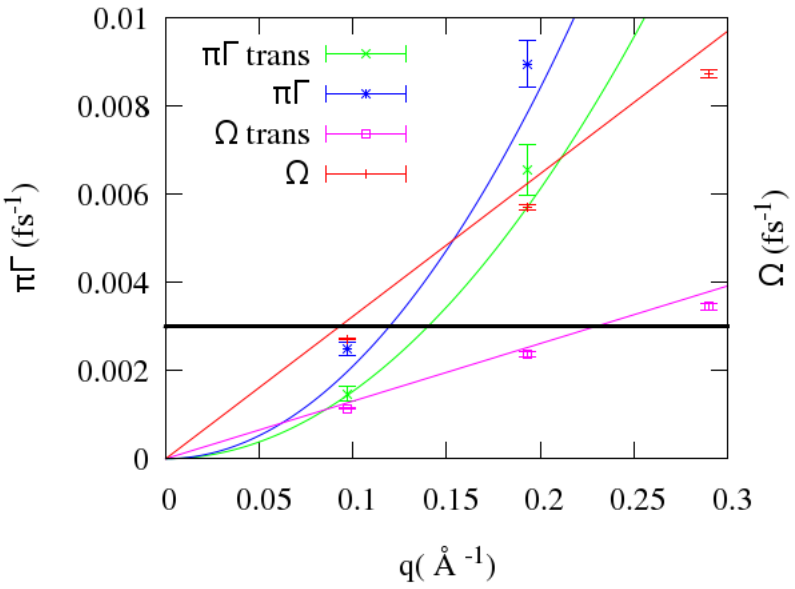

Figure 5.32: Dispersion curve $\Omega_{L,T}(q)$ and broadening $\pi\Gamma_{L,T}(q)$ obtained from $S_{L,T}(q,\omega)$ and frequency of the Boson Peak of a Morse binary system of 32000 atoms $Pd_{80}Cu_{20}$ and quenching rate η_1.

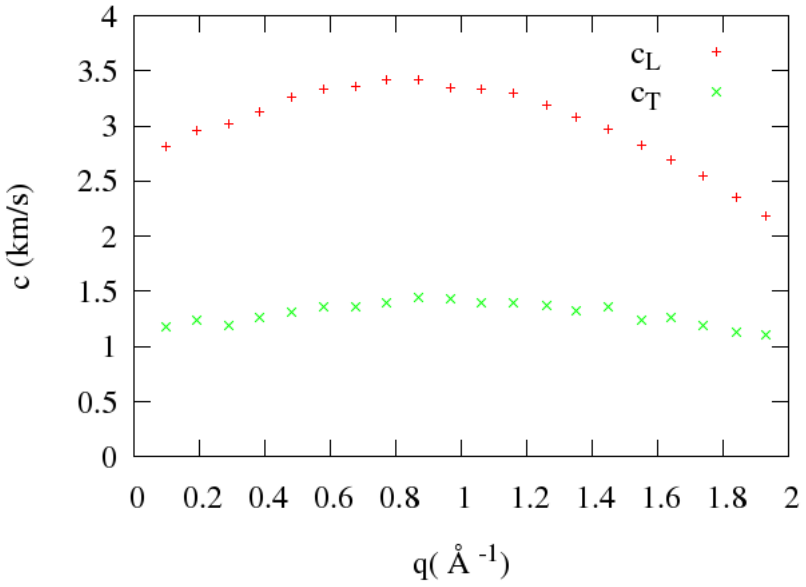

Figure 5.33: Apparent longitudinal and transverse phase velocity as a function of moment transfer q in a Morse binary system of 32000 atoms $Pd_{80}Cu_{20}$ and quenching rate η_1.

In Figure 5.33, the apparent sound phase velocity is represented for the transverse and longitudinal case having values of $\sim 1.3km/s$ and $\sim 3.4km/s$. Both velocities have roughly the same behaviours, showing a maximum around $q \sim 0.8 - 1\text{Å}^{-1}$. The experimental evidence on this point is contradictory [49, 46, 88, 48, 47]

The apparent sound velocity displays a reduction of 20% at very low wave vectors for small q vectors for the longitudinal case, see Figure 5.34. Below q_{BP}, where the softening appears $\Gamma(q) \propto q^4$. This behaviour is attributed to Rayleigh-like scattering of the acoustic waves with the elastic heterogeneities of the glass. This theoretical q^4 regime can not be studied due to the small size of the system studied; Figure 5.34 shows that only one of the computed q-values falls into that regime.

Moving to higher frequencies, the sound speed increases until it reaches a small plateau. This area is characterized for a quadratic dependence $\Gamma(q) \propto q^2$ that persists until the bending starts. This change occurs at 1.6Å^{-1} when approaching the Brillouin zone $q_m/2$, where q_m is the position of the maximum of the static structure factor $S(q)$, see Figure 5.25.

In the same way that with the sound speed, two different regions are also observed when displaying the q-dependence of the damping of the acoustic excitations. For small frequencies the damping acoustic excitation shows a linear behavior that changes to a quadratic one as this frequency increases. This transition occurs at q=0.3 A^{-1} in agreement with the Boson Peak position frequency.

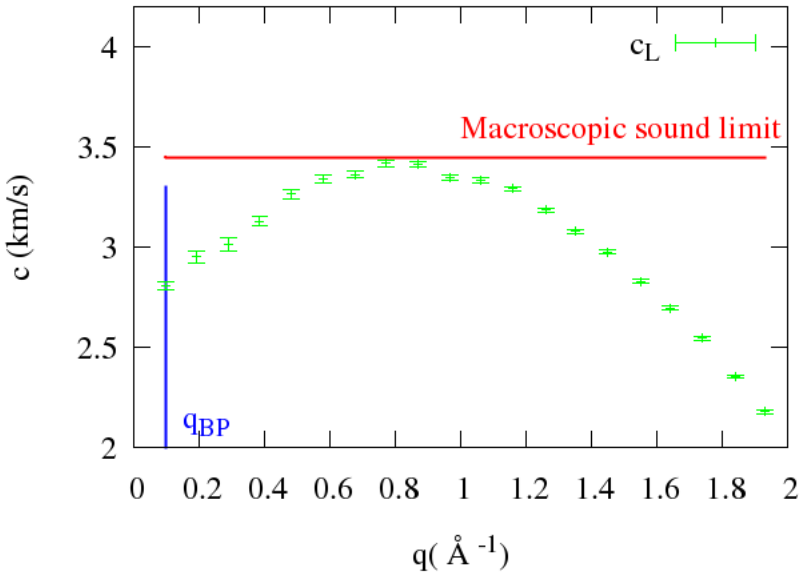

Figure 5.34: Apparent longitudinal phase velocity as a function of moment transfer q , q_{BP} and macroscopic sound limit in a Morse binary system of 32000 atoms $Pd_{80}Cu_{20}$ and quenching rate η_1.

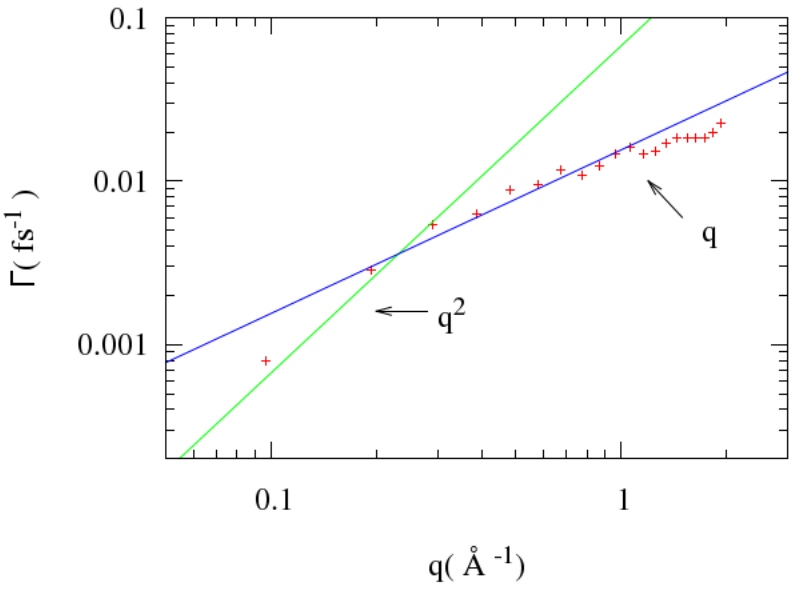

Figure 5.35: q-dependence of the acoustic excitations for the longitudinal in a Morse binary system of 32000 atoms $Pd_{80}Cu_{20}$ and quenching rate η_1.

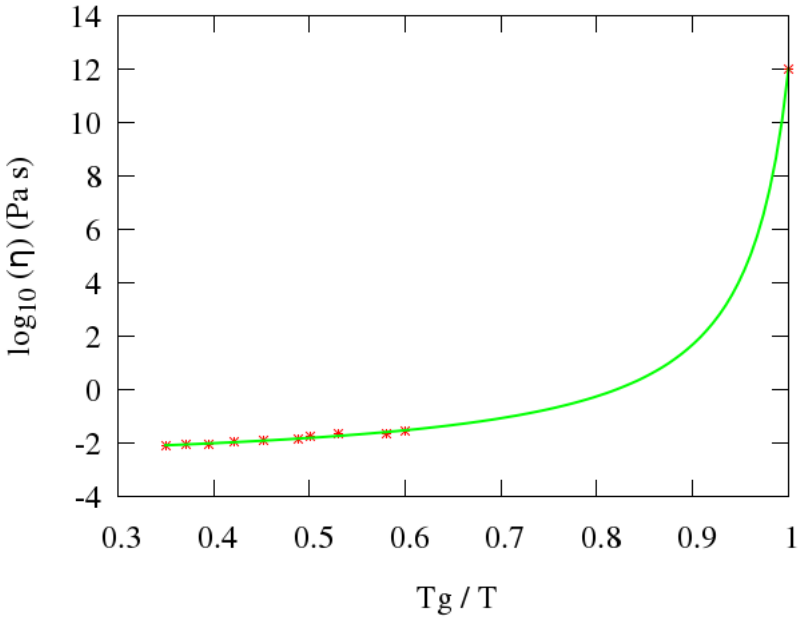

Figure 5.36: Fragility obtained for a binary Morse system of 32000 atoms and quenching rate η_2.

5.2.5 Viscosity

Using the same methodology than for the Lennard-Jones potential, the shear viscosity is calculated. The binary system $Pd_{80}Cu_{20}$ of 32000 atoms obtained with a fast quenching rate is used for the calculations. The stress auto-correlation function is calculated at different temperatures. The viscosity is calculated at $1796K$, $1694K$, $1592K$, $1490K$, $1388K$, $1286K$, $1252K$, $1184K$, $1082K$ and $1048K$. using the Green-Kubo formula. The shear stress as a function of time required for the Green-Kubo relation is determined in the standard way from atomic forces, positions and volume from simulations.

Then, the Vogel-Fulcher-Tammann relationship was fit to the viscosity to construct the Angell plot.

Following the same procedure than with LJ and EAM systems the fragility is determined, $m = 325$, and the glass transition Temperature $T_g = 628K$ [111]. The Morse potential glass results to be quite stronger than the Lennard-Jones glass, as expected.

The value of the fragility obtained in this simulation is higher than those obtained experimentally. It is likely that this fact is related to the extremely high quenching rates used in simulations, as it is known experimentally that fragility increases with the quenching rate [111].

5.3 Embedded atom systems (EAM)

In this section we present the results of large scale MD simulations in binary metallic glasses $Cu_{50}Pd_{50}$ and $Cu_{20}Pd_{80}$ by using Embedded Atom Method

(EAM) potentials. Similarly to the previous sections, different relaxation states are obtained by changing the quenching rates of the simulated MGs.

The masses of the particles are taken as $m_{Pd} = 106.42$ AMU and $m_{Cu} = 63.546$ AMU. The EAM potentials parametrization is obtained from Ref. [112] The simulations are run using a timestep 0.35fs and a potential range of 6.5 as in the case of the Morse potential. All simulations are carried out at constant pressure and temperature (NPT). Periodic boundary conditions are used for the study of all systems.

The results presented in this section will be given in physical units, as the parameters defining the EAM potential are intended to simulate the real bonding of the metallic species. The EAM potential does not allow us to define a clear value of σ. However, in order to compare with the results of the LJ simulation of the previous section, the approximate relations $\sigma \approx 3$Å and $\tau \approx 0,5$ps can be used by the reader.

5.3.1 Quenching procedure and glass transition

The liquid configurations are equilibrated at initial temperature $T_i = 2000K$ and hydrostatic pressure $P_i = 0.135GPa$. Once at the equilibrium, the structures are quenched until reaching a final temperature $T_f = 300K$ and $P_f = 0GPa$. Temperature and pressure are reduced at a given time interval. The reduction for the temperature is chosen to be $\triangle T = -34K$ and pressure $\triangle p = -0.0027GPa$ and applied at 9700 and 97000 timesteps. These two quenching rates correspond to $\eta_1 = 10^{13}K/s$ and $\eta_2 = 10^{12}K/s$. At the final temperature the system is left to equilibrate again in NPT conditions prior starting the system analysis.

Two different size systems containing 32000 and $4 \cdot 10^6$ atoms were studied applying the quenching rates η_1 and η_2 for both compositions, $Cu_{50}Pd_{50}$ and $Cu_{20}Pd_{80}$. The average size of the simulation boxes were $L = 89.2$Å and $L = 440$Å for the $Cu_{50}Pd_{50}$ system and $L = 89.9$Å and $L = 449$Å for the $Cu_{20}Pd_{80}$ system.

Figure 5.37 shows the volume per atom along the quenching process, Showing the glass transition at a temperature of about ~$1080K$. As will be discussed in the next section, this value is somewhat larger than that found by using Morse potentials ($T_g = 628K$). This indicates that the EAM potential is more attractive than the Morse potential, due to the indirect interaction between neighbouring atoms through the electronic density.

5.3.2 Amorphous structure

In the same way that was done with the Lennard-Jones and Morse systems, the pair correlation function, PCF, and the static structure factor $S(q)$ are calculated to check the amorphous structure of the system.

As expected in liquids and amorphous materials, the radial distribution function, Figure 5.38, shows only a clear maximum at the distance of first neighbors. The substructure of the first peak due to the partial distributions of AA, AB and BB atom pairs, that was clearly seen in the $A_{80}B_{20}$ LJ simulations, is only slightly perceived in the $Cu_{20}Pd_{80}$ system, as happened in the simulation performed using Morse potentials.

Analogously, the static structure factor (see Figure 5.39) shows no sharp peaks, indicative of crystalline reflections. The positions of the main peaks of

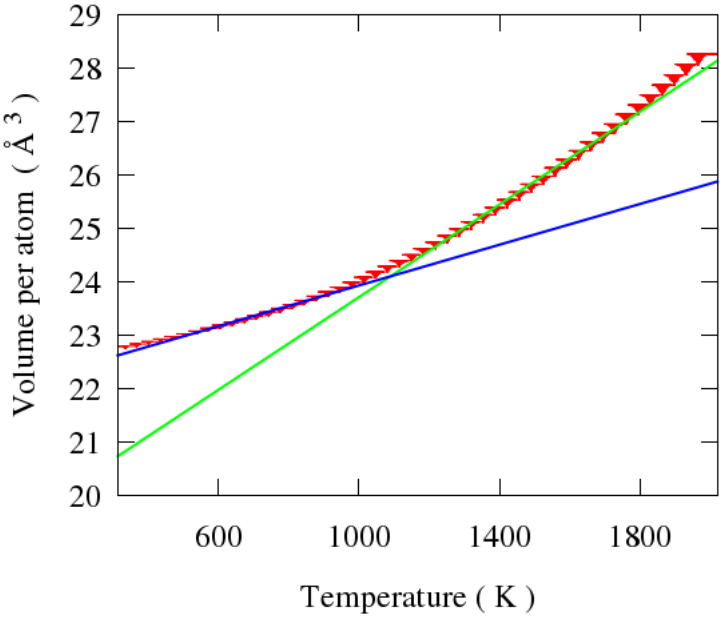

Figure 5.37: Change on the volume per atom during the quench η_1 in a EAM binary system of $4 \cdot 10^6$ atoms.

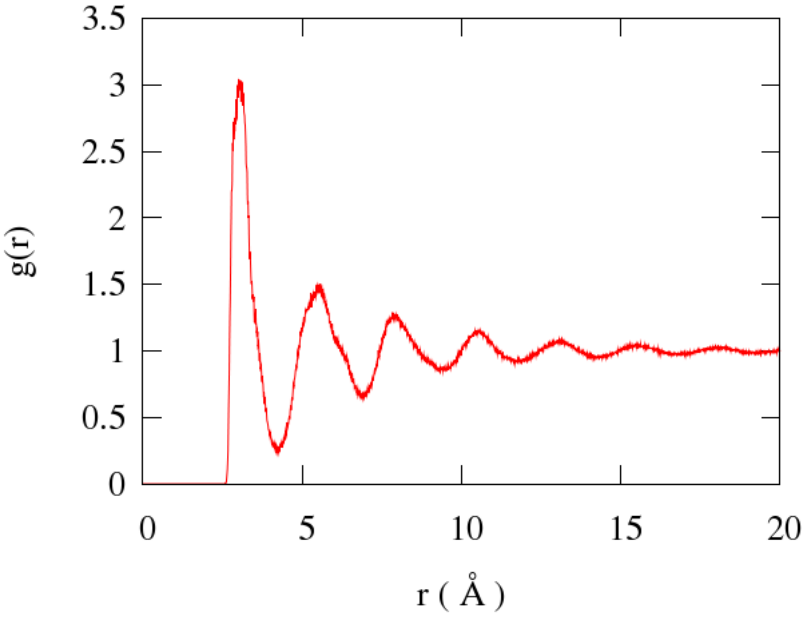

Figure 5.38: Pair Correlation Function of EAM $Cu_{20}Pd_{80}$ binary system of 32000 atoms and quenching rate η_2 at T=300K.

N	System	Quenching rate	q_m (Å^{-1})	PCFmax_1(Å)	PCFmax_2(Å)
32000	$Cu_{20}Pd_{80}$	$\eta_1 = 10^{13} K/s$	$2,5$	$3,00$	$5,56$
32000	$Cu_{20}Pd_{80}$	$\eta_2 = 10^{12} K/s$	$2,5$	$3,08$	$5,58$
32000	$Cu_{50}Pd_{50}$	$\eta_1 = 10^{13} K/s$	$2,5$	$2,86$	$5,10$
32000	$Cu_{50}Pd_{50}$	$\eta_2 = 10^{12} K/s$	$2,5$	$2,85$	$5,08$

Table 5.5: Pic position for the S(q) and PCF for the EAM systems studied.

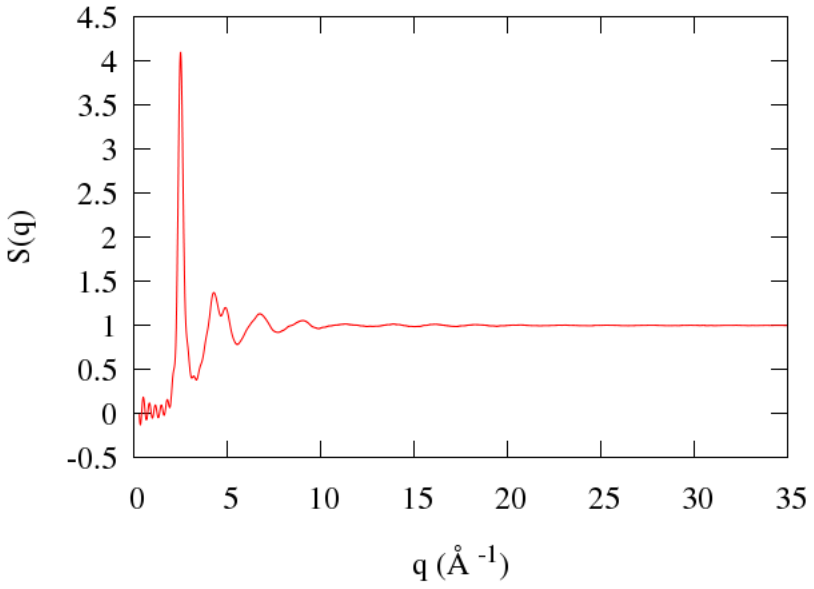

Figure 5.39: Static structure factor of EAM $Cu_{20}Pd_{80}$ binary system of 32000 atoms and quenching rate η_2.

the PCF and the $S(q)$ depend slightly on the quenching rate and system size, as found in Table 5.5. The PCF and $S(q)$ obtained from the simulations have the same basic features obtained experimentally in many metallic glasses and particularly in Pd-based systems [113].

The changes in particle density between the fast and slow cooling rates was found to be $0,1\%$. No significant changes are found in the PCF or the $S(q)$ when modifying the cooling rate or the box size, as in Lennard-Jones and Morse simulations previously reported.

5.3.3 Vibrational Density of States

Following the same procedure than in previous simulations, the velocity auto-correlation function was computed and it is shown in Figure 5.40.

The VDOS is calculated and plotted in Figure 5.41. It can be seen that the large number of atoms in the simulation box allows us to obtain a much lower

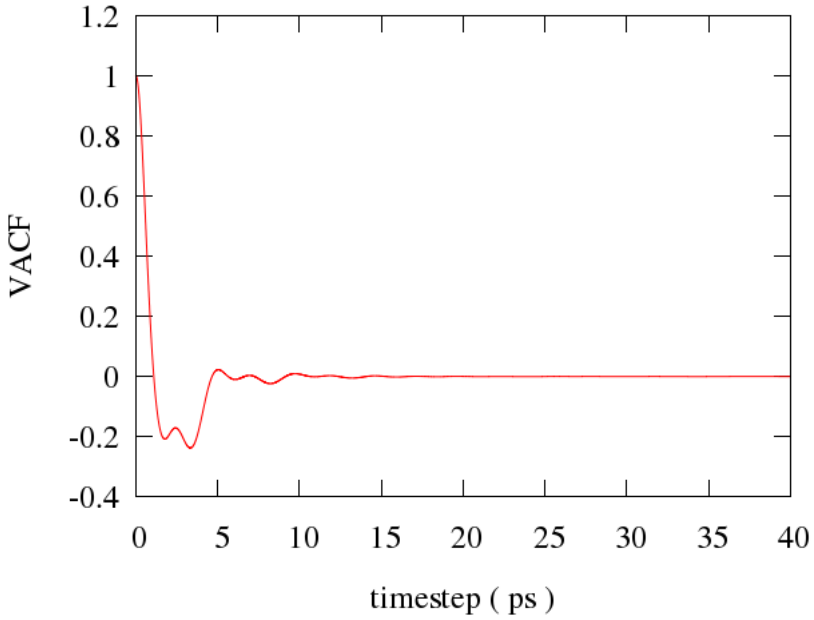

Figure 5.40: Velocity autocorrelation function calculated in EAM $Cu_{20}Pd_{80}$ binary system of $4 \cdot 10^6$ atoms and quenching rate η_2.

noise in the determination of the VDOS. For low frequencies, the VDOS displays a quadratic behavior, see Figure 5.41. Both the VACF and the VDOS have the same qualitative behaviour than those computed with the Morse potential.

The study of the Debye level and the Boson peak was performed for all the samples, in table 5.1 the values of the macroscopic sound velocities (c_L, c_T), density (N/V), Debye frequency (ω_D), Boson Peak position (ω_{BP}), Boson Peak maximum intensity (I_{BP}) and the Ioffe-Regel frequencies (ω^L_{IR},ω^T_{IR},), the peak positions for the pair correlation function ($max_1(PCF)$, $max_2(PCF)$) and the maximum for the static structure factor (q_m) are detailed for all the systems studied.

The Debye level for the system has a value $5.49 \cdot 10^{-4} ps^3$, corresponding to $3/\omega_D^3$.

The effect of the quenching rate and the box size on the Debye level is analyzed, see Figure 5.43. Different results although with similar behavior are obtained for the different compositions studied. As in the studied LJ simulations, the quenching rate produces a slight increase on the Debye level. As it happens with the Lennard-Jones systems, the structures obtained by applying slower quenching rates are more relaxed, leading to more dense structures and consequently affecting the sound speed and so on the Debye level.

The Boson Peak designates an enhancement over the Debye level $9/\omega_D^3$ in the vibration density of states at low frequency, which is characterized by a maximum in the plot of the reduced VDOS, see Figure 5.42. The Boson peak is observed at around $2ps^{-1}$ and $7.5ps^{-1}$ for the $Cu_{20}Pd_{80}$ and $Cu_{50}Pd_{50}$ respectively.

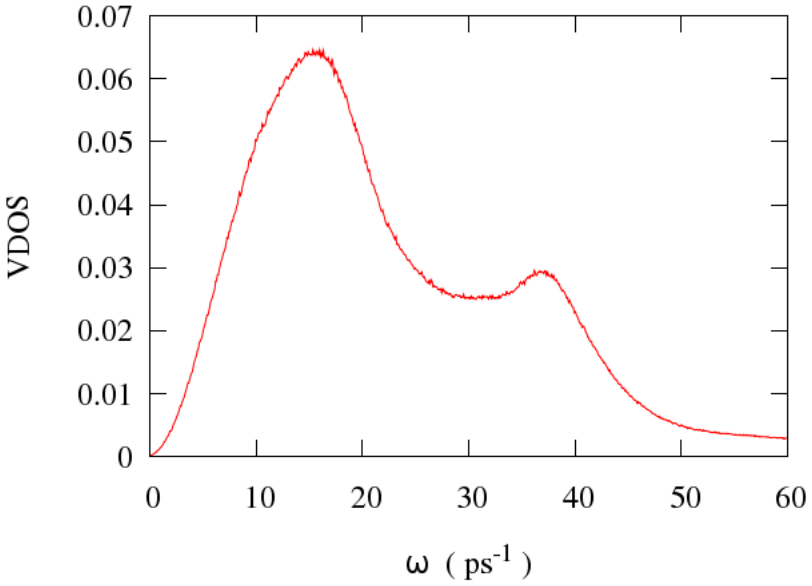

Figure 5.41: Vibrational Density of States calculated from the velocity autocorrelation function in EAM $Cu_{20}Pd_{80}$ binary system of $4{\cdot}10^6$ atoms and quenching rate η_2.

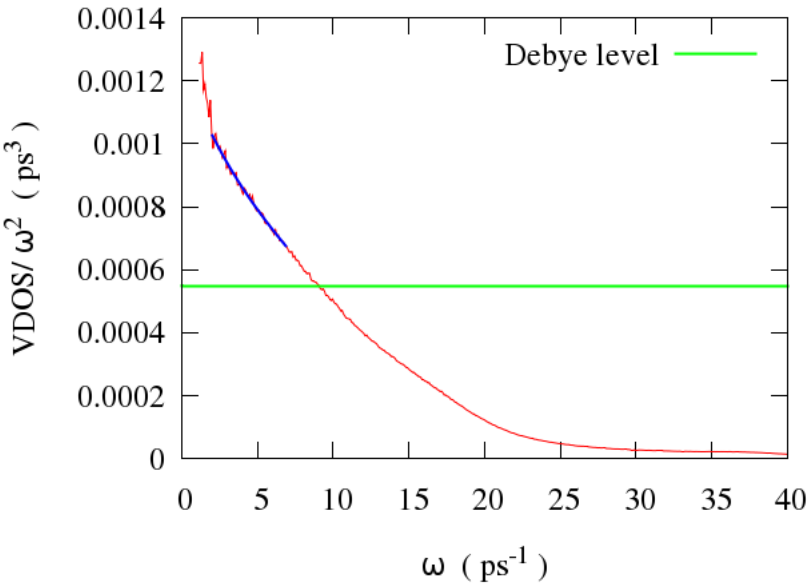

Figure 5.42: Boson Peak observed in a EAM $Cu_{20}Pd_{80}$ binary system of $4 \cdot 10^6$ atoms and quenching rate η_1.

N	c_L (km/s)	c_T (km/s)	Density (N/V)	ϖ_{Debye} (ps^{-1})	*Debye level* (ps^3)	ϖ_{BP} (ps^{-1})	ϖ_{IR}^{L} (ps^{-1})	ϖ_{IR}^{T} (ps^{-1})	q_{BP}	PCF max_1	PCF max_2	q_m
$\eta_1 = 10^{13} K/s$												
$Cu_{20}Pd_{80}$												
32000	*3,297*	*1,500*	*0,0440*	$2,52 \cdot 10^1$	$5,60 \cdot 10^{-4}$	*1,25*	2,7	1,3	*0,038*	3,00	5,56	2,5
4000000	*3,274*	*1,504*	*0,0439*	$2,52 \cdot 10^1$	$5,59 \cdot 10^{-4}$	*2,001*	3,0	1,0	*0,060*	2,99	5,56	2,5
$Cu_{50}Pd_{50}$												
32000	*5,201*	*2,549*	*0,0473*	$3,59 \cdot 10^1$	$1,11 \cdot 10^{-4}$	7,5	5,7	3,7	0,140	3,08	5,58	2,5
4000000	*5,342*	*2,484*	*0,0472*	$4,26 \cdot 10^1$	$1,16 \cdot 10^{-4}$	-	5,2	2,4	-	-	-	2,5
$\eta_2 = 10^{12} K/s$												
$Cu_{20}Pd_{80}$												
32000	3,304	1,529	*0,0442*	$2,57 \cdot 10^1$	$5,31 \cdot 10^{-4}$	0,99	3,2	1,5	0,030	2,86	5,10	2,5
4000000	3,274	1,514	*0,0440*	$2,54 \cdot 10^1$	$5,49 \cdot 10^{-4}$	2,03	2,7	1,4	0,061	-	-	2,5
$Cu_{50}Pd_{50}$												
32000	5,211	2,567	*0,0428*	$4,21 \cdot 10^1$	$1,20 \cdot 10^{-4}$	8,96	6,23	3,86	0,163	2,85	5,08	2,5
4000000	5,342	2,556	*0,0470*	$4,35 \cdot 10^1$	$1,09 \cdot 10^{-4}$	-	5,28	2,25	-	-	-	2,5

Table 5.6: Results obtained from simulations using EAM potential.

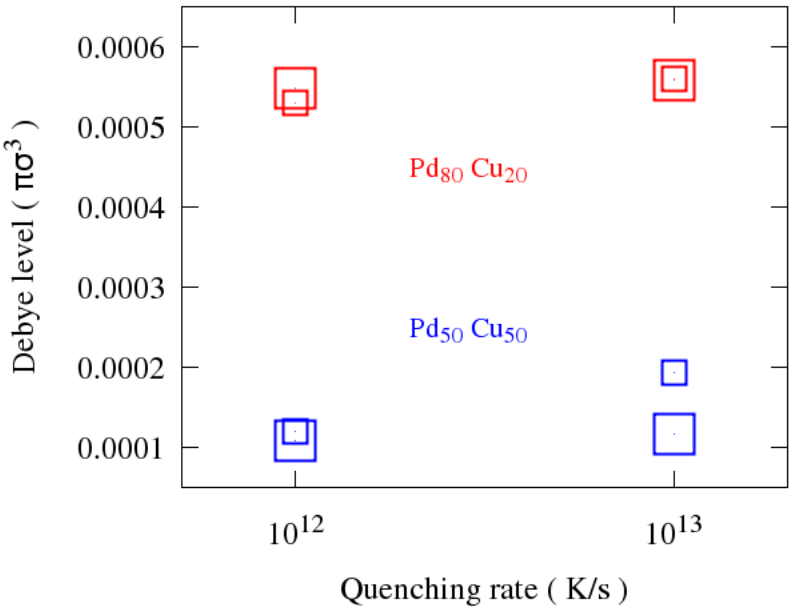

Figure 5.43: Debye level versus quenching rate determined in simulation boxes of different sizes ($3{\cdot}10^4$ and $4{\cdot}10^6$ atoms) and different concentrations, indicated by the size of the corresponding symbol and the color.

In the previous simulation performed using Morse potentials simulations, the BP was found at a frequency of $3,2ps^{-1}$. Thus, there is a qualitative agreement between the results of both simulations, but it seems that the dynamical properties are somewhat different in both cases.

For all the systems studied, the Boson peak is reproduced. Figure 5.44 and Figure 5.45, shows the Boson peak obtained for the binary $Cu_{20}Pd_{80}$ and $Cu_{50}Pd_{50}$, respectively, obtained by applying a fast, η_1, and a medium, η_2, quench.

The position and intensity of the Boson peak changes by modifying the quenching rate. Figure 5.44 and Figure 5.45 show that the intensity of the Boson peak increases when applying a faster quenching rate. Moreover, the position of the Boson peak is slightly shifted to smaller frequencies. Again, more relaxed systems with higher density produce an increase on the elastic constants. However, the changes are almost not affected by the size effects, showing only a small increase in the frequency for bigger systems.

These results are in qualitative agreement with the ones obtained studying Lennard-Jones systems. Furthermore, these results are in concordance with those published by N. Jakse in their study of EAM binary $Cu_{50}Zr_{50}$ [42], although the difference on sound velocities affects them.

It is interesting to realize the difference in the BP position and shape when comparing the results for $Cu_{20}Pd_{80}$ and $Cu_{50}Pd_{50}$. The BP position moves to higher frequencies when the concentration of Cu - light - atoms is increased, and the BP is much more sharper when the concentration difference is large than when both concentrations are equal. It is expected that in $Cu_{20}Pd_{80}$ the

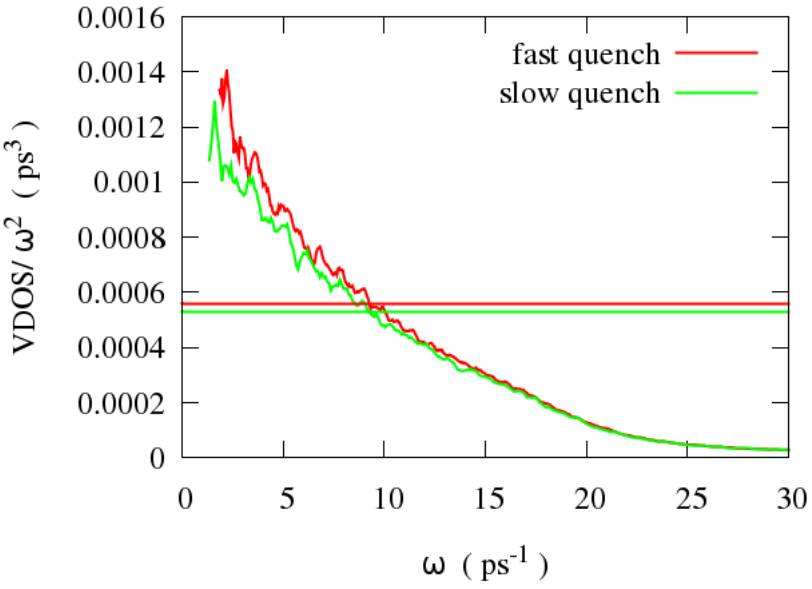

Figure 5.44: Effect of the quench rate on the Boson peak position and intensity in a EAM binary $Cu_{20}Pd_{80}$ system of 32000 atoms with fast (η_1) and slow (η_2) quenching rate.

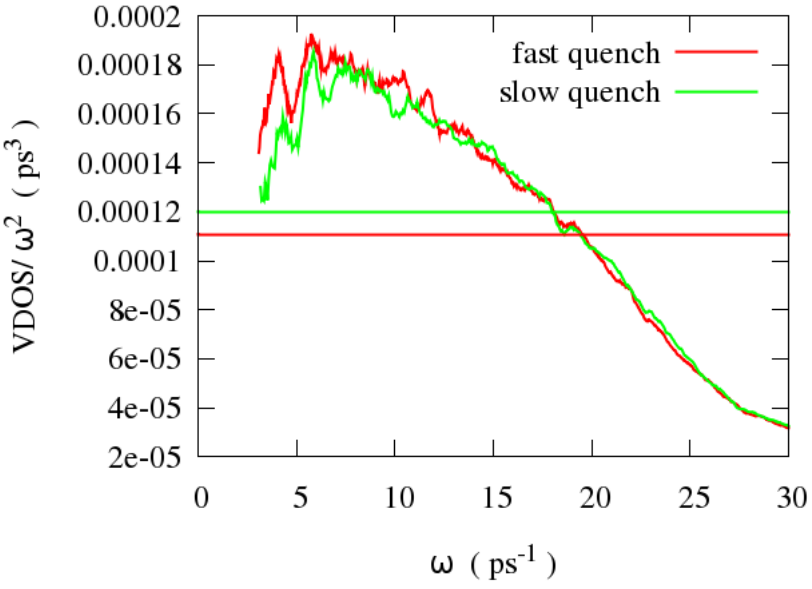

Figure 5.45: Effect of the quench rate on the Boson peak position and intensity in a EAM binary $Cu_{50}Pd_{50}$ system of 32000 atoms with fast (η_1) and slow (η_2) quenching rate.

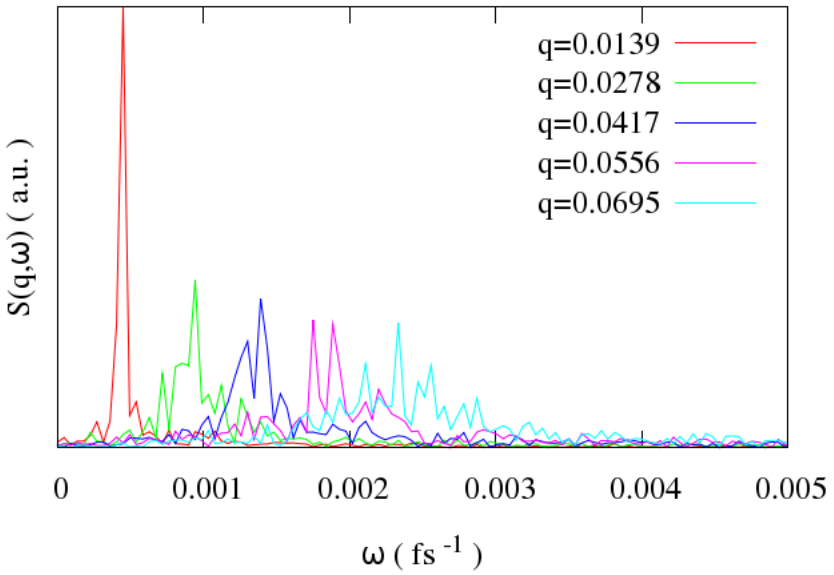

Figure 5.46: Longitudinal dynamic structure factor for 5 different q wave vectors in a EAM $Cu_{20}Pd_{80}$ binary system of $4 \cdot 10^6$ atoms at equilibrium , after quenching at a cooling rate η_2 .

dynamics are dominated by the behaviour of Pd atoms, which are heavier than Cu atoms. In these conditions, lower frequency states are more probable than when the concentration of Cu atoms is increased.

The wavelengths of the acoustic excitations with frequencies in the range of the BP are $\frac{c_L}{\omega_{BP}} = 1.63$nm, $\frac{c_T}{\omega_{BP}} = 0.75$nm and $\frac{c_L}{\omega_{BP}} = 0.58$nm, $\frac{c_T}{\omega_{BP}} = 0.29$nm for the $Cu_{20}Pd_{80}$ and $Cu_{50}Pd_{50}$systems respectively. For the $Cu_{20}Pd_{80}$ system, the BP region is at very low q-values, this difficulting the analysis of the system dynamics (see following section). It is interesting to note that the expected increase of sound speed, due to the increase of concentration of lighter Cu atoms, can not explain the ω_{BP} shift towards higher frequencies. The increase in frequency does not scale with the increase in sound speed and part of it has to be attributed to the effect of the different disordered structures, with the localised states interacting with acoustic excitations with characteristic wavelengths basically dependent on the average mass of the atoms.

5.3.4 Dynamic Structure Factor (S(q,ω))

The dynamic Structure factor, $S(q,\omega)$, for longitudinal and transverse excitations is calculated for different wave vectors in the same way that was done for Lennard-Jones systems.

Figure 5.46 shows $S(q,\omega)$ for different values of the wavevector q. The average phonon frequency, $\Omega(q)$, defined by the position of the maximum of $S(q,\omega)$, shifts to higher frequencies as the wave vector q increases. The full

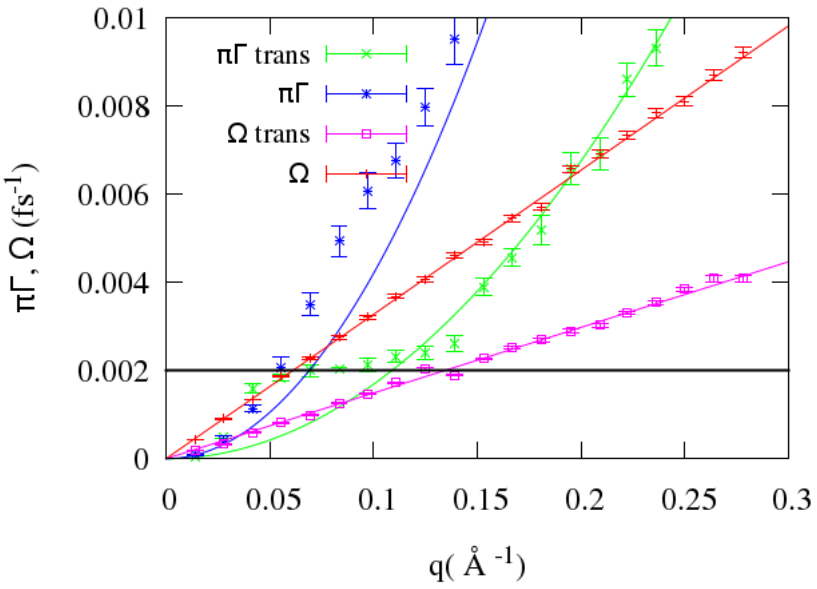

Figure 5.47: Dispersion curve $\Omega_{L,T}(q)$ and broadening $\pi\Gamma_{L,T}(q)$ obtained from $S_{L,T}(q,\omega)$ and frequency of the Boson Peak of a EAM $Cu_{20}Pd_{80}$ binary system of $4 \cdot 10^6$ atoms at equilibrium , after quenching at a cooling rate η_2 .

width maximum $\Gamma(q)$ is a measure of the damping of the acoustic excitations and its increase with the wavenumber indicates a decrease of the coherence length of the phonons. $S(q,\omega)$ presents a behaviour analogous to that found in the studied Lennard-Jones and Morse systems and also results available in the bibliography [88, 114, 44, 42, 46]

The corresponding dispersion relations are computed for the different systems and quenching rates. Figure 5.47 shows the dispersion curve $\Omega_{L,T}(q)$ together with the Boson peak frequency Ω_{BP} of a EAM $Cu_{20}Pd_{80}$ binary system of $4 \cdot 10^6$ atoms obtained with a cooling rate $\eta_2 = 10^{12}\,[K/s]$. According to the dispersion relation and the frequency of the BP $q_{BP} = 0.061\text{Å}^{-1}$. The q_{BP} is calculated for all the systems $Cu_{20}Pd_{80}$ and for the small systems $Cu_{50}Pd_{50}$. In $Cu_{50}Pd_{50}$, q_{BP} increases as the quenching rate decreases due to the effect of the relaxation state on the slope of the dispersion curve, and it is higher for smaller systems, see Figure 5.48. This results are similar to that obtained studying the Lennard-Jones systems. In $Cu_{20}Pd_{80}$, however, the values of q_{BP} are very low due to the highest concentration of heavy atoms, and it is not possible to confirm this tendency.

As discussed before, the BP frequency and the sound velocities (specially in the case of the transverse polarization) are shifted towards significantly low values in the $Cu_{20}Pd_{80}$ system. This generates a small range of ω-values were the different effects related to the BP are observed. From Figure 5.47, the Ioffe-Regel, $\Omega(q) = \pi\Gamma(q)$, is determined for the longitudinal waves, ω_{IR}^{L}, as $2,7ps^{-1}$. For the transverse waves the $\pi\Gamma(q)$ shows values above the dispersion relation in all the computed q-values indicating that the damping suppresses the

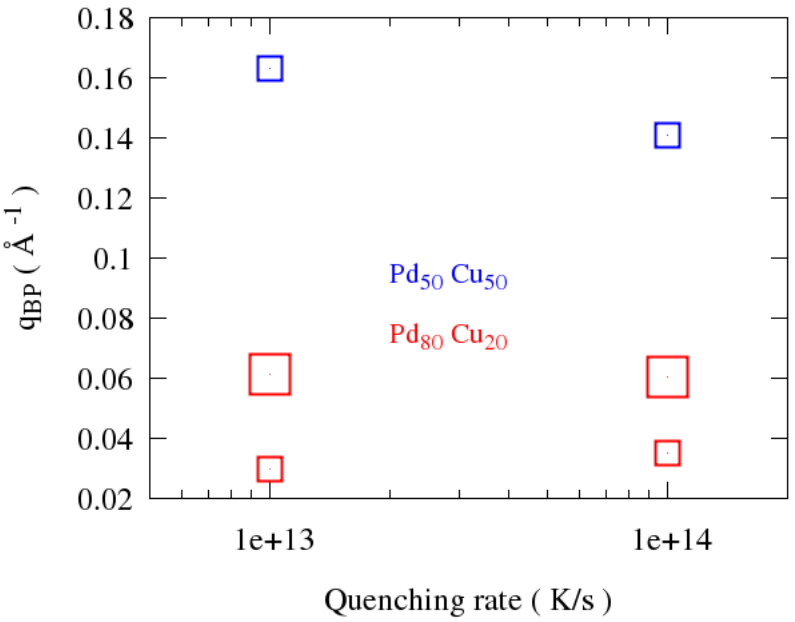

Figure 5.48: q_{BP} versus quenching rate determined in simulation boxes of different sizes ($3 \cdot 10^4$ and $4 \cdot 10^6$ atoms) and different concentrations indicated by the size of the corresponding symboland the color.

propagating nature of the transverse modes even for wavelengths of the order of the size of the simulation box. Assuming a parabolic law, $\Gamma(q) \propto q^2$, ω_{IR}^T would be below $1.4ps^{-1}$. These values compare well with those found in the simulations using Morse potentials, where $\omega_{IR}^L = 4.966ps^{-1}$ and $\omega_{IR}^T = 1.12ps^{-1}$.

By increasing the size of the system, the composition, and modifying the quenching rate these values change. Figure 5.49 presents the values of ω_{IR} obtained for different system compositions and sizes, and applying different quenching rates. As it is expected, ω_{IR}^L is higher than ω_{IR}^T . Moreover, the composition $Cu_{50}Pd_{50}$ presents in all cases larger values for ω_{IR}^L and ω_{IR}^T than the systems $Cu_{20}Pd_{80}$. This is consistent with the decrease in the density of the system as the Cu/Pd concentration ratio is increased. Furthermore, for the case of $Cu_{50}Pd_{50}$, the frequency range of BP is expanded and this allows a better determination of the $\Omega(q)$ and $\Gamma(q)$ curves in such region. In Figure A.58 (Appendix A) the Ioffe-Regel limits are clearly defined obtaining $\omega_{IR}^L = 0.0057ps^{-1}$ $\omega_{IR}^T = 0.0036ps^{-1}$.

Figure 5.47 also shows the Boson frequency, ω_{BP} $Cu_{20}Pd_{80}$ system. In agreement with the results obtained studying the Lennard-Jones systems $\omega_{IR}^L > \omega_{BP}$ ($\omega_{BP} = 1.8ps^{-1}$), but in the EAM systems the difference is much reduced. In both $Cu_{20}Pd_{80}$ and $Cu_{50}Pd_{50}$ cases, and contrary to the typical results obtained in the LJ systems, the longitudinal IR limit is very close to the position of the BP while the transverse IR limit is found well below. Assuming an scheme where the increase of damping is originated by the coupling of propagating modes with the vibrational localized states forming the BP, this would indicate that the EAM potential increases the interaction between the longitudinal modes

and the BP excess states. This result may indicate that the excess of vibrational states has a less transverse nature in the EAM systems. However, taking into account the different Poisson's ratio of the different systems ($\nu = 0.40$, $\nu = 0.37$ and $\nu = 0.35$ for the LJ, $Cu_{20}Pd_{80}$ and $Cu_{50}Pd_{50}$ respectively), it is also possible that an increase of rigidity promotes the coupling between localized modes with shear nature and longitudinal acoustic waves.

Comparing with experimental IXS results [50, 42, 88, 44, 46], the simulated glasses show clear differences with the $Ni_{33}Zr_{67}$ of reference [46] and $Pd_{77}Si_{16.5}Cu_{6.5}$ of reference [50]. In both cases, the IR limit of the longitudinal polarization was clear above the BP frequency, in accordance with the LJ simulations of the previous section or the ones shown in reference [44]. In this sense, we should take into account that the quenching rate of the simulations (10^{12}K/s) is unphysically very much higher than the ultra-fast quenching rates (10^{6}K/s) achieved when producing the glassy metallic ribbons. However, from the results of the simulations it seems clear that the longitudinal IR-limit moves closer to the BP region for more rigid glasses (or glasses coming from stronger liquids) which is in contradiction with some experimental results in metallic glasses but in accordance to some proposed models [43].

Additionally, it can be observed some effect of the box size. By increasing the size of the box, ω_{IR} decreases although the changes are not significant. The reason for increasing the box size is to access lower wavevectors, allowing a better determination of the Ioffe-Regel limit. Finally, the ω_{IR} decreases slightly when applying faster quenching rates. This decrease of ω_{IR} when increasing the quenching rate may explain the lower IR-limit frequencies (relative to the BP position) found in the EAM simulations respect to the experimental measurements of real metallic glasses.

The sound phase velocity can be obtained from the slope of the linear dispersion at low wavevectors. Figure 5.50 shows the values for the longitudinal and transverse sound velocities, respectively, for a EAM $Cu_{20}Pd_{80}$ binary system of $4 \cdot 10^6$ atoms obtained with a cooling rate $\eta_2 = 10^{12}\,[K/s]$. Figure 5.51, shows the same results for a system obtained with the same procedure but reducing Pd constant, $Cu_{50}Pd_{50}$. The sound velocities for the $Cu_{20}Pd_{80}$ system are $c_{L-Cu_{20}Pd_{80}} \sim 3.28km/s$ and $c_{T-Cu_{20}Pd_{80}} \sim 1.50km/s$ and the ones for the $Cu_{50}Pd_{50}$ are $c_{L-Cu_{50}Pd_{50}} \sim 5.34km/s$ and $c_{T-Cu_{50}Pd_{50}} \sim 2.56km/s$. The increase on the velocity when reducing the amount of Pd is logical. The lower content on heavier elements induces a reduction in density without a noticeable change in the elastic constants, and a consequent increase in the sound speed. Moreover, these values are compatible with that obtained in experiments for a metallic glass $Pd_{77}Si_{16.5}Cu_{6.5}$ where the longitudinal sound speed was found to be $c_{L-Pd_{77}Si_{16.5}Cu_{6.5}} \sim 4.5km/s$ [50]. $Pd_{77}Si_{16.5}Cu_{6.5}$, contains a similar percentage of Pd, but most of the Cu is substituted by Si, lighter than Cu. This should result in an increase on the sound speed, as found experimentally. It must be noted that only the longitudinal sound speed can be measured experimentally [50]. Furthermore these results are in agreement with the ones obtained by N. Jaksee [42] studying the amorphous $Cu_{50}Zr_{50}$ alloy, $c_{L-Cu_{50}Zr_{50}} \sim 5.08km/s$ and $c_{T-Cu_{50}Zr_{50}} \sim 2.15km/s$.

At increasing q values the dispersion curve exhibits a bending approaching the first pseudo-Brilloun zone, $q_m/2$, where q_m is the position of the maximum of the $S(q)$ indicating that the acoustic excitations are not well described by propagating plane-waves anymore. This bending occurs for $Cu_{20}Pd_{80}$ the sys-

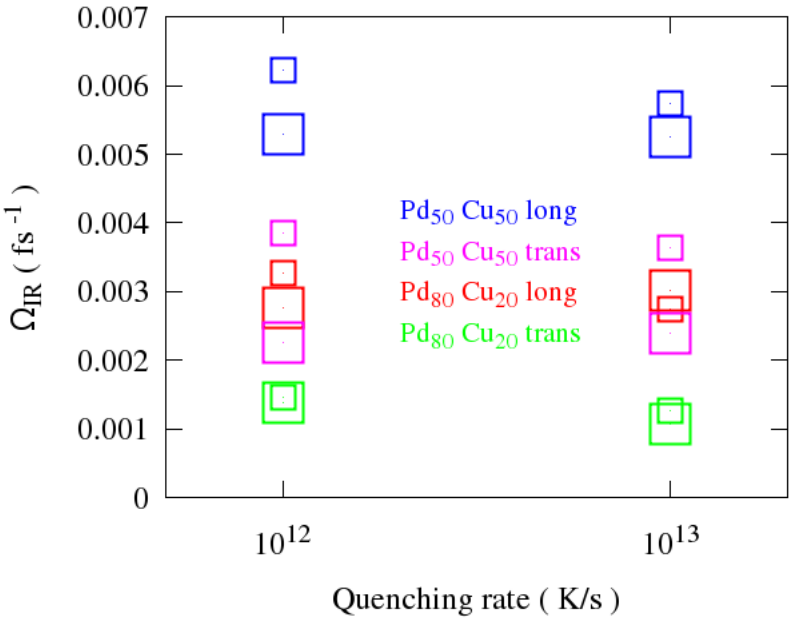

Figure 5.49: Ioffe-Regel limit wavelength versus quenching rate for longitudinal and transverse phonons, determined in simulation boxes of different sizes and different compositions. Systems have different sizes ($3 \cdot 10^4$ atoms and $4 \cdot 10^6$ indicated by the size of the corresponding symbol).

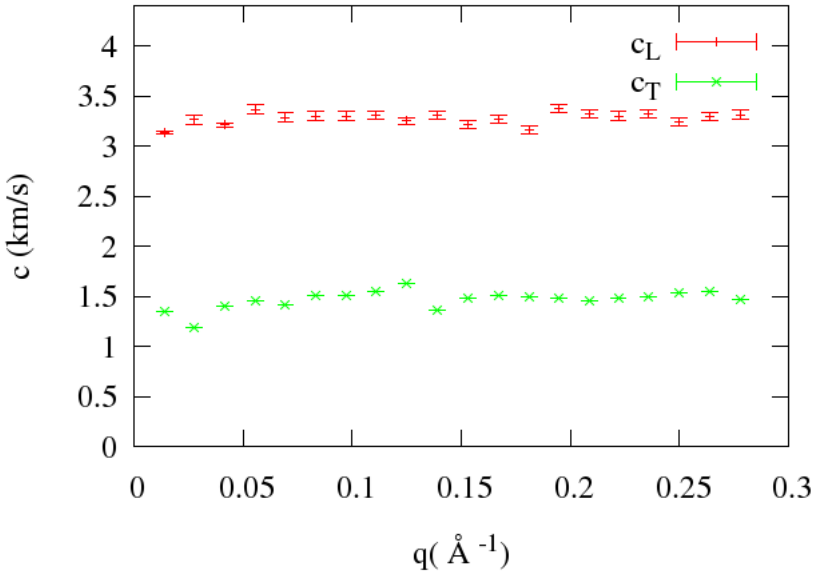

Figure 5.50: Apparent longitudinal and transverse phase velocity as a function of moment transfer q for a EAM $Cu_{20}Pd_{80}$ binary system of $4 \cdot 10^6$ atoms obtained with a quenching rate η_1.

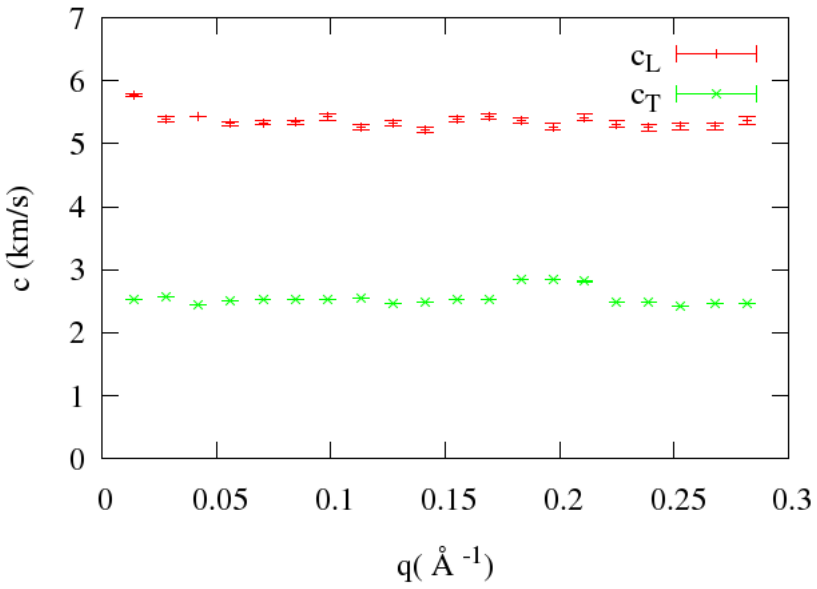

Figure 5.51: Apparent longitudinal and transverse phase velocity as a function of moment transfer q for a EAM $Cu_{50}Pd_{50}$ binary system of $4 \cdot 10^6$ atoms obtained with a quenching rate η_2.

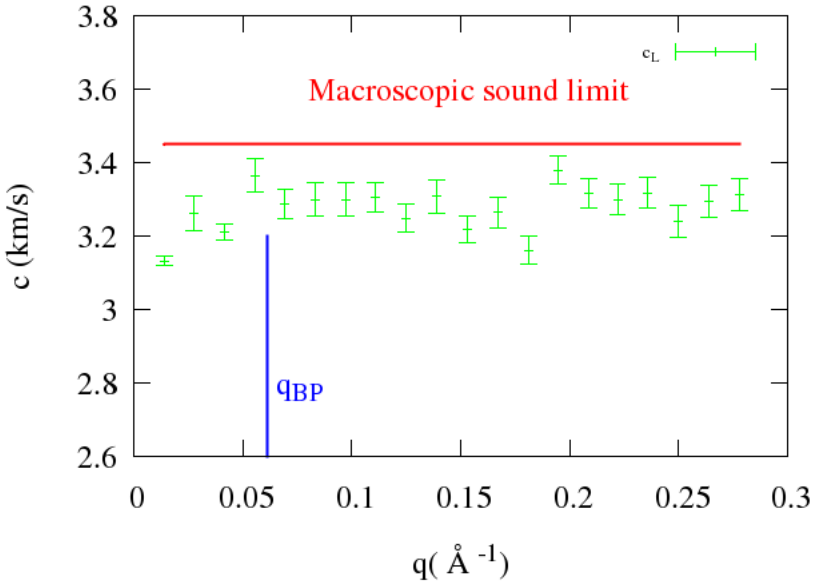

Figure 5.52: Apparent longitudinal phase velocity as a function of moment transfer q, q_{BP} and Macroscopic sound limit in a EAM $Cu_{50}Pd_{50}$ binary system of $4 \cdot 10^6$ atoms obtained with a quenching rate η_2.

tem at $0.45A^{-1}$. A value that is in perfect agreement with the one obtained in experiments, $0.44A^{-1}$ [50]. In the case of the system $Cu_{50}Pd_{50}$ this bending occurs at higher frequencies, $0.6A^{-1}$, due to their higher sound speed.

Although in all the studied systems the macroscopic sound limit has a similar value for all the $Cu_{20}Pd_{80}$ and all the $Cu_{50}Pd_{50}$ metallic glasses, applying different quenching rates and changing the box size slightly modifies the values.

By increasing the size of the studied systems there is a reduction on the sound speed in all the cases. Moreover, applying different quenching rate diverse glassy states and different sound speeds are obtained. By decreasing the quenching rate the sound speed increases slightly. This is coherent with the increase on the density of the material and its rigidity. This behavior was already observed on Lennard-Jones metallic glasses

The sound attenuation changes his behavior as a function of the momentum transfer. For high wave-vectors it follows a linear dependence that becomes stronger to a quadratic law, for low wave-vectors, see Figure 5.53

5.3.5 Viscosity

The shear viscosity is calculated for an EAM $Cu_{20}Pd_{80}$ binary system of 32000 atoms quenched at different temperatures with a cooling rate $\eta_1 = 10^{13}\,[K/s]$.

After studying of the influence of the box size on the results and the computational cost, this system was chosen for being optimal.

Viscosity is calculated for seven different temperatures in the range of 2000k and T_g (1898k, 1694k, 1581k, 1450k, 1354k, 1184k and 1048k) by studying the

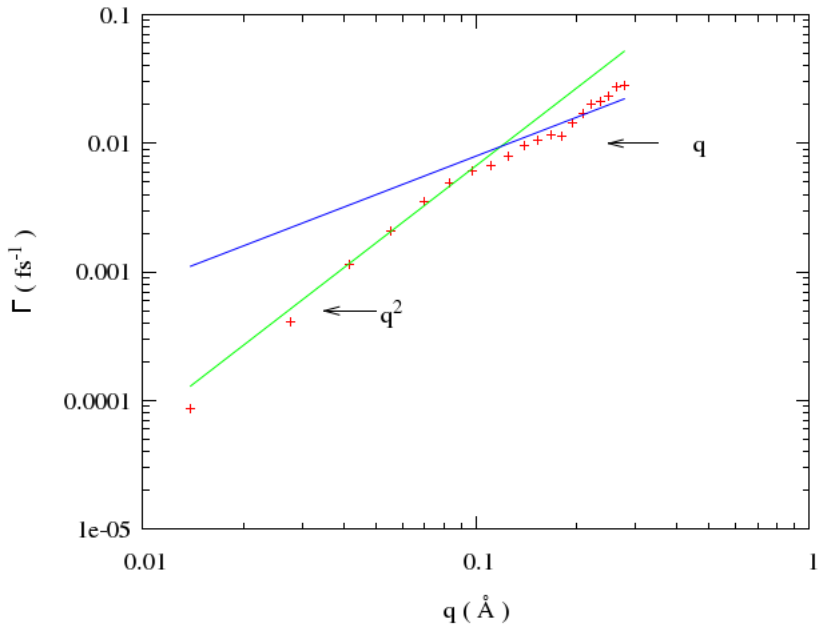

Figure 5.53: q-dependence of the acoustic excitations for the longitudinal of EAM $Cu_{20}Pd_{80}$ binary system of $4 \cdot 10^6$ atoms at equilibrium, after quenching at a cooling rate η_2.

stress auto-correlation function.

Figure 5.54 shows Angell plot fitted by Vogel Fulcher Tammann equation. From this fitting the values for η_0, A and T_0 can be obtained, and consequently the values for the fragility. In this case, the fragility has a value $m = 344$ obtained with a defined $T_g = 739.73K$. The value for the fragility is smaller than the one calculated for the Lennard-Jones system, as expected, due to high fragility of Lennard-Jones systems not reproduced by using more realistic potentials.

This value slightly smaller than the fragility for the Morse system indicates a good concordance. Moreover, the glass transition temperature T_g has a theoretical value higher than the theoretical one obtained for the Morse systems, $T_g = 628K$ and higher than those obtained experimentally. This fact is related with the difference on the quenching rates used in simulations and experiments

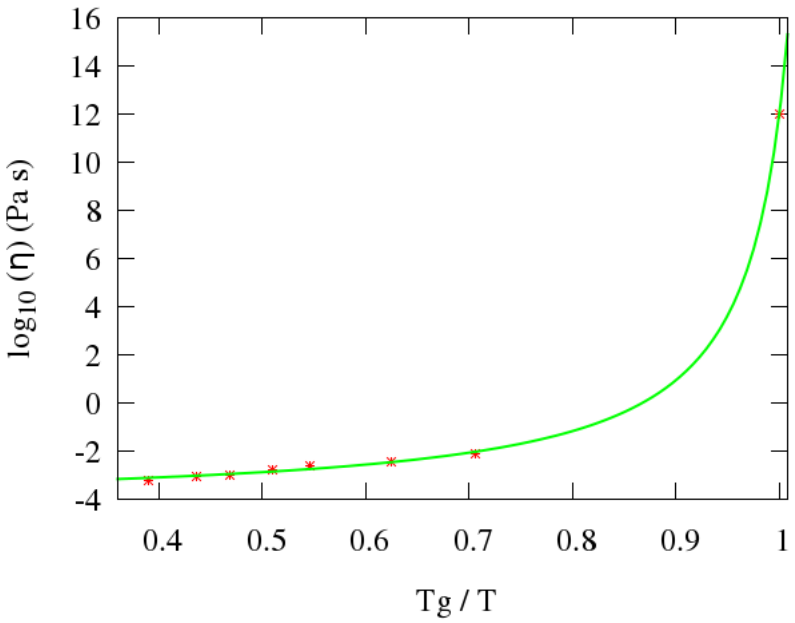

Figure 5.54: Angell plot for a binary EAM $Cu_{20}Pd_{80}$ binary system of 32000 atoms and quenching rate η_2.

Chapter 6

Discussion

The results presented in the previous section permits to analyze the influence of relaxation state, type of inter-atomic bonding and composition on the vibrational dynamics of glasses. Some analysis of the results was performed in the previous chapter, here we will extend such analysis, we will discuss the validity of the results as models of real metallic glasses and we will remark some features of the systems from a global point of view.

All the simulated binary systems showed an amorphous structure, as expected because of the high quenching rates used along the simulation. The most remarkable difference comes from the structure of the Pair correlation function. The Lennard-Jones shows a main peak with a visible substructure, Figure 5.3, associated to the different inter-atomic distances between AA, AB and BB atoms. On the contrary, both the Morse, Figure 5.24, and EAM, Figure 5.38, show a single peaked PCF. This fact is due to the different ratio between the equilibrium distances of both species in the Lennard-Jones (0.833) and the Cu/Pd radius ratio (0.927) used in the Morse and EAM systems. That is, the Lennard-Jones species have much more dissimilar radius than Cu and Pd, and thus it is likely that the atomic environments are more differentiated in the Lennard-Jones system than in the Cu-Pd system.

The Morse potential produces a very compact glass structure coming from a glass transition at 628K, this is close to the T_g of the real material measured at 20K/min but much lower than the glass transition temperature expected for a quenching rate of 10^{13}K/s. The structure factor obtained from the Morse simulations shows the first peak at $q = 3.45\text{Å}^{-1}$, which is much more higher than the one obtained in similar real materials like $Pd_{77}Si_{16.5}Cu_{6.5}$ glass ($q \sim 2.7\text{Å}^{-1}$). On the contrary, the EAM potential produces lower density structures. The maximum of the $S(q)$ is found at $q = 2.5\text{Å}^{-1}$, corresponding to a glassy structure more similar to the one expected in a Pd-based metallic glass.

Despite the very different glass structures resulting form the Morse and EAM potentials, the similarity of the vibrational properties obtained in the $Cu_{20}Pd_{80}$ system is worth to mention. The shape of the VDOS and the sound velocities are qualitatively comparable thus showing a strong dependence of the atomic masses and the strength of the inter-atomic bonds and a smaller influence of the particular glassy structure. There is no doubt that EAM potentials have a well settled physical background, and Morse potentials are not so commonly used

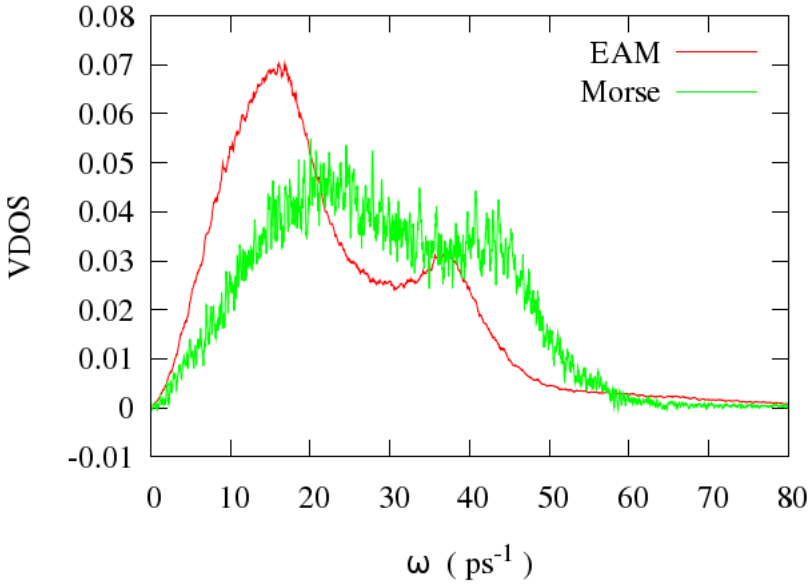

Figure 6.1: Representative vibrational densities of states of systems $Cu_{20}Pd_{80}$ simulated with Morse and EAM potentials.

in the literature in the simulation of amorphous materials. However, Lennard-Jones potentials have been extensively used as a model systems in the study of glassy materials, including metallic glasses. It is commonly argued that Lennard-Jones potentials are much less computationally costly than realistic potentials such as EAM. Our results show, however, that a potential such as the Morse potential, with spherical symmetry and as mathematically simple as the Lennard-Jones potential, gives a much closer description of the dynamical behaviour of glasses, at least metallic glasses.

The main purpose of this work was the study of the vibrational properties of metallic glasses. The comparison of the vibrational density of states between Lennard-Jones systems and Cu-Pd systems shows noticeable differences. The VDOS of LJ systems is single peaked, Figure 5.7 , while the VDOS of the Cu-Pd glass is doubly peaked, see Figure 6.1. The different position of the maxima in this case is directly linked to the differences observed in the pair correlation function.

It is tempting to thing that the two peaks are associated to the two kinds of atoms, heavier atoms moving at lower frequencies than lighter ones. However, the ratio of masses in the LJ system is 2, while in the Cu-Pd is ~ 1.68; the secondary peak appears precisely when the ratio of masses is decreased. Thus, we consider that the vibrational states are more related to the features of the interatomic potential. The Lennard-Jones potential has a long tail, the elastic constant being weaker than in the Cu-Pd system at increasing interatomic distances. This may allow a more uncoupled movement between neighbouring atoms, specially in relation to shearing forces. On the contrary, the Morse potential is a more bounding potential, inducing a higher correlation between

neighbour atoms. Shearing forces will be more effective in transmitting vibrations three dimensionally. This is even more evident in the case of the EAM potentials, which introduce an indirect many-body interaction. Thus, we think that the phononic spectra of the Pd-Cu is more complex than in the LJ system, and phonons are of mixed type, longitudinal-transverse, as it is common in amorphous materials. .

It is worth to mention that, although the main physical results are quite similar in small and large systems, the quality of the computed quantities increases with the size of the simulation box. The noise observed in a simulation with 32000 atoms, Figure 5.27 reduces substantially when the system size increases to 10^6 atoms, Figure 5.7, and even more to $4 \cdot 10^6$ atoms, Figure 5.41. This fact is common in the computation of all the dynamical properties of the simulated systems, contrary to the computation of the static properties such as the PCF and the Static structure factor.

The Debye frequency and the corresponding Debye level was calculated for all the studied systems, showing a consistent behaviour. In most of the studied cases the Debye level increases slightly by increasing the number of the atoms. Given that large systems are expected to be closer to the actual material behaviour, this fact indicates that small-size simulations always underestimate the value of the Debye level. Furthermore, the Debye level increases as the quenching rate increases. When applying slower quenching rates, systems with higher density and less free volume are obtained. This increase on the density of the glass usually increases the value of the Debye frequency ω_D, leading to smaller values for the Debye level.

The composition of the system also influences the Debye level. In particular, the Debye level reduces noticeably when the amount of the heavy Pd atoms is reduced. In the case of the $Cu_{20}Pd_{80}$ systems the values obtained by using the EAM potentials are in concordance with those obtained in Morse system. Moreover, the values obtained in this work are in qualitative agreement with those obtained experimentally in glasses with comparable composition, although the quenching rates are several orders the magnitude faster in simulations than in the laboratory.

One of the particular features of glasses related with vibrational properties is the Boson Peak. The Boson Peak reflects an enhancement of states in the low frequency regime of the Vibrational Density of States and is believed to be the key to the fundamental understanding of the vibrational properties in metallic glasses. For this reason an extended study for different systems, samples and using different potentials was performed.

The Boson Peak designates an excess over the Debye level in the vibrational density of states at low frequencies. Figure 6.2 shows the comparison betwen the Boson Peak as simulated using Morse and EAM potentials. As expected, the Debye level of the Morse (denser) system appears below that of the EAM system (lighter). The Boson Peak appears at larger frequencies in the Morse system, but with lower intensity.

In this work we observed that the position and intensity of the Boson peak are slightly affected by the size effects. However, the Boson peak intensity is higher in systems obtained with higher quenching rates and their position shifts slightly to smaller frequencies. This effect is probably due to the increase of the elastic constants of more relaxed systems obtained by lower quenching rates. These results are in agreement with those obtained by Bauchy on the study of

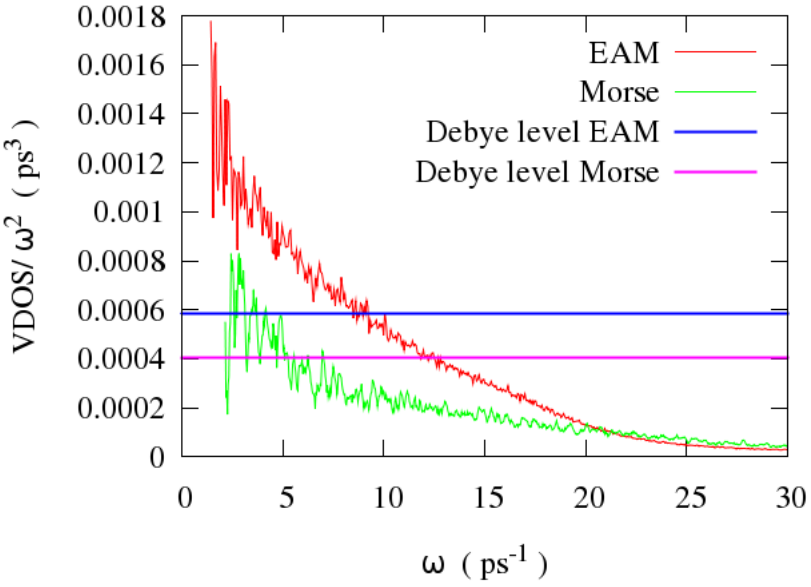

Figure 6.2: Representative intensity of the ratio between the density of states and the frequency squared in systems $Cu_{20}Pd_{80}$ simulated with Morse and EAM potentials.

densified silicates using MD in small systems [57]. Moreover, similar results were observed experimentally in different systems as pure silica [58], lithium silicate glass, $Na_2FeSi_3O_8$ glass [60], as well as in different polymers [61]. In the case of the system studied experimentally, $Pd_{77}Si_{16.5}Cu_{6.5}$ the BP was found at $3,6 \cdot 10meV$[50], see Figure 6.3 (right). These are in qualitative agreement with those obtained in $Cu_{20}Pd_{80}$, shown in Figure 6.3 (left). The values for the BP position obtained in our simulations for $Cu_{20}Pd_{80}$ are $1,3meV$ by using EAM potentials and $2,1meV$ using Morse potentials, respectively. In the case of the $Cu_{50}Pd_{50}$ the BP is observed around $5meV$. This indicates that the wavenumber of the BP decreases as the mass ratio between the heavier and the lighter atom increases. Thus, the difference found between the experimental value in $Pd_{77}Si_{16.5}Cu_{6.5}$ and the computed value in $Cu_{20}Pd_{80}$ may be due to the Si content, Si being much lighter than Cu.

The dynamic structure factor, $S(q,\omega)$ provided us information about the behavior of acoustic excitations. The access to lower frequencies is limited by the box size, for this reason multimillion atoms systems were studied.

It was observed that in all the cases that the width of the peak, $\Gamma_{L,T}(q)$, of the longitudinal and transverse phonons increases and the characteristic frequency, $\Omega_{L,T}(q)$, is shifted to higher frequencies as the wave-vector increases in $S(q,\omega)$. By fitting the characteristic frequency the dispersion relation was built. For all the studied systems a linear region at low q numbers was observed and a bending when approaching the limit of the first pseudo-Brillouin zone $q_m/2$, where q_m is the position of the maximum of the static structure factor $S(q)$ as shown in Figure 6.4. From this data, the apparent sound speed was computed,

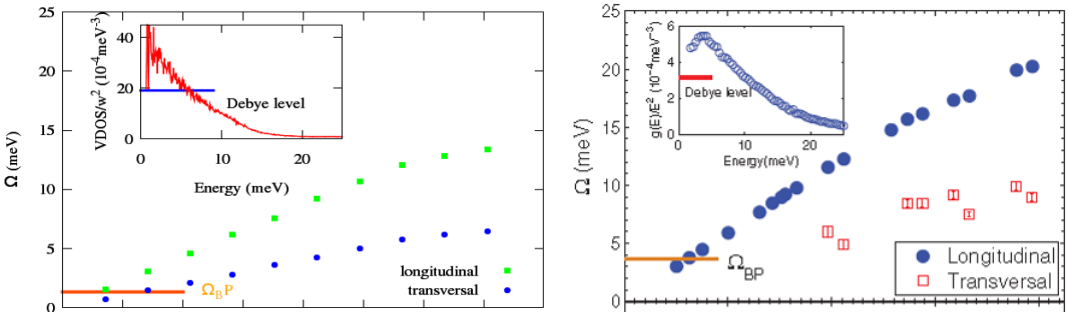

Figure 6.3: Left: Dispersion relationship in $Cu_{20}Pd_{80}$ simulated with EAM potentials. Inset: reduced vibrational density of states. Right: Dispersion relationship in $Pd_{77}Si_{16.5}Cu_{6.5}$ measured experimentally by Inelastic X-Ray scattering. Inset: reduced vibrational density of states.

and it is shown in Figure 6.5 right. The results obtained are very similar to those obtained experimentally[50], see Figure 6.5 (right).

From the relation dispersion the Ioffe-Regel limit was computed. The ω_{IR}^{L} is found at frequencies higher than the Boson peak frequency (ω_{BP}) ($\omega_{IR}^{L} > \omega_{BP}$) for all the cases, although the difference in EAM systems is much reduced.

In the case of the LJ systems ω_{IR}^{T} has values closer to ω_{BP} than in the $CuPd$ system. It has been proposed that the excess modes generating the BP corresponds to transverse localized vibrational modes generated by some kind of defective configurations of the glass structure. These localized modes strongly couple with the propagating transverse excitations and govern their damping and dissipation [101], an so on $\omega_{IR}^{T} \simeq \omega_{BP}$. Although the IXS technique is limited to the study of the longitudinal excitations, it is expected that the same features, $\omega_{IR}^{T} \simeq \omega_{BP}$ and $\omega_{IR}^{L} > \omega_{BP}$, will hold in $Pd_{77}Si_{16.5}Cu_{6.5}$ glass due to the ratio between shear and bulk modulus of the material.

The difference between ω_{IR}^{L} and ω_{BP}, in EAM systems is much reduced. In both $Cu_{20}Pd_{80}$ and $Cu_{50}Pd_{50}$ cases, and contrary to the typical results obtained in the LJ systems, the longitudinal IR limit is very close to the position of the BP while the transverse IR limit is found well below. This may indicate that the EAM potential increases the interaction between the longitudinal modes and the BP excess states.

This result is in agreement with the results obtained experimentally in the longitudinal case[50], see Figure 6.4. In the case of the ω_{IR}^{T} different behaviours were observed for the potentials studied. In the case of LJ systems the ω_{IR}^{T} is found to be nearer to ω_{BP} than in other cases. Comparing with experimental IXS results [50, 42, 88, 44, 46], the simulated glasses show clear differences with the $Ni_{33}Zr_{67}$ of reference [46] and $Pd_{77}Si_{16.5}Cu_{6.5}$ of reference [50].

It is necessary to take into account that the quenching rate of the simulations (10^{12}K/s) is unphysically very much higher Thant the ultra-fast quenching rates (10^{6}K/s) achieved when producing the glassy metallic ribbons. However, from the results of the simulations it seems clear that the longitudinal IR-limit moves closer to the BP region for more rigid glasses (or glasses coming from stronger liquids).

In order to access lower wave vectors systems with different sizes were stud-

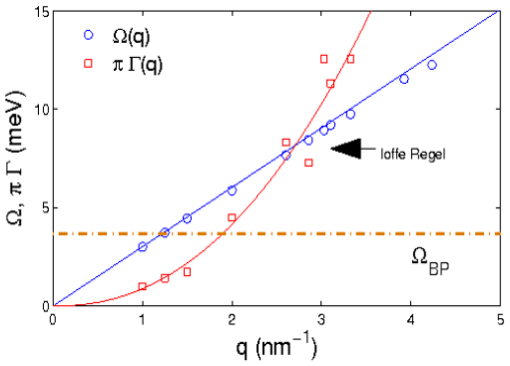

Figure 6.4: Experimental dispersion relationship obtained from IXS measurements in $Pd_{77}Si_{16.5}Cu_{6.5}$.

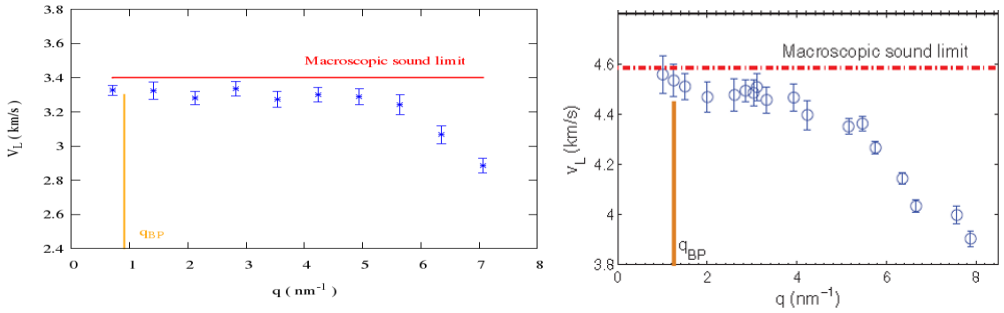

Figure 6.5: Left: apparent sound speed in $Cu_{20}Pd_{80}$ simulated with EAM potentials. Right: Apparent sound speed in $Pd_{77}Si_{16.5}Cu_{6.5}$, computed from IXS.

ied. It was observed that by increasing the size of the box, ω_{IR} decreases although the changes are not significant. Finally, the ω_{IR} decreases slightly when applying faster quenching rates. This decrease of ω_{IR} when increasing the quenching rate may explain the lower IR-limit frequencies (relative to the BP position) found in the EAM simulations respect to the experimental measurements of real metallic glasses.

The apparent sound phase velocity was calculated for all the systems from the slope of the linear region of the dispersion relationship at low q-vectors. In the case of the Lennard-Jones systems we obtain values of $10\sigma\tau^{-1}$ and $4.2\sigma\tau^{-1}$ for the longitudinal and transverse the sound phase velocity, respectively. In the case of Morse potential the sound phase velocity has values of$\sim$ $3.4km/s$ and $\sim$ $1.3km/s$ in $Cu_{20}Pd_{80}$. Using more realistic potentials, the sound velocities for the $Cu_{20}Pd_{80}$ system are $c_{L-Cu_{20}Pd_{80}} \sim 3.28km/s$ and $c_{T-Cu_{20}Pd_{80}} \sim 1.50km/s$ while for $Cu_{50}Pd_{50}$ are $c_{L-Cu_{50}Pd_{50}} \sim 5.34km/s$ and $c_{T-Cu_{50}Pd_{50}} \sim 2.56km/s$. It is observed an increase on the velocity when reducing the amount of Pd due to the reduction in density without a noticeable change in the elastic constants, and a consequent increase in the sound speed.

The values obtained in EAM systems are compatible with that obtained in experiments for a metallic glass $Pd_{77}Si_{16.5}Cu_{6.5}$ where the longitudinal sound speed was found to be $c_{L-Pd_{77}Si_{16.5}Cu_{6.5}} \sim 4.5km/s$[50]. $Pd_{77}Si_{16.5}Cu_{6.5}$, contains a similar percentage of Pd, but most of the Cu is substituted by Si, lighter than Cu. This should result in an increase on the sound speed, as found experimentally. It must be noted that only the longitudinal sound speed can be measured experimentally[50]. Furthermore these results are in agreement with the ones obtained by N. Jaksee [42] studying the amorphous $Cu_{50}Zr_{50}$ alloy, $c_{L-Cu_{50}Zr_{50}} \sim 5.08km/s$ and $c_{T-Cu_{50}Zr_{50}} \sim 2.15km/s$.

The sound velocity is affected by the quenching rate. Different quenching rate lead to diverse glassy states with different overall properties. By decreasing the quenching rate the sound speed increases slightly. This is coherent with the reduction of the free volume and the increase in the rigidity of the material. For low q values the determined sound speeds are almost independent of the box size, while for larger values small boxes give systematically larger values than larger boxes.

At small q it is observed a softening of the apparent sound velocity. This softening was already observed in a monoatomic Lennard-Jones glass $q < 0.27\sigma^{-1}$ and it was showed that this regime is accompanied by strong scattering with $\Gamma(q) \propto q^4$. It was proposed [88, 7] that this softening is originated by a Rayleigh-like scattering of sound waves by the elastic fluctuations in the media. This reduction of the apparent sound velocity was already observed in experimental results and also in monoatomic LJ glasses [88, 50].

Finally, moving to higher frequencies the dispersion curve exhibits a bending approaching the pseudo Brillouin zone, $q_m/2$. This bending occurs for $Cu_{20}Pd_{80}$ the system at $0.45A^{-1}$. A value that is in perfect agreement with the one obtained in experiments, $0.44A^{-1}$[50]. In the case of the system $Cu_{50}Pd_{50}$ this bending occurs at higher frequencies, $0.6A^{-1}$, due to their higher sound speed.

The fragility of the studied systems was obtained by calculating the viscosity at different temperatures. The values for the fragility in the LJ systems is $m = 1316$, in Morse systems is $m = 324$ and in the case of the EAM systems is $m = 344$. As expected LJ fragility is much higher than that of EAM and Morse systems, due that Lennard-Jones are highly fragile systems. Even in the case of the use of more realistic potentials the value for the fragility is higher than the ones obtained experimentally. The reason might be related to the extremely high quenching rates used in simulations, as it is known experimentally that fragility increases with the quenching rate.

A final comment will be made on the computational costs of the simulations. All simulations were performed by using the moldyPSI code [83], parallelized with MPI. Small size systems, up to 10^5 atoms were simulated in a personal workstation with 8 processors, but larger systems were performed at the facilities of the Barcelona Supercomputing Center [84] using up to 512 processors. Most of the computing time was needed for the quenching procedure and subsequent equilibration below the glass transition temperature. The computation of the dynamical properties required comparatively much less computing time. However, the use of large systems was needed to reduce substantially the noise in the computation of the dynamical properties.

Conclusions

The macroscopic mechanical properties of a material are intimately linked to its atomic structure. In particular, the fracture behavior of brittle materials, is initiated by the generation of vibrational modes. In materials with periodic structure, this vibrational states can be easily defined as quantized plane wave phonons. In metallic glasses, where the structure appears to be amorphous, the vibrational spectrum has different, specific features.

In this work, the vibrational properties of metallic glasses were examined by molecular dynamics simulations. The study was focused in binary systems simulated using three different interatomic potentials: Lennard-Jones, Morse and Embedded atom (EAM). Systems of different sizes, up to several millions of atoms, were simulated. In all cases the ratio of masses of both species was high, namely 2 in Lennard-Jones potentials and 1.67 in Morse and EAM potentials. The purpose was to simulate Pd-based metallic glasses, where the mass ratio between difference between the composing species is also high.

Well equilibrated systems were obtained by quench from a melt at high temperature, followed by a simulated quench through the glass transition and subsequent equilibration at constant temperature in the glass state.

The amorphous structure of the simulated materials was checked by computing the the Pair correlation function and the Static structure factor S(q). The static structure factor showed no sharp peaks for any of the system indicating no crystallization.

In the case of the PCF, the LJ systems shows a first sharp peak split in three contributions and a second peak-with-shoulder. This structure has been observed previously in hard sphere potentials and metallic glasses. In the case of EAM and Morse systems, this first peak is well defined and no individual contributions can be distinguished. Moreover, it is found that the position of the main peak of both the PCF and the S(q) are not affected by changing the size of the system.

The Vibrational density of states was computed by Fourier transformation of the Velocity autocorrelation function. The VDOS is single-peaked in all Lennard-Jones systems, but shows two peaks in both Morse and EAM systems. We presume that this is due to the higher bonding strength of Morse and EAM potentials, as well as to the mixed transverse-longitudinal nature of phonons in amorphous materials. However, we cannot discriminate between these possible reasons.

The behaviour of the Debye level was also studied. A positive correlation between the Debye level and the box size was found, indicating that small-size simulations always underestimate the value of the Debye level. The Debye level was also found to increase with the quenching rate, as a consequence of the

corresponding density decrease. Finally, there is a compositional dependence on the Debye level, studied in the CuPd system, showing also a positive correlation with the heavier atom; this is also attributed to the density variation. The values obtained in this work are in qualitative agreement with those obtained experimentally in similar glasses.

The so-called Boson peak, which designates an excess over the Debye level in the vibrational density of states at low frequencies in glasses was also extensively observed. The dependence of the Boson peak position and intensity on the system size was found to be weak. On the contrary, the Boson peak intensity increases with the quenching rate, while its position shifts slightly to smaller frequencies. This effect is probably due to the increase of the elastic constants of more relaxed systems obtained by lower quenching rates. The results obtained by using realistic, semiempirical EAM potentials compare well with the experimental data available in glasses of similar compositions.

The dynamic structure factor, $S(q,\omega)$ was also computed in large systems to get information on the behavior of acoustic excitations at low wavenumbers. The dominant frequencies $\Omega_{L,T}(q)$ were computed for each considered wavevector, in order to compute the relation of dispersion of longitudinal and transverse phonons. In all studied cases the width of the peak, $\Gamma_{L,T}(q)$, increases as the frequency increases. For all the systems a linear region at low wavenumbers was observed and a bending when approaching the limit of the first pseudo-Brillouin. This behaviour is the same than that observed experimentally by Inelastic X-Ray scattering.

The macroscopic sound speed was obtained in the limit of wavenumbers tending to zero. The values obtained with EAM and Morse potentials are in qualitative agreement with those obtained experimentally in systems of similar composition.

The Ioffer-Regel limit, where the coherence length of the phonon is similar to the phonon wavelength, was computed. It was found that the Ioffe-Regel frequency decreases slightly when applying faster quenching rates. The longitudinal Ioffe-Regel limit was found at frequencies higher than the Boson peak frequency for all the cases, although the difference in EAM systems is much reduced. In both $Cu_{20}Pd_{80}$ and $Cu_{50}Pd_{50}$ cases, and contrary to the typical results obtained in the LJ systems, the longitudinal IR limit is very close to the position of the BP while the transverse IR limit is found well below. It is inferred that the EAM potential increases the interaction between the longitudinal modes and the BP excess states. There is a large dispersion in the available experimental data but, from the results of the simulations it seems clear that the longitudinal IR-limit moves closer to the BP region for more rigid glasses (or glasses coming from stronger liquids).

Finally the fragility of the studied systems was obtained by calculating the viscosity at different temperatures. Lennard-Jones systems showed a much larger fragility than EAM and Morse systems, as it is known in the literature. However, even systems simulated with more realistic potentials showed fragility values much higher than those obtained experimentally. This is attributed to the extremely high quenching rates used in simulations, as it is known experimentally that fragility increases with the quenching rate.

Appendix A

This appendix includes the results of all the simulated metallic glasses referred in the text.

Lennard-Jones potential

This section presents the results obtained by using a Lennard-Jones potential in systems of 13824, 110592, 1098500, 2048000 and 3764768 atoms obtained with a fast ($\eta_1 = 24.57/500$ $[\varepsilon/(k_B\tau)]$), medium ($\eta_2 = 24.57/5000$ $[\varepsilon/(k_B\tau)]$) and slow ($\eta_3 = 24.57/50000$ $[\varepsilon/(k_B\tau)]$) quenching rate.

Binary systems (80%-20%)

13824 atoms

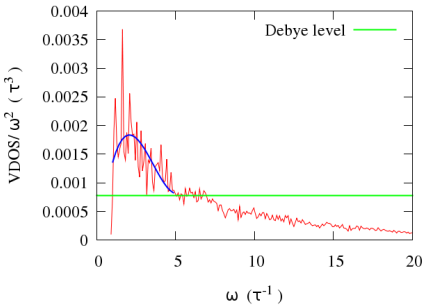

Figure A.1: Boson Peak observed in a Lennar-Jones binary system of 13824 atoms and quenching rate η_1.

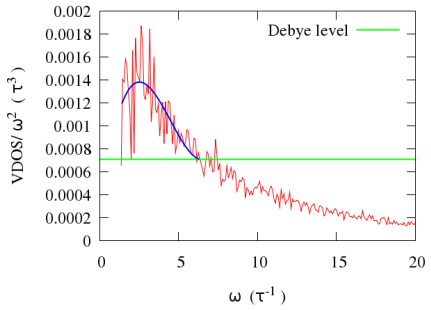

Figure A.2: Boson Peak observed in a Lennar-Jones binary system of 13824 atoms and quenching rate η_2.

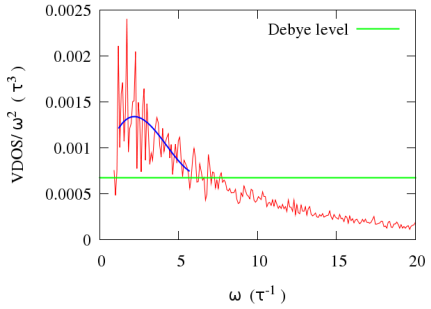

Figure A.3: Boson Peak observed in a Lennar-Jones binary system of 13824 atoms and quenching rate η_3.

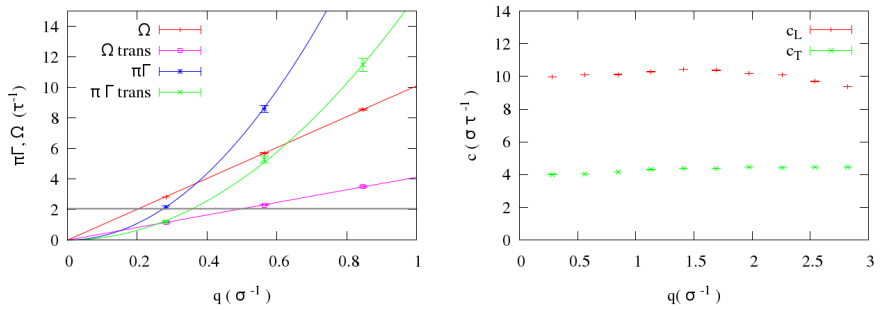

Figure A.4: Dispersion relation curve (left) and apparent phase velocity (right) of Lennar-Jones binary system of 13824 atoms and quenching rate η_1.

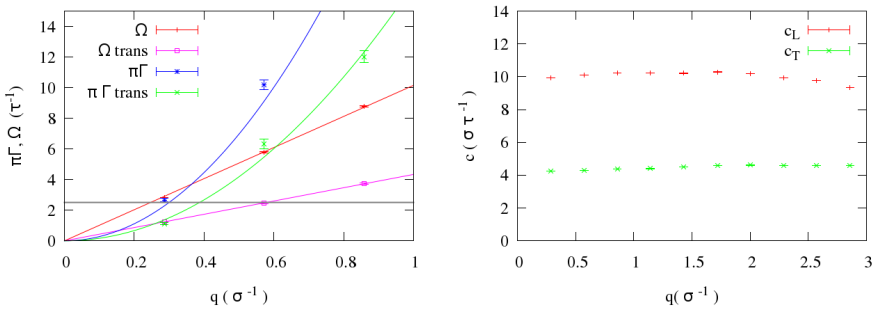

Figure A.5: Dispersion relation curve (left) and apparent phase velocity (right) of Lennar-Jones binary system of 13824 atoms and quenching rate η_2.

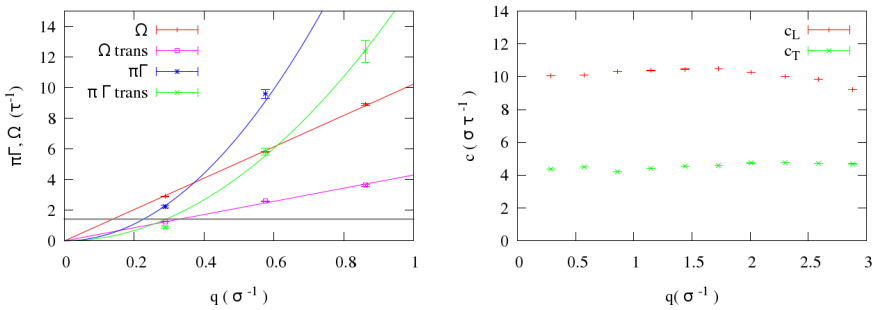

Figure A.6: Dispersion relation curve (left) and apparent phase velocity (right) of Lennar-Jones binary system of 13824 atoms and quenching rate η_3.

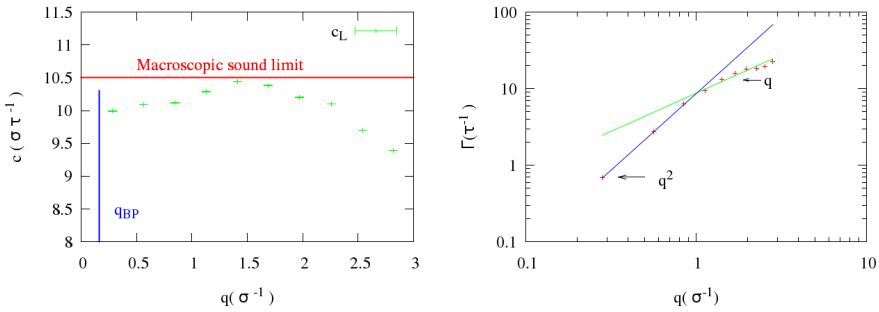

Figure A.7: Apparent longitudinal phase velocity as a function of wave vector q, q_{BP} and Macroscopic sound limit (left) and sound attenuation as a function of wave vector q (right) of Lennar-Jones binary system of 13824 atoms and quenching rate η_1.

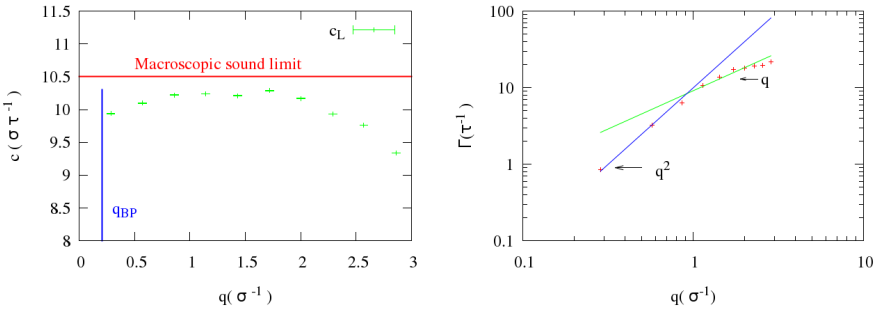

Figure A.8: Apparent longitudinal phase velocity as a function of wave vector q, q_{BP} and Macroscopic sound limit (left) and sound attenuation as a function of wave vector q (right) of Lennar-Jones binary system of 13824 atoms and quenching rate η_2.

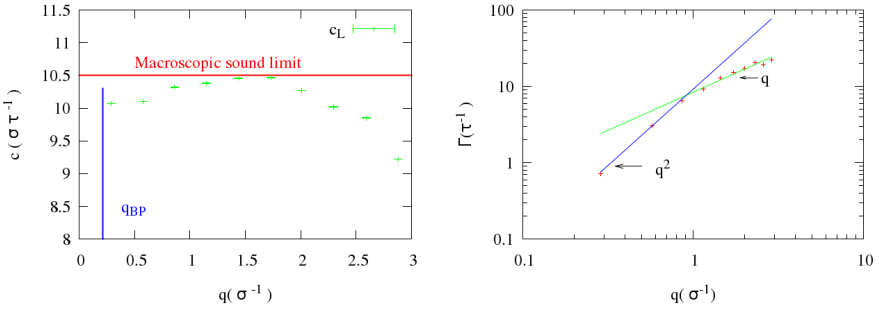

Figure A.9: Apparent longitudinal phase velocity as a function of wave vector q, q_{BP} and Macroscopic sound limit (left) and sound attenuation as a function of wave vector q (right) of Lennar-Jones binary system of 13824 atoms and quenching rate η_1.

110592 atoms

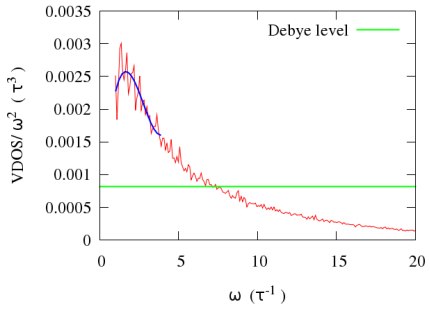

Figure A.10: Boson Peak observed in a Lennar-Jones binary system of 110592 atoms and quenching rate η_1.

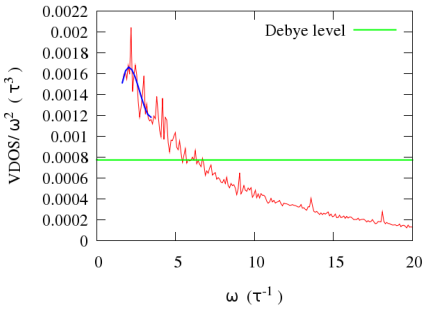

Figure A.11: Boson Peak observed in a Lennar-Jones binary system of 110592 atoms and quenching rate η_2.

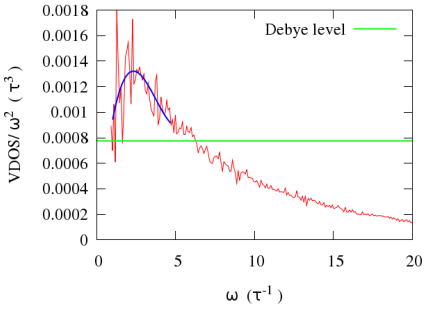

Figure A.12: Boson Peak observed in a Lennar-Jones binary system of 110592 atoms and quenching rate η_3.

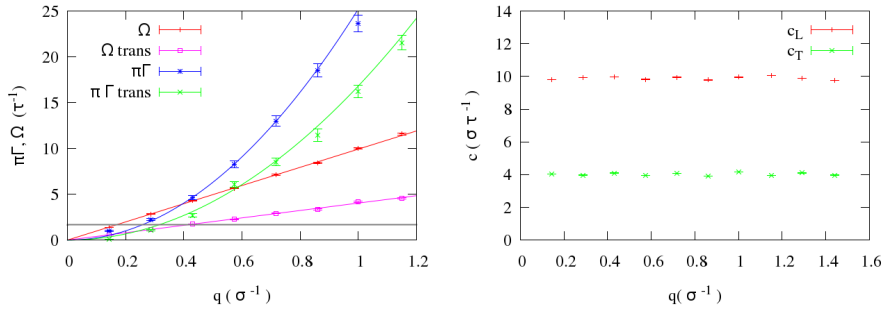

Figure A.13: Dispersion relation curve (left) and apparent phase velocity (right) of Lennar-Jones binary system of 110592 atoms and quenching rate η_1.

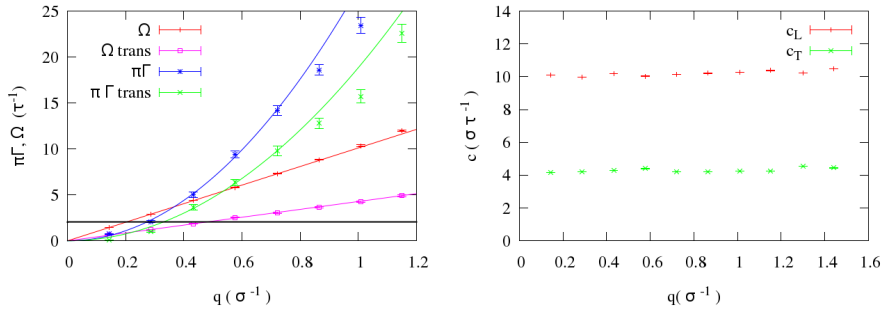

Figure A.14: Dispersion relation curve (left) and apparent phase velocity (right) of Lennar-Jones binary system of 110592 atoms and quenching rate η_2.

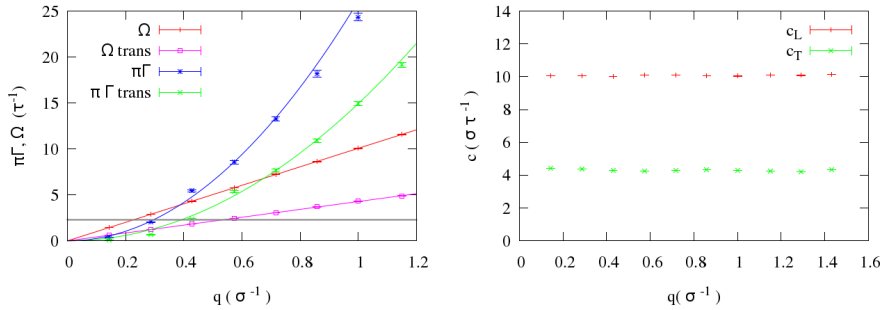

Figure A.15: Dispersion relation curve (left) and apparent sound speed (right) of Lennar-Jones binary system of 110592 atoms and quenching rate η_3.

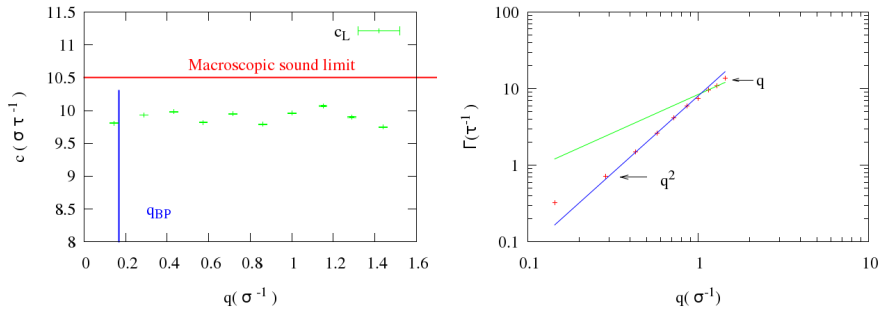

Figure A.16: Apparent longitudinal phase velocity as a function of wave vector q, q_{BP} and Macroscopic sound limit (left) and sound attenuation as a function of wave vector q (right) of Lennar-Jones binary system of 110592 atoms and quenching rate η_1.

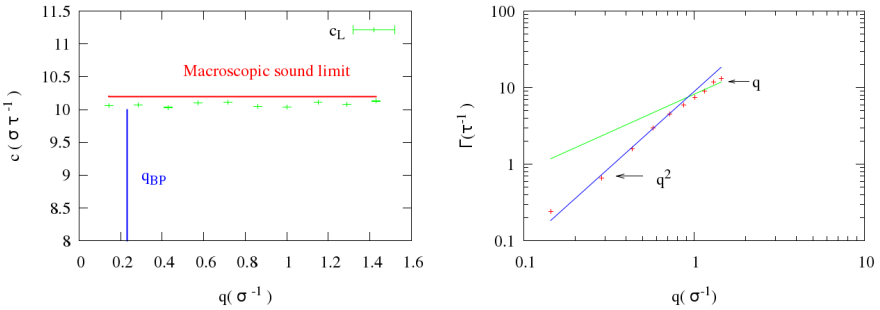

Figure A.17: Apparent longitudinal phase velocity as a function of wave vector q, q_{BP} and Macroscopic sound limit (left) and sound attenuation as a function of wave vector q (right) of Lennar-Jones binary system of 110592 atoms and quenching rate η_2.

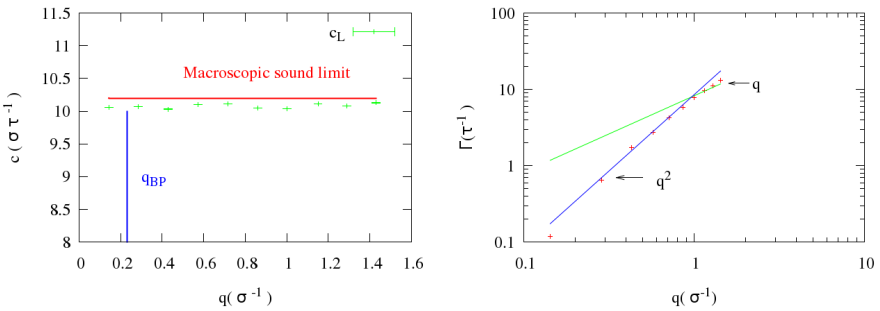

Figure A.18: Apparent longitudinal phase velocity as a function of wave vector q, q_{BP} and Macroscopic sound limit (left) and sound attenuation as a function of wave vector q (right) of Lennar-Jones binary system of 110592 atoms and quenching rate η_3.

1098500 atoms

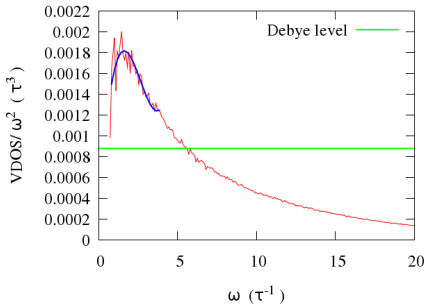

Figure A.19: Boson Peak observed in a Lennar-Jones binary system of 1098500 atoms and quenching rate η_1.

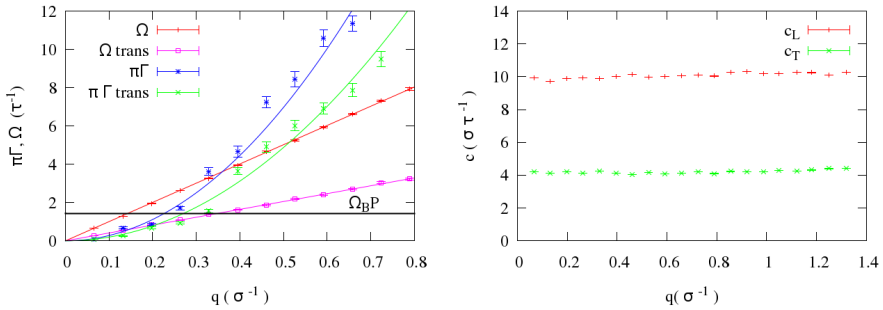

Figure A.21: Dispersion relation curve (left) and apparent phase velocity (right) of Lennar-Jones binary system of 1098500 atoms and quenching rate η_1.

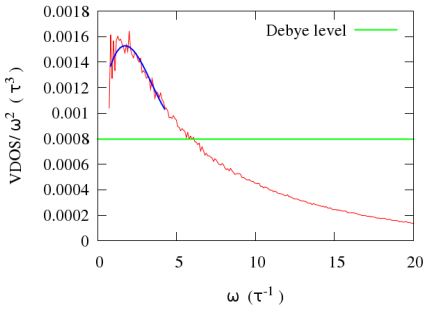

Figure A.20: Boson Peak observed in a Lennar-Jones binary system of 1098500 atoms and quenching rate η_2.

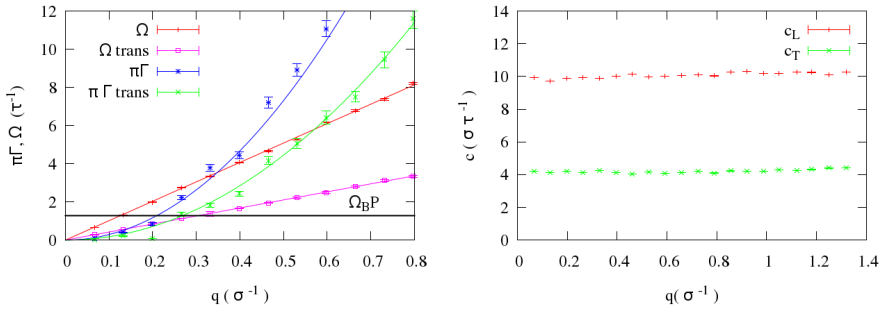

Figure A.22: Dispersion relation curve (left) and apparent phase velocity (right) of Lennar-Jones binary system of 1098500 atoms and quenching rate η_2.

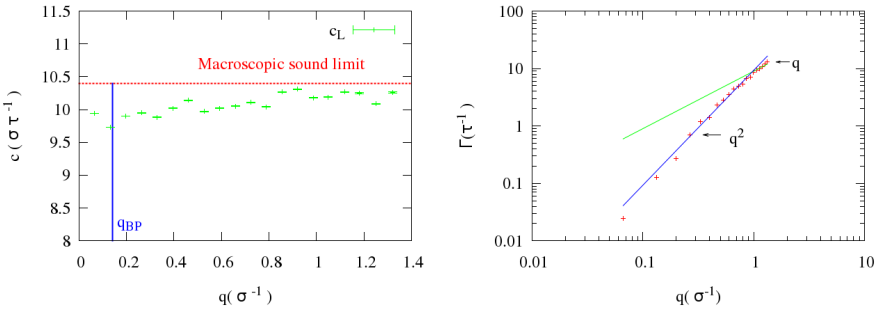

Figure A.23: Apparent longitudinal phase velocity as a function of wave vector q, q_{BP} and Macroscopic sound limit (left) and sound attenuation as a function of wave vector q (right) of Lennar-Jones binary system of 1098500 atoms and quenching rate η_1.

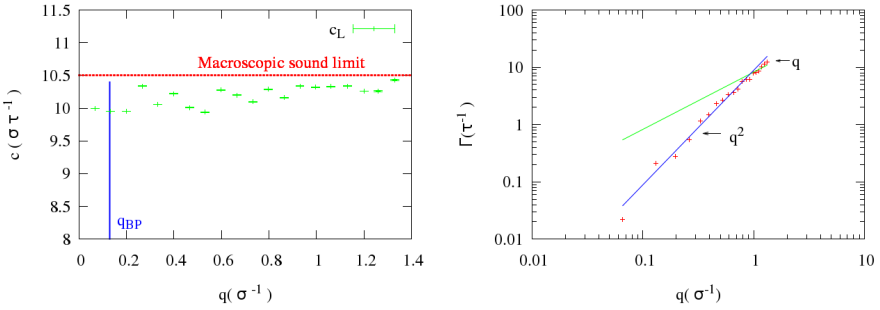

Figure A.24: Apparent longitudinal phase velocity as a function of wave vector q, q_{BP} and Macroscopic sound limit (left) and sound attenuation as a function of wave vector q (right) of Lennar-Jones binary system of 1098500 atoms and quenching rate η_2.

2048000 atoms

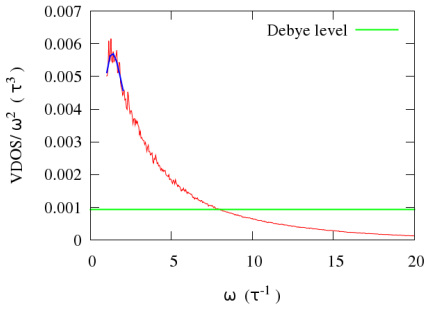

Figure A.25: Boson Peak observed in a Lennar-Jones binary system of 2048000 atoms and quenching rate η_1.

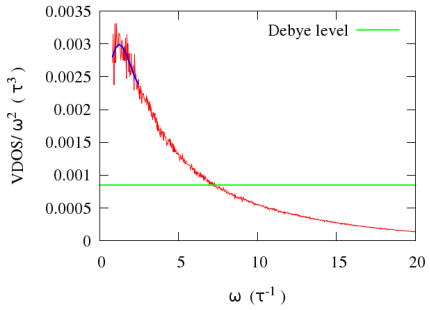

Figure A.26: Boson Peak observed in a Lennar-Jones binary system of 2048000 atoms and quenching rate η_2.

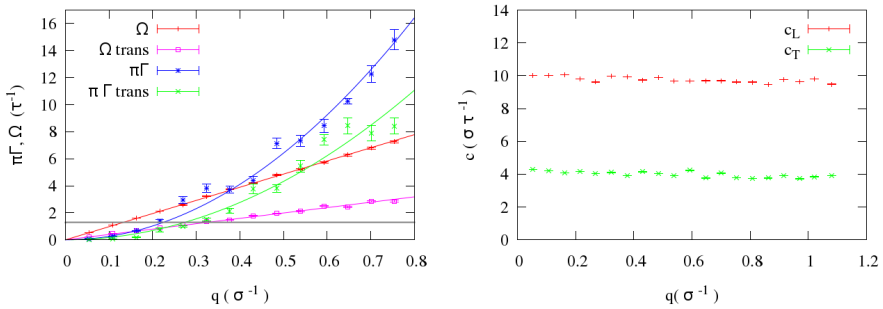

Figure A.27: Dispersion relation curve (left) and apparent phase velocity (right) of Lennar-Jones binary system of 2048000 atoms and quenching rate η_1.

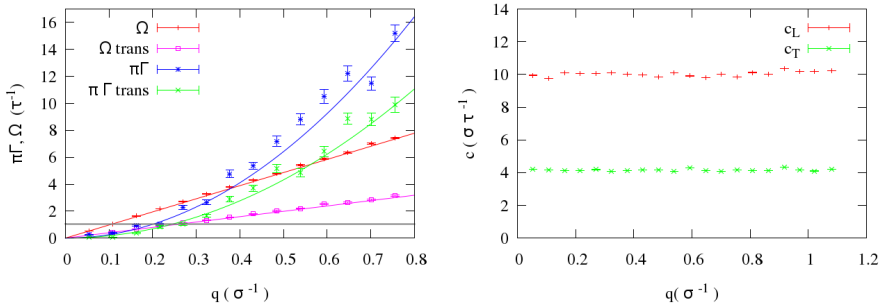

Figure A.28: Dispersion relation curve (left) and apparent phase velocity (right) of Lennar-Jones binary system of 2048000 atoms and quenching rate η_2.

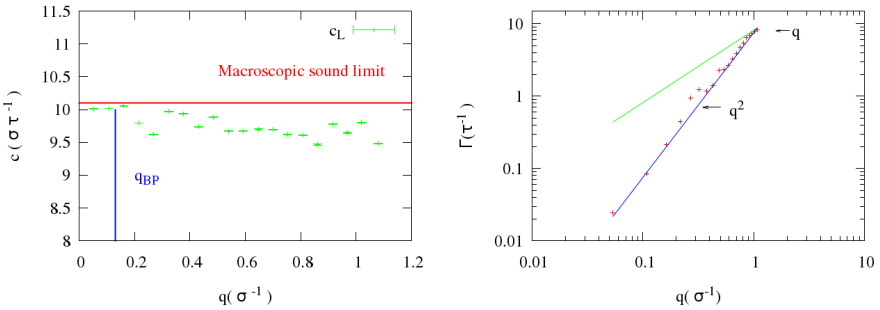

Figure A.29: Apparent longitudinal phase velocity as a function of wave vector q, q_{BP} and Macroscopic sound limit (left) and sound attenuation as a function of wave vector q (right) of Lennar-Jones binary system of 2048500 atoms and quenching rate η_1.

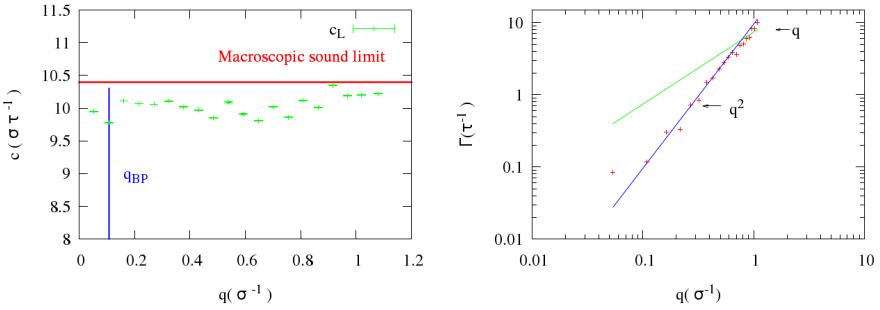

Figure A.30: Apparent longitudinal phase velocity as a function of wave vector q, q_{BP} and Macroscopic sound limit (left) and sound attenuation as a function of wave vector q (right) of Lennar-Jones binary system of 2048500 atoms and quenching rate η_2.

3764768 atoms

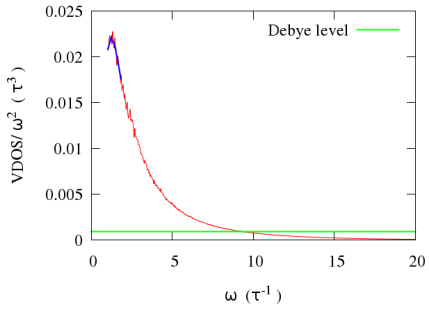

Figure A.31: Boson Peak observed in a Lennar-Jones binary system of 3764768 atoms and quenching rate η_1.

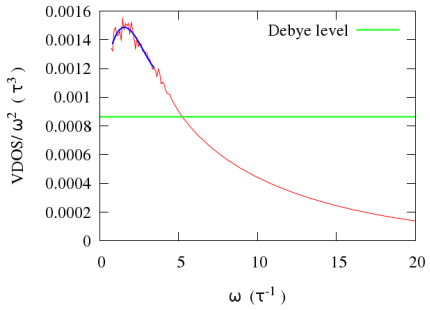

Figure A.32: Boson Peak observed in a Lennar-Jones binary system of 3764768 atoms and quenching rate η_2.

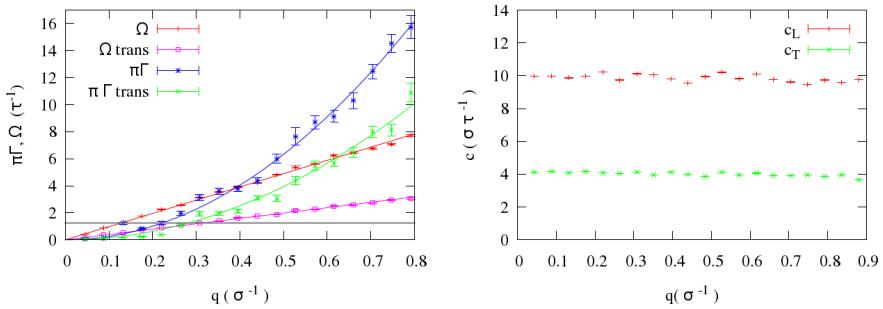

Figure A.33: Dispersion relation curve (left) and apparent phase velocity (right) of Lennar-Jones binary system of 3764768 atoms and quenching rate η_1.

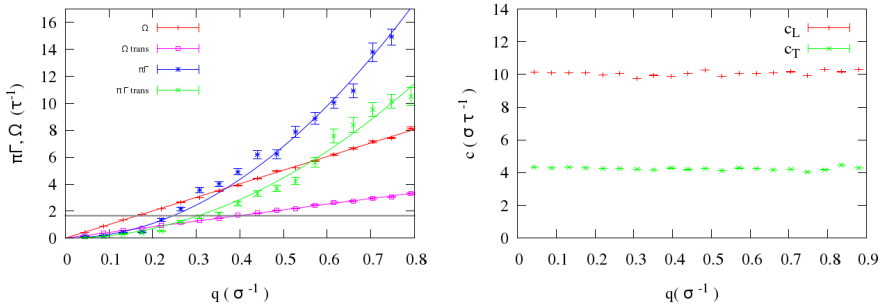

Figure A.34: Dispersion relation curve (left) and apparent phase velocity (right) of Lennar-Jones binary system of 3764768 atoms and quenching rate η_2.

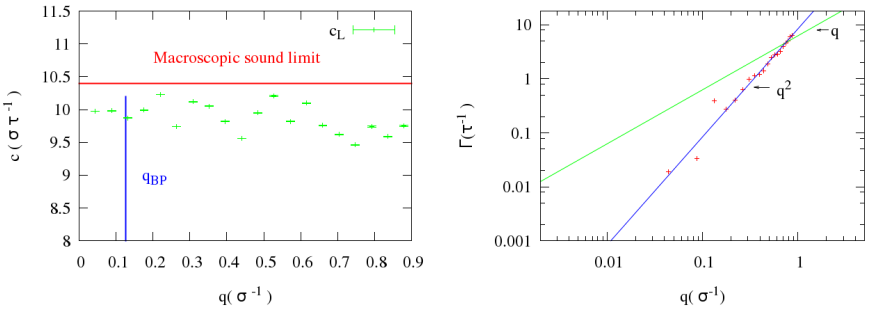

Figure A.35: Apparent longitudinal phase velocity as a function of wave vector q, q_{BP} and Macroscopic sound limit (left) and sound attenuation as a function of wave vector q (right) of Lennar-Jones binary system of 3764768 atoms and quenching rate η_1.

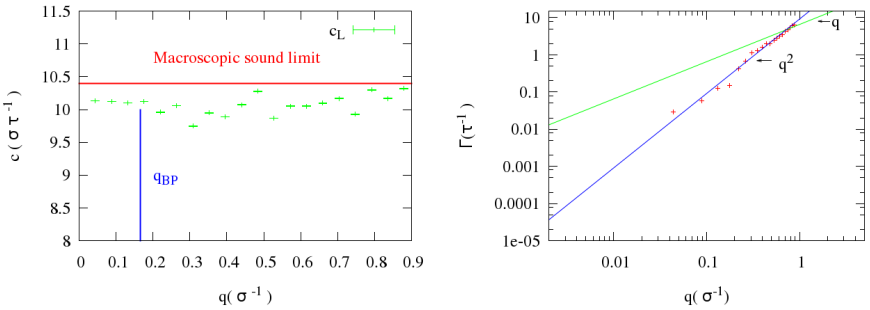

Figure A.36: Apparent longitudinal phase velocity as a function of wave vector q, q_{BP} and Macroscopic sound limit (left) and sound attenuation as a function of wave vector q (right) of Lennar-Jones binary system of 3764768 atoms and quenching rate η_2.

Embedded atom method potential

The EAM potential was tested on two different system concentrations, $Cu_{20}Pd_{80}$, and reducing the amount of Pd, $Cu_{50}Pd_{50}$. In both cases the metallic glasses were studied in two different system size (32000 and 4000000 atoms) in order to study different wave vectors frequency and applying two different quenching rates, $\eta_1 = 10^{13}K/s$ and $\eta_2 = 10^{12}K/s$. This part shows the graphics obtained by studying these metallic glasses.

Binary systems (80%-20%)

32000 atoms

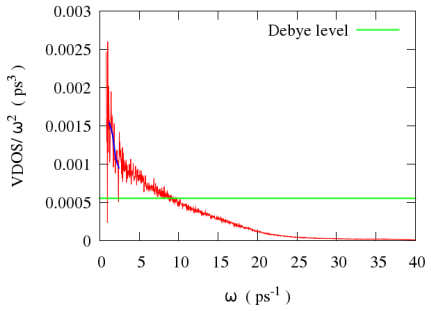

Figure A.37: Boson Peak observed in a EAM $Cu_{20}Pd_{80}$ binary system of 32000 atoms and quenching rate η_1.

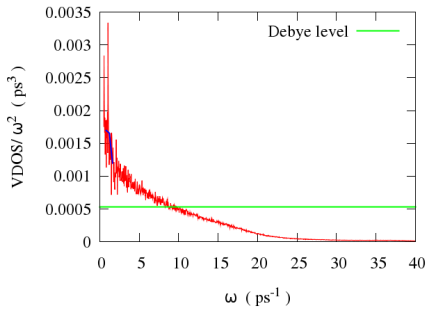

Figure A.38: Boson Peak observed in a EAM $Cu_{20}Pd_{80}$ binary system of 32000 atoms and quenching rate η_2.

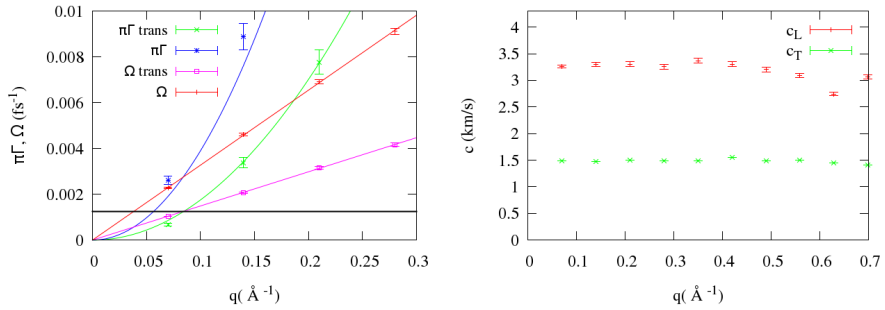

Figure A.39: Dispersion relation curve (left) and apparent phase velocity (right) in a EAM $Cu_{20}Pd_{80}$ binary system of 32000 atoms and quenching rate η_1.

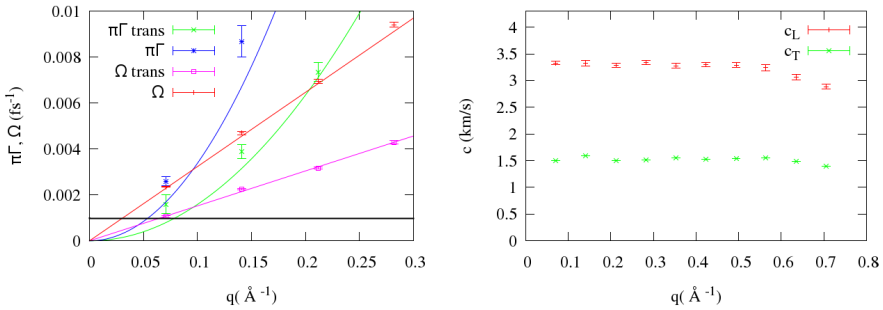

Figure A.40: Dispersion relation curve (left) and apparent phase velocity (right) in a EAM $Cu_{20}Pd_{80}$ binary system of 32000 atoms and quenching rate η_2.

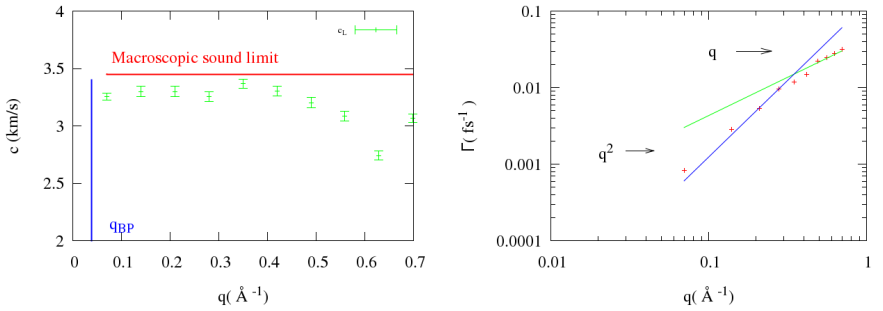

Figure A.41: Apparent longitudinal phase velocity as a function of wave vector q, q_{BP} and Macroscopic sound limit (left) and sound attenuation as a function of wave vector q (right) in a EAM $Cu_{20}Pd_{80}$ binary system of 32000 atoms and quenching rate η_1.

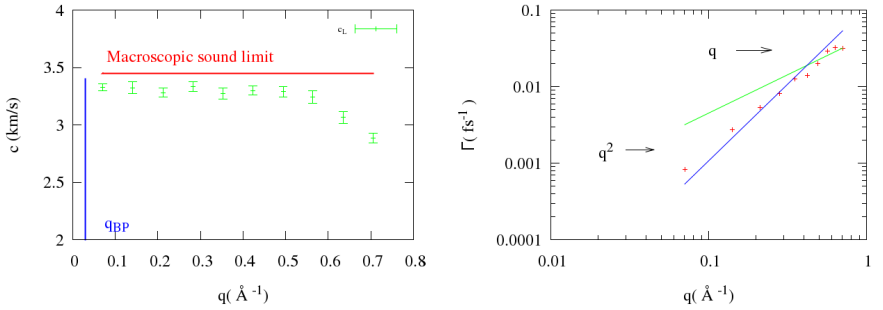

Figure A.42: Apparent longitudinal phase velocity as a function of wave vector q, q_{BP} and Macroscopic sound limit (left) and sound attenuation as a function of wave vector q (right) in a EAM $Cu_{20}Pd_{80}$ binary system of 32000 atoms and quenching rate η_2.

$4 \cdot 10^6$ atoms

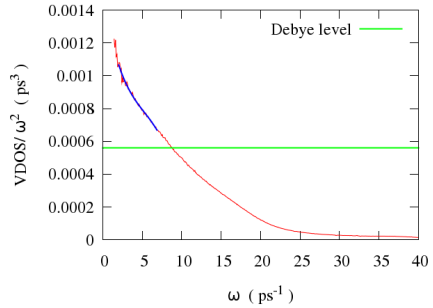

Figure A.43: Boson Peak observed in a EAM $Cu_{20}Pd_{80}$ binary system of $4 \cdot 10^6$ atoms and quenching rate η_1.

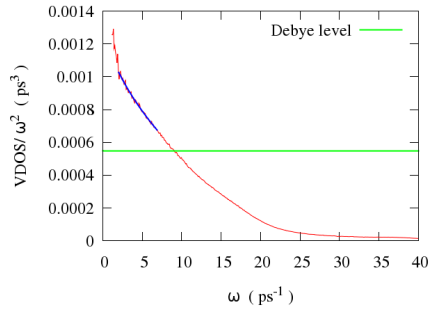

Figure A.44: Boson Peak observed in a EAM $Cu_{20}Pd_{80}$ binary system of $4 \cdot 10^6$ atoms and quenching rate η_2.

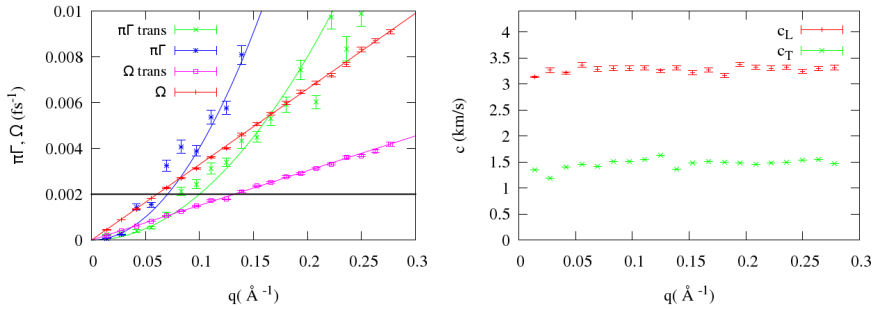

Figure A.45: Dispersion relation curve (left) and apparent phase velocity (right) in a EAM $Cu_{20}Pd_{80}$ binary system of $4 \cdot 10^6$ atoms and quenching rate η_1.

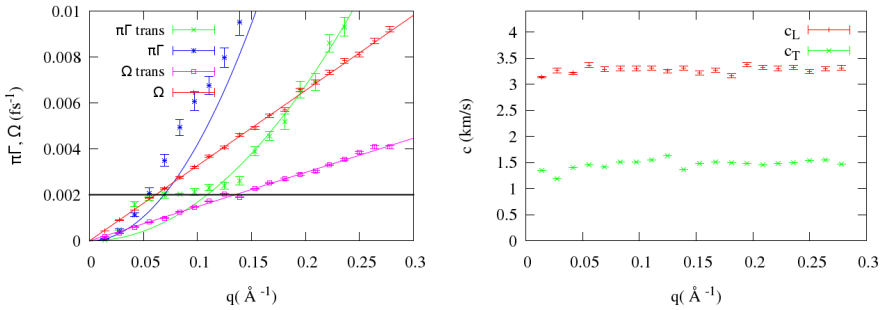

Figure A.46: Dispersion relation curve (left) and apparent phase velocity (right) in a EAM $Cu_{20}Pd_{80}$ binary system of $4 \cdot 10^6$ atoms and quenching rate η_2.

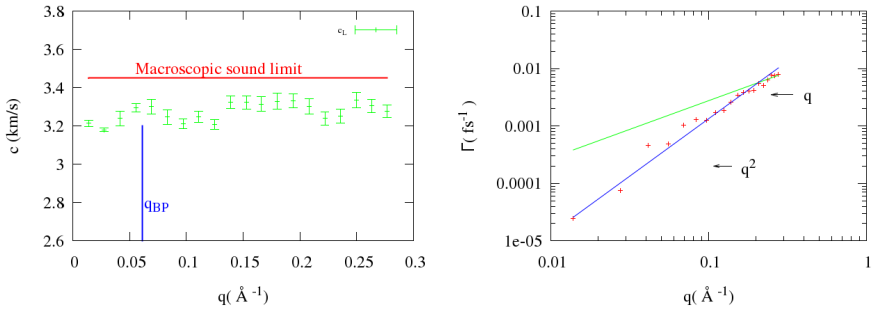

Figure A.47: Apparent longitudinal phase velocity as a function of wave vector q, q_{BP} and Macroscopic sound limit (left) and sound attenuation as a function of wave vector q (right) in a EAM $Cu_{20}Pd_{80}$ binary system of $4 \cdot 10^6$ atoms and quenching rate η_1.

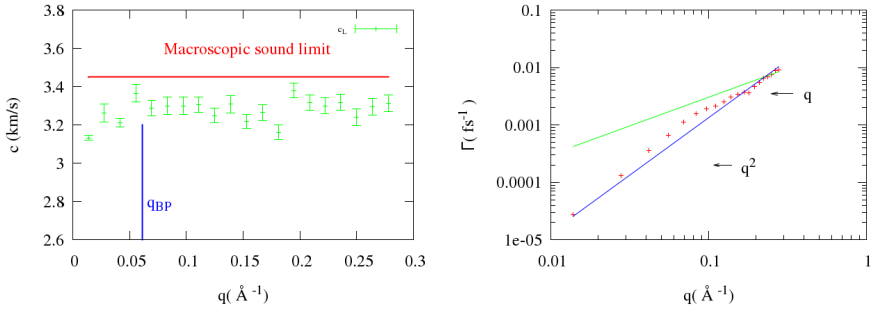

Figure A.48: Apparent longitudinal phase velocity as a function of wave vector q, q_{BP} and Macroscopic sound limit (left) and sound attenuation as a function of wave vector q (right) in a EAM $Cu_{20}Pd_{80}$ binary system of $4 \cdot 10^6$ atoms and quenching rate η_2.

Binary systems (50%-50%)

32000 atoms

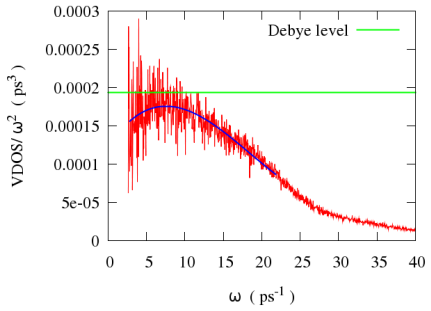

Figure A.49: Boson Peak observed in a EAM $Cu_{50}Pd_{50}$ binary system of 32000 atoms and quenching rate η_1.

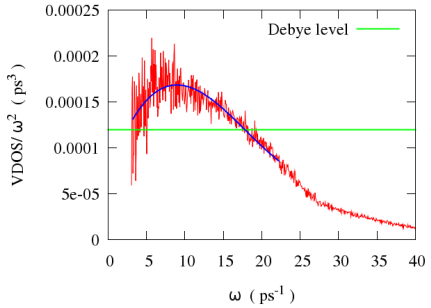

Figure A.50: Boson Peak observed in a EAM $Cu_{50}Pd_{50}$ binary system of 32000 atoms and quenching rate η_2.

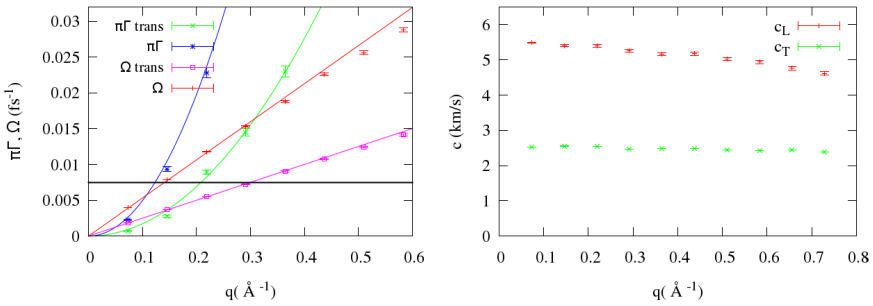

Figure A.51: Dispersion relation curve (left) and apparent phase velocity (right) in a EAM $Cu_{50}Pd_{50}$ binary system of 32000 atoms and quenching rate η_1.

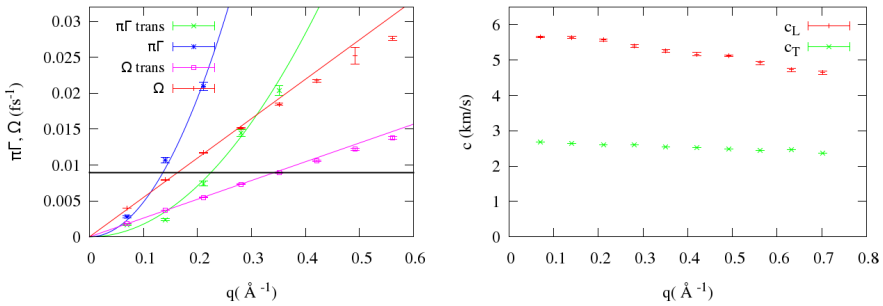

Figure A.52: Dispersion relation curve (left) and apparent phase velocity (right) in a EAM $Cu_{50}Pd_{50}$ binary system of 32000 atoms and quenching rate η_2.

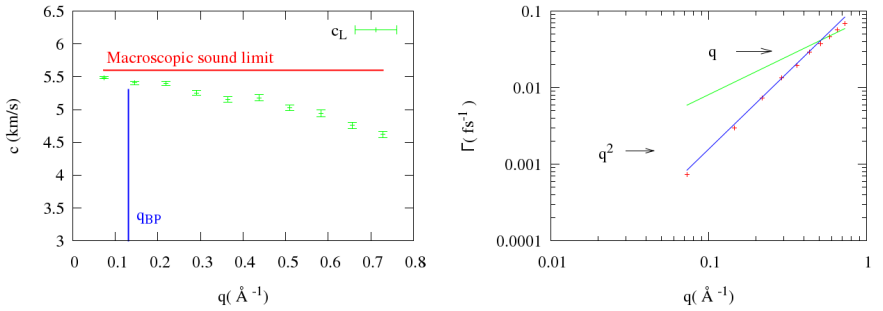

Figure A.53: Apparent longitudinalphase velocity as a function of wave vector q, q_{BP} and Macroscopic sound limit (left) and sound attenuation as a function of wave vector q (right) in a EAM $Cu_{50}Pd_{50}$ binary system of 32000 atoms and quenching rate η_1.

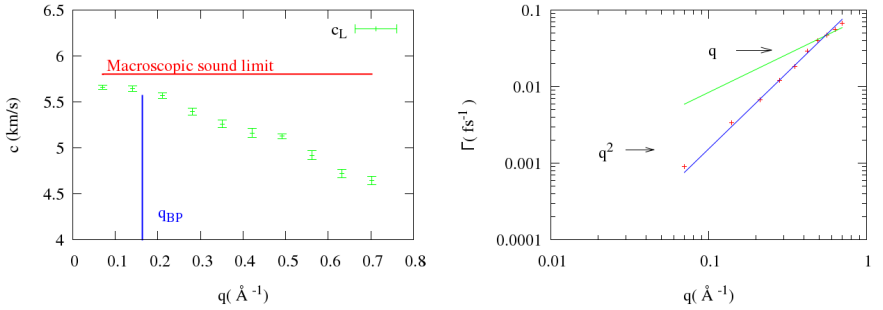

Figure A.54: Apparent longitudinal phase velocity as a function of wave vector q, q_{BP} and Macroscopic sound limit (left) and sound attenuation as a function of wave vector q (right) in a EAM $Cu_{50}Pd_{50}$ binary system of 32000 atoms and quenching rate η_2.

$4 \cdot 10^6$ atoms

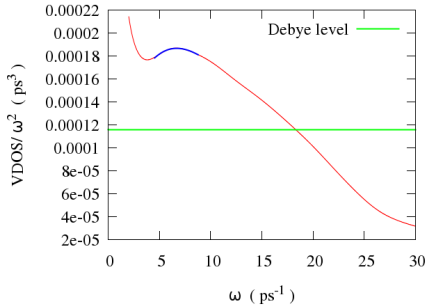

Figure A.55: Boson Peak observed in a EAM $Cu_{50}Pd_{50}$ binary system of $4 \cdot 10^6$ atoms and quenching rate η_1.

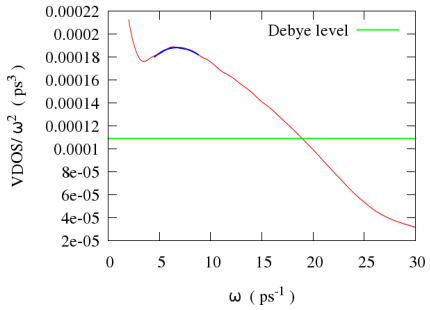

Figure A.56: Boson Peak observed in a EAM $Cu_{50}Pd_{50}$ binary system of $4 \cdot 10^6$ atoms and quenching rate η_2.

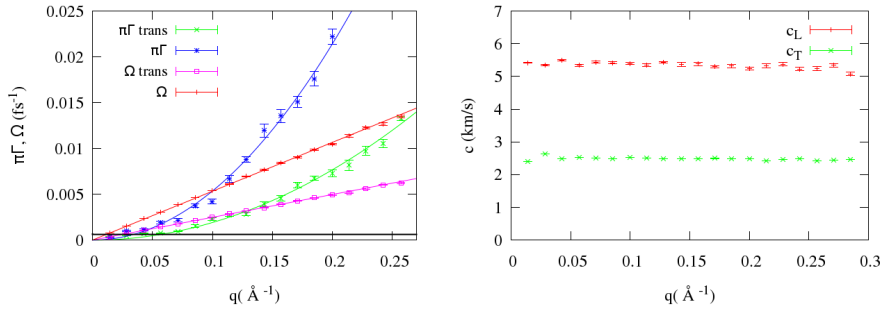

Figure A.57: Dispersion relation curve (left) and apparent phase velocity (right) in a EAM $Cu_{50}Pd_{50}$ binary system of $4 \cdot 10^6$ atoms and quenching rate η_1.

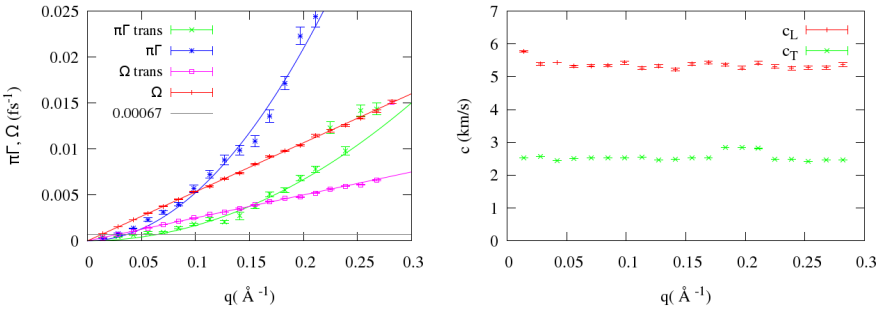

Figure A.58: Dispersion relation curve (left) and apparent phase velocity (right) in a EAM $Cu_{50}Pd_{50}$ binary system of $4 \cdot 10^6$ atoms and quenching rate η_2.

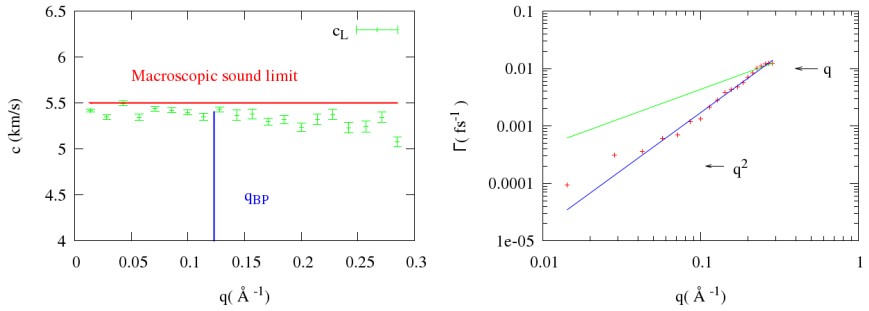

Figure A.59: Apparent longitudinal phase velocity as a function of wave vector q, q_{BP} and Macroscopic sound limit (left) and sound attenuation as a function of wave vector q (right) in a EAM $Cu_{50}Pd_{50}$ binary system of $4 \cdot 10^6$ atoms and quenching rate η_1.

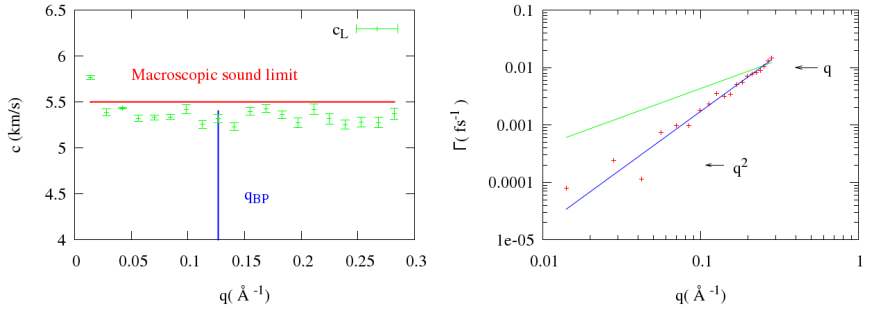

Figure A.60: Apparent longitudinal phase velocity as a function of wave vector q, q_{BP} and Macroscopic sound limit (left) and sound attenuation as a function of wave vector q (right) in a EAM $Cu_{50}Pd_{50}$ binary system of $4 \cdot 10^6$ atoms and quenching rate η_2.

Morse potential

Morse potential was studied in a more brief way and without focus on the effect of the size system and quenching rate. Just a single system was studied in this case and the results are the ones present in Morse results section. The studied system is a $Cu_{20}Pd_{80}$ of 32000 atoms obtained by applying a quenching rates $\eta_1 = 10^{13} K/s$.

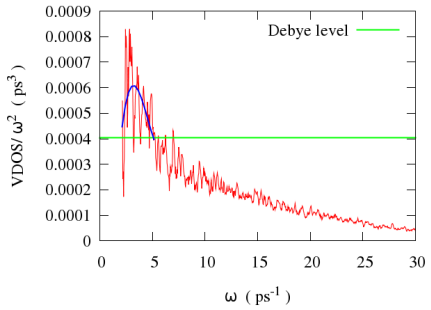

Figure A.61: Boson Peak observed in a Morse binary system of 32000 atoms and quenching rate η_1

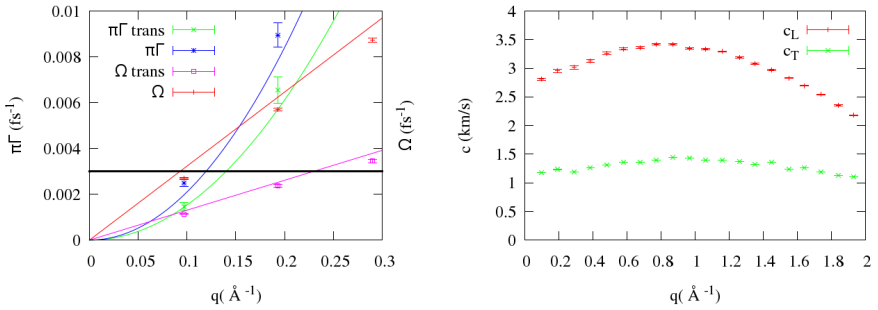

Figure A.62: Dispersion relation curve (left) and apparent phase velocity (right) in a Morse $Cu_{20}Pd_{80}$ binary system of 32000 atoms and quenching rate η_1.

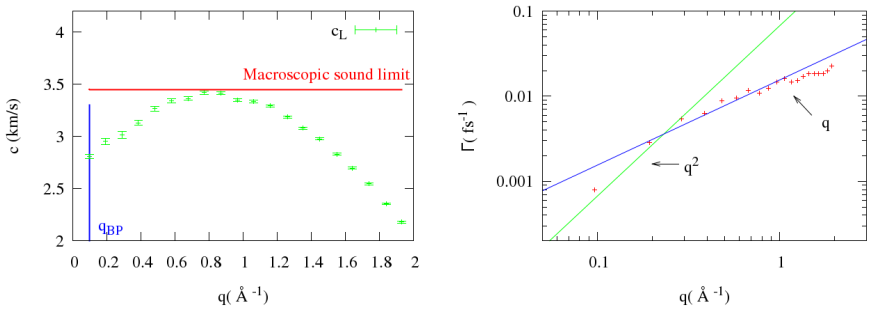

Figure A.63: Apparent longitudinal phase velocity as a function of wave vector q, q_{BP} and Macroscopic sound limit (left) and sound attenuation as a function of wave vector q (right) in a Morse $Cu_{20}Pd_{80}$ binary system of 32000 atoms and quenching rate η_1.

Bibliography

[1] W. Klement, R. H. Willens, and P. Duwez. Non-crystalline structure in solidified gold-silicon alloys. *Nature*, 187:869–870, 1960.

[2] A Inoue and A Takeuchi. Recent progress in bulk glassy alloys. *Materials Transactions*, 43:1892–1906, 2002.

[3] W. L. Johnson. Bulk glass-forming metallic alloys: Science and technology. *Mat. Res. Bull.*, 24:42–56, 1999.

[4] V. Ponnambalam, S. J. Poon, and G. J. Shiflet. Fe-based bulk metallic glasses with diameter thickness larger than one centimeter. *J Mater Res.*, 19:1320–1323, 2004.

[5] Z. P. Lu, C. T. Liu, C. A. Carmichael, W. D. Porter, and S. C. Deevi. Bulk glass formation in an fe-based fe-y-zr-m (m = cr, co, al)-mo-b system. *J Mater Res.*, 19:921–929, 2004.

[6] A. Ashby, M. & Greer. Metallic glasses as structural materials. *Scripta Materialia*, 54:321–326, 2006.

[7] G. Monaco and V. M. Giordano. Breakdown of the debye approximation for the acoustic modes with nanometric wavelengths in glasses. *Proceeding of the National Academy of Science of the United States of America*, 106:3659, 2009.

[8] F. Leonforte, R. Boissière, A. Tanguy, J. Wittmer, and J. L. Barrat. Continuum limit of amorphous elastic bodies. iii. three-dimensional systems. *Phys Rev B*, 72:224206, 2005.

[9] G. Baldi, M. Zanatta, E. Gilioli, V. Milman, K. Refson, B. Wehinger, B. Winkler, A. Fontana, and G. Monaco. Emergence of crystal-like atomic dynamics in glasses at the nanometer scale. *Physical Review Letters*, 110:185503, 2013.

[10] J. F. Loffler. Bulf metallic glasses. *Intermetallics*, 11:529, 2003.

[11] T. C. Hufnagel. Preface to the viewpoint set on mechanical behavior of metallic glasses. *Scripta Materialia*, 54:317, 2006.

[12] C. A. Schuh, T. C. Hufnagel, and U. Ramamurty. Mechanical behavior of amorphous alloys. *Acta Mater.*, 55:4067–4109, 2007.

[13] M. W. Chen. Mechanical behavior of metallic glasses: Microscopic understanding of strength and ductility. *Annual Review of Materials Research*, 38:445–469, 2008.

[14] A. Drehman, A. Greer, and D. Turnbull. Bulk formation of a metallic-glass - pd-40 ni-40-p-20. *Applied Physics Letters*, 41:716–717, 1982.

[15] A. L. Greer. Metallic glasses. *Science*, 267:1947–1995, 1995.

[16] M. Telford. The case for bulk metallic glass. *Materials today*, 7:36–43, 2004.

[17] R. D. Conner, W. L. Johnson, N. E. Paton, and W. D. Nix. Shear bands and cracking of metallic glass plates in bending. *J. Appl. Phys.*, 94:904, 2003.

[18] A. Shamimi Nouri and et al. Chemistry (intrinsic) and inclusion (extrinsic) effects on the toughness and weibull modulus of fe-based bulk metallic glasses. *Philos. Mag. Lett.*, 88:853, 2008.

[19] D. C. Hofmann, J.-Y. Suh, A. Wiest, G. Duan, M.-L. Lind, and W. L. Demetriou, M. D. & Johnson. Designing metallic glass matrix composites with high toughness and tensile ductility. *Nature*, 451:1085–9, 2008.

[20] M. E. McHenry, M. A. Willard, and D. E. Laughlin. Amorphous and nanocrystalline materials for applications as soft magnets. *Progress in Materials Science*, 44:291–433, 1999.

[21] K. Hashimoto. What we have learned from studies on chemical properties of amorphous alloys? *Applied Surface Science*, 257:8141–8150, 2011.

[22] A. Inoue. Stabilization of metallic supercooled liquid and bulk amorphous alloys. *Acta Mater.*, 48:276–306, 2000.

[23] M. H. Cohen and D. Turnbull. Molecular transport in liquids and glasses. *J.Chem. Phys.*, 31:1164, 1959.

[24] M. H. Cohen and G. S Grest. Liquid-glass transition, a free volume approach. *Phys. Rev. B*, 20:1077, 1979.

[25] D. Turnbull and M. H. Cohen. Free-volume model of amorphous phase -glass transition. *J. Chem. Phys*, 34:120, 1961.

[26] D. Turnbull and M. H. Cohen. On free-volume model of liquid-glass transition. *J. Chem. Phys*, 52:3038, 1970.

[27] D. B. Miracle. A structural model for metallic glasses. *Nat. Mater.*, 3:697, 2004.

[28] H. W. Cheng, W. K. Luo, F. M. Alamgir, J. M. Bai, and E. Ma. Atomic packing and short-to-medium-range order in metallic glasses. *Nature*, 439:419, 2006.

[29] D. B. Miracle, A. L. Greer, and K. F. Kelton. Icosahedral and dense random cluster packing in metallic glass structures. *J. Non-Cryst. Solids*, 354:4049, 2008.

[30] M. Li, C. Z. Wang, S. G. Hao, M. J. Kramer, and K. M. Ho. Structural heterogeneity and medium-range order in zr_xcu_{100-x} metallic glasses. *Phys. Rev. B*, 80:184201, 2009.

[31] J. D. Bernal. Geometrical approach to the structure of liquids. *Nature*, 183:141, 1959.

[32] J. D. Bakerian. Lecture 1962 - structure of liquids. *Proc. R. Soc. London, Ser. A*, 280:299, 1964.

[33] J. L. Finney. Random packings and structure of simple liquids .1. geometry of random close packing. *Proc. R. Soc. London, Ser. A*, 319:479, 1970.

[34] G. Z Voronoi. Nouvelles applications des parametres continus a la theorie des formes quadratiques. *J. Reine u. Angew. Math.*, 134:199, 1908.

[35] J. A. Prins and H. Petersen. Theoretical diffraction patterns corresponding to some simple types of molecular arrangement in liquids. *Physica*, 3:147, 1936.

[36] P. H. Gaskell. Structure of simple inorganic amorphous solids. *J. Phys. C: Solid State Phys.*, 12:4337, 1979.

[37] P. H. Gaskell. Models for the structure of amorphous metals. *Top. Appl. Phys.*, 53:5–49, 1983.

[38] D. Ma, A. D. Stoica, and X. L. Wang. Power-law scaling and fractal nature of medium-range order in metallic glasses. *Nat. Mater.*, 8:30, 2009.

[39] M.T. Dove. *Structure and dynamics*. Oxford University Press, 2003.

[40] A. Einstein. Die plancksche theorie der strahlung und die theorie der spezifischen wärme. *Annalen der Physik*, 327:180, 1906.

[41] Peter Debye. Zur theorie der spezifischen wÃ€rme. *Annalen der Physik*, 39:789–839, 1912.

[42] N. Jakse, A. Nassour, and A. Pasturel. Structural and dynamics origin of the boson peak in cu-zr metallic glass. *Phys Rev B*, 85:174201, 2012.

[43] B. Rufflé, G. Guimbretière, E. Courtens, R. Vacher, and G. Monaco. Glass-specific behavior in the damping of acousticlike vibrations. *Phys Rev Lett*, 96:045502, 2006.

[44] H. Shintani and H. Tanaka. Universal link between the boson peak and transverse phonons in glass. *Nature Materials*, 7:870–877, 2008.

[45] G. Ruocco, A. Matic amd T. Scopigno, and S. Yannopoulos. Comment on "glass-specific behavior in the damping of acousticlike vibrations" by b. ruffle' et al. *Phys Rev Lett*, 98:011901, 2007.

[46] T. Scopigno, J. B. Suck, R. Angelini, F. Albergamo, and G. Ruocco. High-frequency dynamics in metallic glasses. *Phys Rev Lett.*, 96:135501, 2006.

[47] T. Ichitsubo, S. Hosokawa, K. K. Matsuda, E Matsubara, N Nishiyama, S Tsutsui, and A. Q. R. Baron. Nanoscale elastic inhomogeneity of a pd-based metallic glass: Sound velocity from ultrasonic and inelastic x-ray scattering experiments. *Phys Rev B*, 76:140201, 2007.

[48] B. Ruta, G. Baldi, M. Giordano, L. Orsingher, S. Rols, F. Scarponi, and G. Monaco. Communication: High-frequency acoustic excitations and boson peak in glasses: A study of their temperature dependence. *J. Chem Phys*, 133:041101, 2010.

[49] G. Baldi, M. Giordano, G. Monaco, and B. Ruta. Sound attenuation at terahertz frequencies and the boson peak of vitreous silica. *Phys Rev. Lett*, 104:195501, 2010.

[50] P. Bruna, G. Baldi, E. Pineda, J. Serrano, J. B. Suck, D. Crespo, and G. Monaco. Communication: Are metallic glasses different from other glasses? a closer look at their high frequency dynamics. *J. Chem Phys*, 135:101101, 2011.

[51] G. SS. Grest, S. R. Nagel, and A. Rahman. Longitudinal and transverse excitations in a glass. *Phys Rev Lett.*, 49:1271–1274, 1982.

[52] J. Hafner. Structure and vibrational dynamics of the metallic-glass ca70mg30. *Physical Review B*, 27:678–695, 1983.

[53] R . N. Barnett, C. L. Cleveland, and U. Landman. Structure and dynamics of a metallic-glass-molecular-dynamics simulations. *Phys Rev Lett.*, 55:2035–2038, 1985.

[54] W. Jin, P. Vashishta, R. K. Kalia, and J.P. Rino. Dynamic structure factor and vibrational properties of sio2 glass. *Physical Review B.*, 48:9359–9368, 1993.

[55] M. Sampoli, P. Benassi, R. Dell'Anna, V. Mazzacurati, and G. Ruocco. Numerical study of the low-frequency atomic dynamics in a lennard-jones glass. *Philosophical Magazine B-Physics of Condensed Matter Statistical Mechanics Electronic Optical and Magnetic Properties.*, 77:473–484, 1998.

[56] P. M. Derlet, R. Maaß, and J. F. Löffler. The boson peak of model glass systems and its relation to atomic structure. *Eur. J. Phys. B*, 85:148, 2012.

[57] M. Bauchy. Structural, vibrational, and thermal properties of densified silsilica: Insights from molecular dynamics. *Journal Chem Phys*, 137:044510, 2012.

[58] M. Zanatta, G. Baldi, S. Caponi, A Fontana, E. Gilioli, M. Krish, C Masciovecchio, G. Monaco, L. Orsingher, F Rossi, G. Ruocco, and R. Verbeni. Elastic properties of permanently densified silica: A raman, brillouin light, and x-ray scattering study. *Phys Rev B*, 81:212201, 2010.

[59] N. Kitamura, K. Fukumi, H. Mizoguchi, M. Makihara, a. Higuchi, N. Ohno, and T. Fukunaga. High pressure densification of lithium silicate glasses. *J Non Cryst Solids*, 274:244–248, 2000.

[60] A. Monaco, A.I. Chumakov, G. Monaco, W. A. Crichton, A. Meyer, L. Comez, D. Fioretto, and R. Korecki, J.and Rüffer. Effect of densification on the density of vibrational states of glasses. *Phys Rev Lett*, 97:135501, 2006.

[61] L. Hong, B. Begen, A. Kisliuk, C. Alba-Simionesco, V. N. Novikov, and A. P. Sokolov. Pressure and density dependence of the boson peak in polymers. *Phys Rev B*, 78:134201, 2008.

[62] M.P. Allen and D.J. Tildesley. *Computer simulation of liquids.* Oxford University Press, 1989.

[63] H. Gould and J. Tobechnik. *Introduction to computation simulation methods. applications to physical systems.* Addison Wesley ed., 1996.

[64] B.S. Frenkel. *Understanding molecular simulations.* Academic Press, 1996.

[65] J. E. Lennard-Jones. On the determination of molecular fields. *Proc. R. Soc. London, Ser. A*, 106:738, 1924.

[66] P. M. Morse. Diatomic molecules according to the wave mechanics. ii. vibrational levels. *Phys Rev*, 34:57, 1929.

[67] M. S. Daw and M. I. Baskes. Embedded-atom method: Derivation and application to impurities, surfaces and other defects in metals. *Phys Rev B*, 29:6443, 1984.

[68] S. M. Foiles, M. I.I. Baskes, and M. S. Daw. Embedded-atom-method functions for the fcc metals cu, ag, au, ni, pd, pt, and their alloys. *Phys Rev B*, 33:7983, 1986.

[69] D. D. Abajingin. Solution of morse potential for face center cube using embedded atom method. *Advanced in Physics Theories and Applications*, 8:36, 2012.

[70] Chang Lyoul Kong. Combining rules for intermolecular potential parameters. ii. rules for the lennard-jones (12-6) potential and the morse potential. *Journal of Chemical Physics*, 59:2464, 1973.

[71] L. A. Girifalco and V. G. Weizer. Application of the morse potential function to cubic metals. *Phys Rev*, 114:687–690, 1959.

[72] Central Michigan University. Interactive Structrue Analysis of Amorphous and Crystalline Systems project. http://isaacs.sourceforge.net/phys/pbc.html.

[73] F. Ercolessi. *A molecular dynamics primer.* Spring College in COmputational Physics, 1997.

[74] L. Verlet. Computer 'experiments' on classical fluids. i. thermodynamical properties of lennard-jones molecules. *Phys Rev*, 159:98–103, 1967.

[75] L. Verlet. Computer 'experiments' on classical fluids. ii. equilibrium correlation functions. *Phys Rev*, 165:201–214, 1968.

[76] D. J. Evans and B. L. Holian. The nose-hoover thermostat. *J Chem Phys*, 83:4069–4074, 1985.

[77] H. Nosé. A molecular dynamics method for simulations in the canonical ensemble. *Molec Phys*, 52:255–268, 1984.

[78] M. Parrinello and A. Rahman. Polymorphic transitions in single-crystals - a new molecular-dynamics method. *J Appl Phys*, 52:7182–7190, 1981.

[79] M. Parrinello and A. Rahman. Crystal structure and pair potentials: A molecular-dynamics study. *Phys Rev Lett*, 45:1196–1199, 1980.

[80] J. Andersen. Molecular dynamics simulations at constant pressure and/or temperature. *Journal of Chemical Physics*, 72:2384, 1980.

[81] Peter Derlet. http://www.psi.ch/cmt/peter-derlet.

[82] Paul Scherrer Institute. http://www.psi.ch/.

[83] MOLDY MDCASK. https://asc.llnl.gov/computing_resources/purple/archive/benchmarks/mdcask/mdcask.readme.bm.html.

[84] Barcelona Supercomputing Center (BSC). http://www.bsc.es.

[85] J. A. Barker and D. Henderson. What is 'liquid'? understanding the states of matter. *Rev Mod Phys*, 48:587–671, 1976.

[86] Department of Crystallography & Structural Biology CSIC, Spain. Crystallography. http://www.xtal.iqfr.csic.es/cristalografia/index-en.html.

[87] J. P. Hansen and I. R. McDonald. *Theory of simple liquids*. Academic Press, 2005.

[88] G. Monaco and S. Mossa. Anomalous properties of the acoustic excitations of glasses on the mesoscopic length scale. *Proc. Natl. Acad. Sci. USA*, 106:16907–16912, 2009.

[89] J. M. Dickey and A. Paskin. Computer simulation of the lattice dynamics of solids. *Phys Rev*, 188:1407, 1969.

[90] N. P. Lazarev, A. S. Bakai, and C. Abromeit. Molecular dynamics simulation of viscosity in supercooled liquid and glassy agcu alloy. *Journal of Non-Crystalline Solids*, 353:332–337, 2007.

[91] B. Hess. Determining the shear viscosity of model liquid from molecular dynamics simulation. *Journal of Chemical Physics*, 116:209, 2002.

[92] A. Takeuchi, H. Kato, and A. Inoue. Vogel-fulcher-tammann plot for viscosity scaled with temperature interval between actual and ideal glass transitions for metallic glasses in liquid and supercooled liquid states. *Intermetallics*, 18:406–411, 2010.

[93] C. A. Angell. Relaxation in liquids, polymers and plastic crystals - strong/fragile patterns and problems. *J. Non-Cryst. Solids*, 131-133:13–31, 1991.

[94] European Synchrotron Radiation Facility. http://www.esrf.eu/.

[95] G. Wahnström. Molecular-dynamics study of a supercooled 2-component lennard-jones system. *Physical Review A*, 44:3752–3764, 1991.

[96] W. G. Hoover. Canonical dynamics: Equilibrium phase-space distributions. *Phys Rev A*, 31:1695–1697, 1985.

[97] Y Waseda, H Okazaki, and T Masumoto. Current views on structure and crystallization of metallic glasses. *Joural of Materials Science*, 12:1927–1949, 1977.

[98] xmakemol, http://www.nongnu.org/xmakemol/.

[99] A. Vasiliev, T. Voloshok, A. Granato, D. Joncich, Yu. Mitrofanov, and V. Khonik. Relationship between low-temperature boson heat capacity peak and high-temperature shear modulus relaxation in a metallic glass. *Physical Review B*, 80:172102, 2009.

[100] Tullio Scopigno, Giancarlo Ruocco, and Francesco Sette. Microscopic dynamics in liquid metals: The experimental point of view. *Reviews of Modern Physics*, 77:881–933, 2005.

[101] H.R. Schober. Quasi-localized vibrations and phonon damping in glasses. *Journal of Non-Crystalline Solids*, 357:501–505, 2011.

[102] W Schirmacher. Thermal conductivity of glassy materials and the boson peak. *Europhysics Letters (EPL)*, 73:892–898, 2006.

[103] M.D. Ediger. Can density or entropy fluctuations explain enhanced translational diffusion in glass-forming liquids? *Journal of Non-Crystalline Solids*, 235-237:10–18, 1998.

[104] Majid Mosayebi, Emanuela Del Gado, Patrick Ilg, and Hans Christian Öttinger. Probing a critical length scale at the glass transition. *Physical Review Letters*, 104:205704, 2010.

[105] L. Orsingher, G. Baldi, A. Fontana, L. E. Bove, Unruh T., A. Orecchini, C. Petrillo, N. Violini, and F. Sacchetti. High-frequency dynamics of vitreous gese2. *Phys Rev B*, 82:115201, 2010.

[106] G. Ruocco, F. Sciortino, F. Zamponi, C. De Michele, and T. Scopigno. Landscape and fragilities. *J.Chem.Phys.*, 120:10666, 2004.

[107] S. Sastry. The relationship between fragility configurational entropy and the potential energy landscape of glass-forming liquids. *Nature*, 409:164, 2001.

[108] T. Scopigno, D. Cangialosi, and Ruocco G. Universal relation between viscous flow and fast dynamics in glass-forming materials. *Phys Rev B*, 81:100202, 2010.

[109] C. A. Angell, K. L. Ngai, G. B. McKenna, P. F. McMillan, and S. W. Martin. Relaxation in glassforming liquids and amorphous solids. *Journal of Applied Physics*, 88, 2000.

[110] D. Coslovich and G. Pastore. Understanding fragility in supercooled lennard-jones mixtures. ii. potential energy surface. *Journal of Chemical Physics*, 127:124505, 2007.

[111] R. Raghavan, P. Murali, and U. Ramamurty. Influence of cooling rate on the enthalpy relaxation and fragility of a metallic glass. *Metallurgical and Materials Transactions A*, 39A:1573, 2008.

[112] Byeong-Joo Lee, Jae-Hyeok Shim, and M. I. Baskes. Semiempirical atomic potentials for the fcc metals cu, ag, au, ni, pd, pt, al, and pb based on first and second nearest-neighbor modified embedded atom method. *Phys. Rev. B*, 68:144112, 2003.

[113] S Hosokawa, J-F Bérar, N Boudet, T Ichitsubo, E Matsubara, W-C Pilgrim, and N Nishiyama. Partial structure of pd 42.5 ni 7.5 cu 30 p 20 bulk metallic glass: Comparison to the reference pd 40 ni 40 p 20 glass. *Journal of Physics: Conference Series*, 98:012013, 2008.

[114] A. Marruzzo, W. Schirmacher, A. Fratalocchi, and G. Ruocco. Heterogeneus shear elasticity of glasses: the origin of the boson peak. *Sci. Rep*, 3, 2013.